University of Stavanger

Faculty of Science and Technology

MASTER'S THESIS

Study program/Specialization: **Petroleum Engineering/Well & Drilling Technology**	Spring semester, 2016 Open access
Writer: **Olaleke Anthony Akisanmi**	…… (Writer's signature)
Faculty supervisor: **Mesfin Belayneh** External supervisor(s): **Eric Cayeux, IRIS, Stavanger**	
Thesis title: Automatic Management of Rate of Penetration in Heterogeneous Formation Rocks	
Credits (ECTS): 30	
Key words: Drillbotics Rate of Penetration PDC Bits ROP Models Mechanical Specific Energy Weight on Bit Revolutions per minute ROP Modeling	Pages: …….117…… + enclosure: ….24…… Stavanger, ...15th June, 2016… Date/year

ABSTRACT

Rate of penetration (ROP) is dependent on several factors and it is essential to properly manage and control this in order to save cost of drilling operations.

Drillbotics test skid is an automated machine that is expected to drill as vertically as possible into a rock formation of varying compositions. This thesis demonstrates the design approach to controlling ROP by managing the effects of circulation system, WOB, RPM, bit torque and the reaction time of the controller in order to achieve an optimal drilling operation. Also covered are the detailed steps based on the design guidelines for the drillbotics 2016 competition. The results obtained during testing indicated high potential of controlling ROP automatically during drilling operations.

The second part of the thesis focused on multiple regression techniques which were used in predicting the ROP of a well by using the coefficients obtained from a near-by well on the same block. The analysis was based on four wells, a pair on two blocks respectively. The technique considered the combined effects of drilling parameters, MSE and D-exponent independently in order to predict the ROP of the nearby well. The results displayed both, the actual ROP and the modelled ROP plots for comparison.

ACKNOWLEDGEMENT

I would like to thank God for being my strength and guide throughout my study programme.

My sincere gratitude for the supervision and guidance of Mesfin Belayneh for his motivation and immense knowledge; so also the support and contributions of Eric Cayeaux, towards the success of this research & write up.

I would also like to thank my parents for supporting me spiritually throughout the study programme.

Special thanks to my darling wife, Olapeju, for her constant love, support, understanding and encouragement throughout the entire programme. Thanks to my beautiful daughter, Anjolaoluwa, for being understanding why I could not witness her development and growing up in the last two years.

Finally I express my gratitude to a wonderful friend and family of Gunhild for showing me so much care and support since I got to this country.

Stavanger, 15th June, 2016.

Olaleke Anthony Akisanmi

TABLE OF CONTENT

LIST OF TABLES

LIST OF FIGURES

NOMENCLATURE

t – Travel time of p-wave

Δt – Sonic travel time

$\emptyset$ - Porosity

l_p - Cutter penetration per revolution

τ - Shear stress

c - Cohesive resistance of the rock

$\propto$ - Bottom hole cutting angle or helix angle

$\dot{\gamma}$ - Shear rate

σ_n - Normal stress

θ - Angle of internal friction

h - Fractional tooth height worn away

d_b – Bit diameter

μ - Bit specific coefficient of sliding friction / apparent viscosity / plastic viscosity

f_1 to f_8 - normalized effects of factors of ROP

g_p – Pore pressure gradient

ρ_c, ρ_m, ρ_f - mud weight

F_j - Hydraulic impact force beneath the bit

d_n - Bit nozzle diameter

ρ – Density

ρ_s – Density of cuttings

Re – Reynolds number

d – d-exponent

d_{corr} – Corrected d-exponent

f – Fanning friction factor

f_D - Darcy-Weisbach friction factor

D – Internal diameter of a conduit

D_e- Equivalent circular diameter

L – Length of pipe

ΔP – Pressure drop

Q – Flow rate

A – Cross-sectional area

C_v - Flow coefficient

Po – Constant weight on bit

F_o – Bit side force

A_n, B_n – Rayleigh Ritz constants

δ - Deflection at the top of the BHA

r – Radius from center of hole; radius of pipe

F_g- Apparent weight acting due to gravity

F_D - Drag force

LIST OF ABBREVIATIONS

DSATS - Drilling System Automation Technical Section

ROP – Rate of penetration

HSE – Health, Safety and Environment

PDC – Polycrystalline diamond compact

UCS - Uniaxial Compressive Strength

CCS - Confined compressive strength

WOB – Weight on bit

RPM – Revolutions per minute

N – Rotary speed

T, T_{bit} – Bit torque

T_{yield} – Yield torque

MSE – Mechanical specific energy

MSE_{adj} - Mechanical specific energy adjusted

EFF_M - Mechanical efficiency factor

BHA – Bottom hole assembly

MWD – Measurement while drilling

DOC – Depth of cut

JSA – Junk slot area

HSI – Horse power per square inch

D-Exp – D-exponent

DG – Dull grade

NPP - Normal Pore Pressure gradient

ECD – Equivalent circulating density

MSL – Mean sea level MSE

D-exp – D- exponent

P – Axial load

SF – side force

PE – Potential energy

E - Young's modulus of elasticity

I – Area Moment of inertia

J – Polar moment of inertia

IADC – International Association of Drilling Contractors

TYS - Tensile yield strength

STS - Shear yield strength

CC – Cuttings Concentration

FFT – Fast Fourier Transform

wrt – with respect to

1 INTRODUCTION

This thesis consists of two parts. The first part deals with Drillbotics design, constructing and system testing. The second part deals with North Sea drilling well data ROP modelling and application of the model to predict the ROP of a nearby well.

1.1 Background and motivation

Drillbotics is a competition organized by SPE Drilling System Automation Technical Section (DSATS) to steer students in the petroleum mechanical and computer engineering towards constructing a rig that could drill into a formation autonomously without causing any damage to the drill string or other components.[1] In 2015, the objective was to manage any sharp transition in rock strength (horizontal layers); while in 2016, the objective is to dill as vertically as possible when the formations have a large dip and strong strength contrast.

In 2015, four (4) universities participated in the competition, three from the United States and one from Norway, Europe. The universities are: University of Oklahoma, Texas A&M University, University of Texas and University of Agder.

None of the universities managed to drill through the rock. While the University of Agder did not manage to construct the rig, others primarily had either pipe failure or bit failure (see *Figure 1.1 and Figure 1.2*).

Figure 1.1: Pipe failure from A&M

Figure1.2: bit failure from Houston

University of Stavanger decided to take part in this year's competition, however, no European university was selected among the five finalists. Despite this, the university decided to go ahead with the project (with the support of IRIS) to demonstrate our understanding of what we had learned in the course of our master's programme. This thesis has considered automatic management of rate of penetration in the drilling operation.

The application of automation is proven in many industries and found out to be efficient and reliable in terms of operations and reducing HSE problems. The oil industry is now working on how to partly or fully automate drilling operations. As a petroleum engineer, I was motivated to challenge myself for Drillbotics competition.

1.2 Objective

This research work is being divided into two (2) parts. It is primarily based on the drillbotics design, considering the management of rate of penetration in the drilling operations. The second part is to show how we can model rate of penetration of a well from the field data of a nearby well.

The design and construction of the robot have been based on the guidelines stipulated by SPE Drilling System Automation Technical Section (DSATS) for 2016 competition. Rate of penetration is a function of different factors of drilling such as the bit type, type of formation being drilled, type of drilling fluid, rotary speed, and weight on bit; so there is need to be able to manage the penetration rate in order to get a better drilling performance.

Prediction of the ROP of a new well is possible by applying the model obtained from an old nearby well using multiple regression data analysis approach. This thesis has been able to verify the approach.

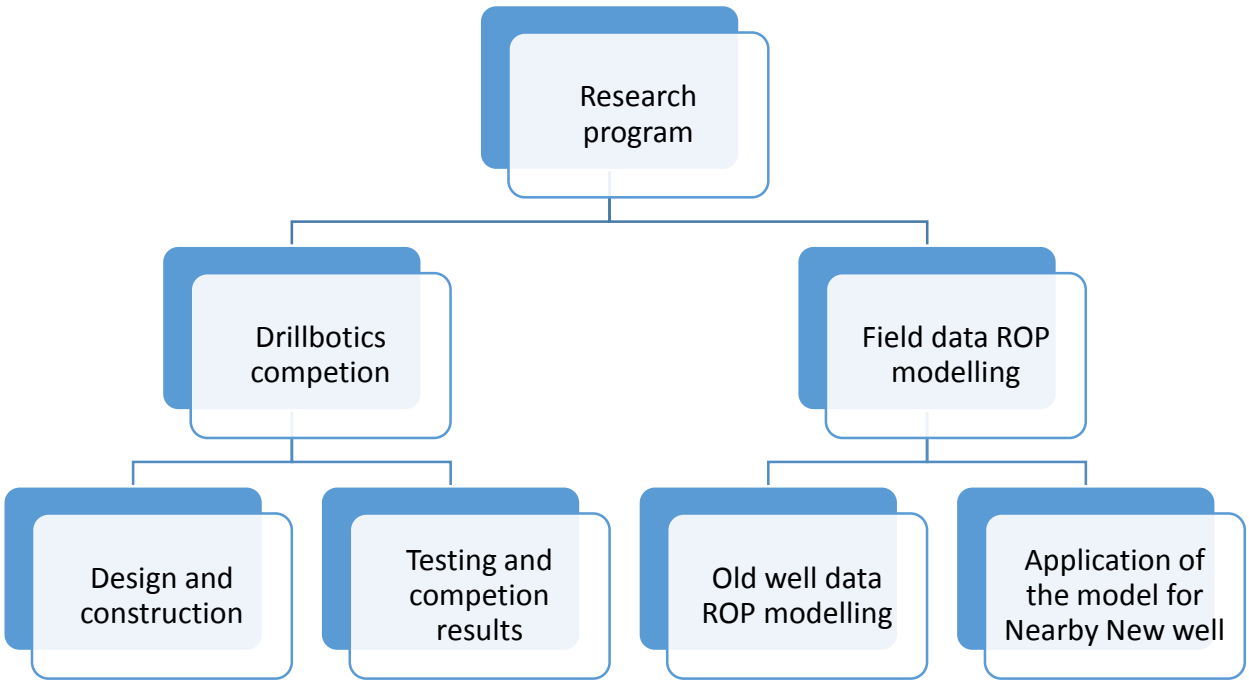

Figure1.3: Structure of the thesis

2 LITERATURE STUDY

This chapter presents some of the theories behind the concept of drilling with respect to rate of penetration in drillbotics. Herein is a description of rock strength and failure mechanism with focus on PDC bit. Described also are the factors that affect ROP and different ROP models. The science involved in hydraulic and circulation systems are equally highlighted; together with the analysis of the deformation of drill string to avoid its damage.

2.1 Rock Strength

Characterization of rock strength is maybe the most important when selecting the optimal type of completion in reservoirs [2]. It is important that rock strength analysis quantifies drillability for a specific formation. The highest quality rock strength properties are usually obtained from the laboratory by stress-loading the rock sample to yield and failure.[2] The tensile strength of rock is quite small, usually of the order of 10% of the compressive strength, so a rock material is more likely to fail in tension than in compression. [3]

Rock strength is often referred to Uniaxial Compressive Strength (UCS). This is the maximum axial compressive stress that the rock material can withstand before failure under unconfined condition, usually atmospheric pressure. [4]

Confined compressive strength (CCS) is another parameter used to characterize the strength of a rock formation. This analysis measures the maximum resistance value with respect to a specified confined load condition. The strength value obtained from CCS is usually higher than UCS. [4]

UCS can be measured directly in the laboratory by subjecting the rock sample to an axial load, or prediction indirectly by correlations. The use of indirect predictions is more favorable as they are cost effective and easier. These indirect methods are often based on regression techniques, simple index parameters and fundamental physical properties of the rock. Parameters commonly used in the correlations are point load index test, p-wave or ultrasonic velocity and Schmidt hammer rebound number.[4] The correlations are most often subjective to the formation type and geographical location, so some can under-predict or over-predict UCS.

McNally also proposed a correlation using least square regression for coal mine rock strength in Australia. [5]

$$UCS = 329.100e^{-0.0505t} \quad \text{.....2.1}$$

Where UCS is in psi and t is the travel time of p-wave in (μs/ft) [5]

An empirical formula to estimate UCS based on sonic logs as a function sonic travel time and porosity for a carbonate formation was proposed by [6]. This is based on the fact that rock strength is a resultant contribution of grain texture, cement texture, porosity, fluid content and degree of compaction. [6]

$$UCS = 194.4 - 0.6072\Delta t - 646.1\emptyset - 0.01644\Delta t^2 + 8.792(\emptyset.\Delta t) \quad \text{.....2.2}$$

Where UCS is in MPa, Δt is sonic travel time in (μs/ft) and $\emptyset$ is the porosity.
Porosity, not only the sonic travel time was considered in order to get continuous log strength along the wellbore. [6]

2.1.1 Rock failure mechanism during drilling

Bit design and selection largely depend on the failure mechanism of formation rock. Formation rock could be in brittle or ductile mode. This depends on the rock strength, which is actually dependent on the composition and downhole conditions like depth, pressure and temperature. [3] *Figure 2.1* shows the failure modes of formation rocks. By brittle mode, the rock fails by fracturing with little or small deformation, while for ductile/plastic mode, failure is by yielding with large deformation until rupture. [3, 7]

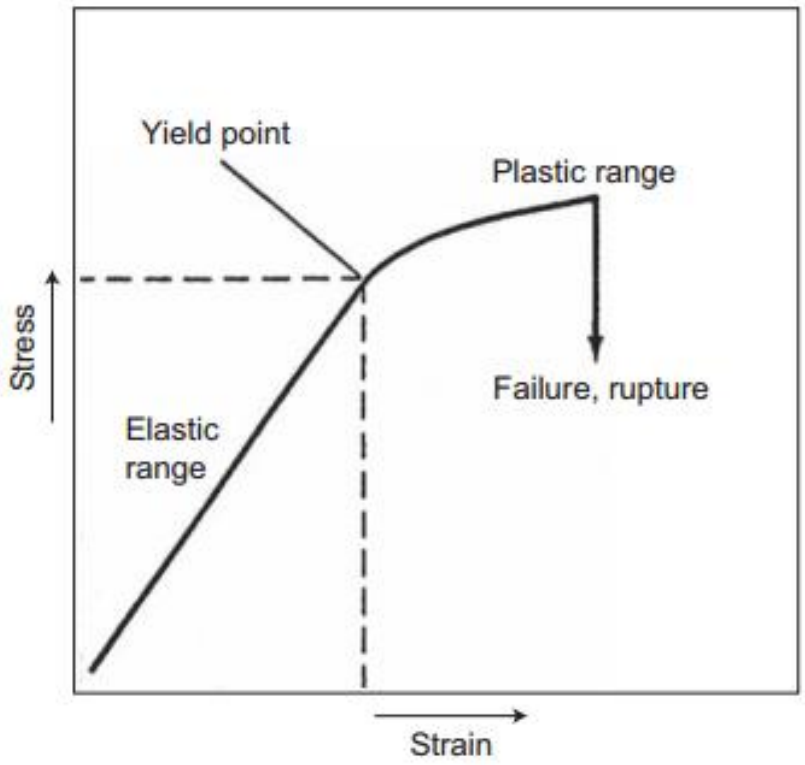

Figure 2.1: Stress-strain curve of a rock formation.

Mechanisms of rock removal of breaking by drill bit include, shearing, grinding, erosion by fluid jet action and crushing. Roller-cone bits break formation rock by crushing, while fixed cutters/PDC's break by shearing mechanism.

2.2 Drill Bits

In order to fully understand the performance and interaction of the different bit types with the formation, it is important to understand the basic components and how the bits are designed. This section explains basic design principles of fixed cutter bits, even though there are many other bits available on the market. [7, 8] Different bits types available are:

- Polycrystalline Diamond Cutter (PDC) bits
- Roller-cone bits
- Drag bits
- Core bits

- The Surface Set Natural Diamond Core Bit
- Impregnated Diamond Core Bits
- PDC Core bits
- Kymera bits

A PDC bit has been used in this thesis.

2.2.1 PDC design review

This bit type has no moving parts, as there is no bearing. Mechanism of breaking the formation is by shearing as compared to crushing for roller cone. The basis of designing an efficient PDC bit can mainly be attributed to: [9]

- Cutter durability
- Depth of cut management
- Build Up rate & dog-leg severity
- Back rake allocation
- Chamfer angle
- Bit stability
- Hydraulic efficiency

Cutter durability: This feature is one of the most critical in PDC design. It is important that cutters demonstrate good resistivity to wear, achieved either by increasing the back rakes or increasing the chamfer angle as shown in *Figure 2.2*. Laboratory tests showed that this reduces the aggressiveness but in turn increases the cutter life longevity due to premature wear flats. [9]

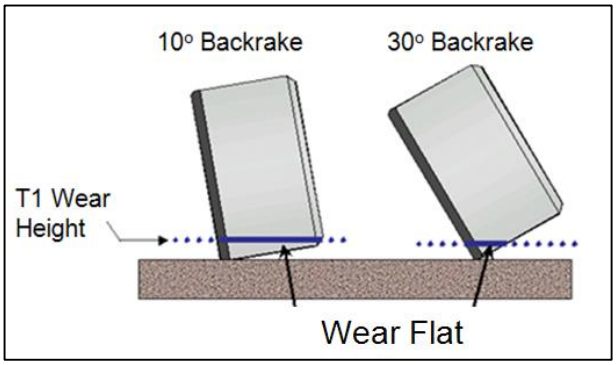

Figure 2.2: Back rake angle impacts wear flat generation

Depth of cut management: This is the way that the distance of the cutter exposure per revolution is managed within the formation. The depth of cut is managed in the cone by allowing the blade surfaces to contact with the formation (ref: *Figure 2.3*). The advantage of this feature helps control torque variation and acts as a torque limiter. This is designed to moderate aggressiveness, increase tool face control, WOB fluctuations while transitioning in formation. In real time this prevents stalling of motors. As cutters placed in a PDC bit's cone do not wear to a larger extent, the contact area and standoff are relatively constant. [7] [9]

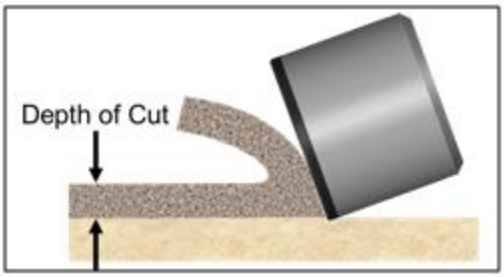

Figure 2.3: Depth of cut

Build Up rate & Dog-leg severity: Build up rate allocation requires different angles of side cut and would need to relate to the BHA and formation type. Side cutting angle (SA) is engaged by a bit feature known "Active gauge" or "Lateral Aggressiveness", (ref: *Figure 2.4).* [10]

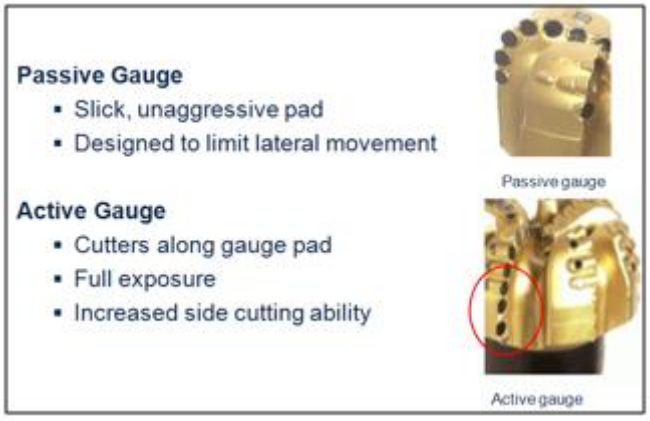

Figure 2.4: Active gauge versus Passive gauge

Back rakes: It is mandatory to set a balance as the cutter back rake varies throughout the bit profile. A higher back rake tends to decrease efficiency and allocate more forces into the substrate while increasing cutter life, as seen in *Figure 2.5*. Laboratory results have suggested

that the lower aggressive back rakes require lesser WOB for a given torque value and hence deemed more efficient. In other words the lower the back rake angle for a given penetration rate, the lower specific energy required to remove unit volume of rock at the respective DOC. [7]

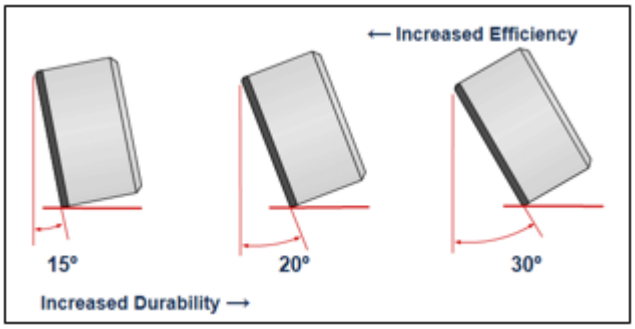

Figure 2.5: Cutter backrake angle vs efficiency

Chamfer angles: Chamfer angle is adjusted by increasing or decreasing the height and small edge chamfer of the diamond bit. This is designed into the diamond bit to increase the cutter durability. It has been proven that smaller chamfers require lesser energy to fracture a given rock, but are more susceptible to early wear depending on the type of formation. [9]

Bit stability: Bit stability is involves managing the cutter design. For a given DOC a respective torque imbalance is generated. The torque imbalance relates to the net torque on individual cutters to the applied WOB. There are profile techniques such as low imbalance, kerfing, high imbalance etc. that are being employed to overcome whirling or lateral instability. [10]

Hydraulic efficiency: This is achieved by reducing the highest possible amount of particles in a given time frame. Typically, a turbulent flow regime is preferred at the bit. This is engineered by optimizing the junk slot area (JSA), increasing the pinch point ratios, evaluating cuttings trajectory and planning for high hydraulic horsepower per square inch (HSI) for a given flow rate. (See *Figure 2.6*) [11]

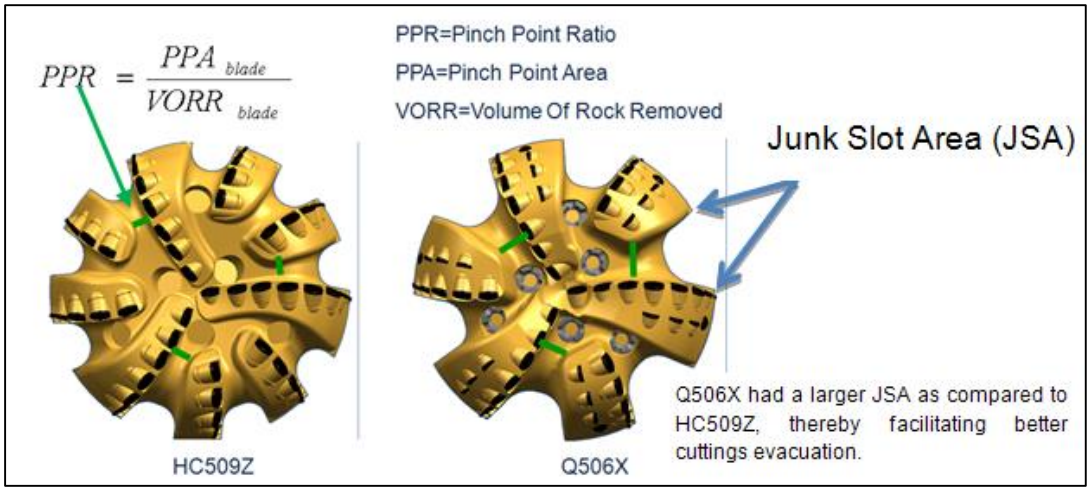

Figure 2.6: PDC hydraulic efficiency using larger pinch points (PPR) and junk slot area (JSA)

2.2.2 Shearing Mechanism of a PDC Bit

The cutting mechanism of PDC bits primarily is shearing, rather than crushing as the case of roller cone. There is sufficient axial load on the cutters to penetrate into the rock surface and sat the same time have the available torque for bit rotation. The resultant force describes a plane of thrust for the cutter. Depending on the rock strength, cuttings are then sheared off at an initial angle with respect to the plane of thrust. (*Figure 2.7*). [7] [12] Rock breakage requires less energy, thus less WOB than roller-cone bits, however higher rotational speed is required. [12]

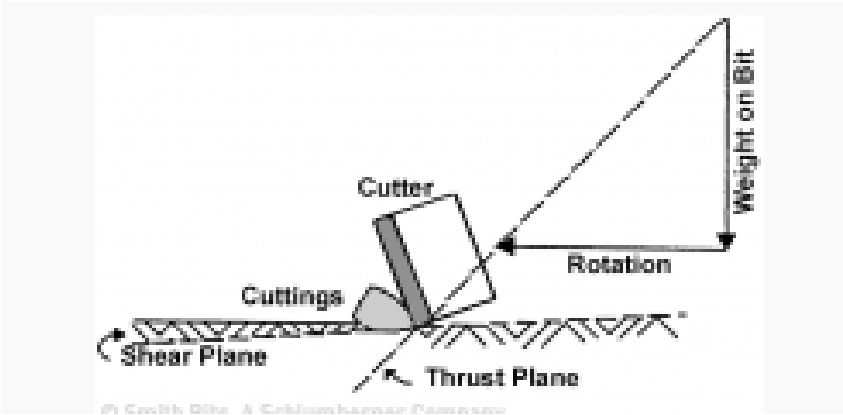

Figure 2.7.: Shear and thrust on a cutter

Angle at which cutter is placed (backrake) affects the aggressiveness of the bit. High angle implies less aggressiveness and vice versa. The bit cutters are strategically positioned on the face of the bit so as to ensure overall bottomhole coverage (ref: *Figure 2.8*) below.

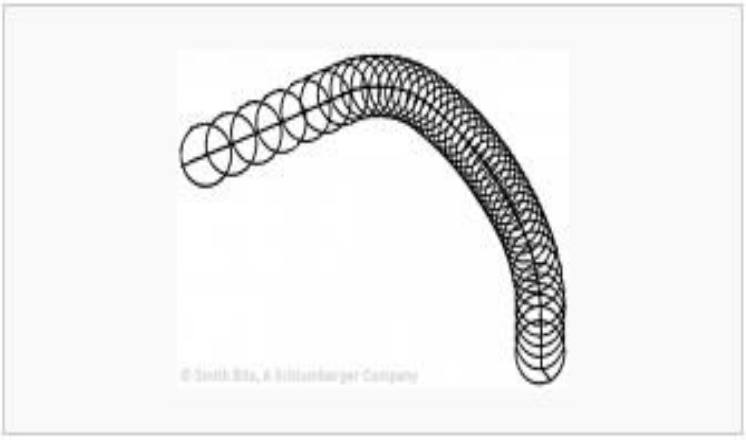

Figure 2.8: Planar representation of cutter density increase with radial position

Reducing the number of cutters on the face of a bit yields: increase in the depth of cut, increase in ROP, increase in torque but reduces bit lifespan. While increasing number of cutters leads to, decrease in ROP, decrease in cleaning efficiency, but increase in bit lifespan. [12] So the need to optimize the number of cutters in order to achieve desired ROP, efficient hole cleaning and appreciable bit lifespan.

The depth of cut of a PDC bit is determined by the rock strength, the WOB applied and the dull condition of the bit. If we express the cut geometry in terms of bottom hole cutting angle or helix angle, $\propto$. [7]

$$\tan \propto = \frac{l_p}{2\pi r} \qquad \text{.....2.3}$$

l_p is the cutter penetration per revolution, while r is the radius from the center of the hole.

According to Mohr-Coulumb failure criterion, yielding or fracturing of rock sample should occur when the shear stress is higher than the sum of the cohesive resistance of the rock and the frictional resistance of the fracture plane. [7] This is mathematically expressed as:

$$\tau = \pm(c + \sigma_n \tan\theta)$$

…….2.4

τ is the shear stress at failure, c is the cohesive resistance of the rock, σ_n is the normal stress at the failure plane and θ is the angle of internal friction. (Ref: *Figure 2.9*) At least two compression tests are conducted at different confining pressures to get the circles and a tangent line is drawn to the circles to get the equation. [3] [7]

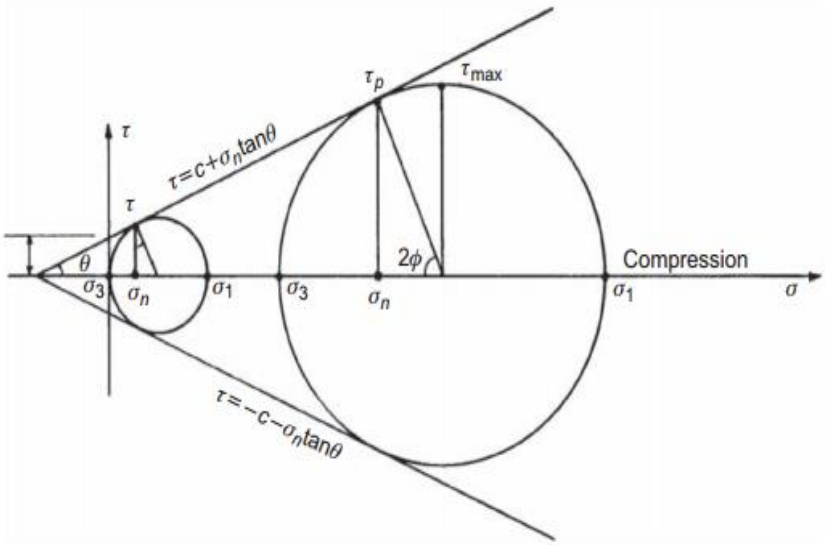

Figure 2.9: Mohr's circle representation of Mohr failure criterion

2.3 Factors affecting rate of penetration (ROP)

Rate of penetration is usually used to describe the speed with which the drill bit breaks the formation rock while drilling [13]. Unit is in feet per hour (ft/hr) or meters per hour (m/hr). There is need to have a sufficient speed to break the formation, and at the same time limit the speed to avoid several problems with the bit and drilling operation. [7]

The following factors are known to affect rate of penetration:

- Type of bit,
- Formation properties,

- Properties of drilling fluid,
- Operating conditions of bit (bit weight and rotary speed)
- bit tooth wear,
- bit hydraulics.

Bit Type: This has great effect on rate of penetration. Roller cone bits often have highest initial ROP in a given formation rock when bits with long teeth and a high cone-offset angle are used; though these bits are not practical in hard rocks, they are in soft formations, dues to quick tooth damage and decline in penetration rate. [13]

Fixed cutter bits, including PDC bits break rocks by shearing, and the bit penetration per revolution depends on number of cutters and backrakes. Improvement in PDC bits design have resulted into higher ROP, efficient bits and reduction in bit balling. [7]

Formation Characteristics: The strength of a formation, both the elastic and the ultimate are the most important properties of a formation that affect ROP. Studies have shown that the compressive shear strength of a given rock could be correlated to the threshold force required to initiate drilling in the rock at atmospheric pressure. This shear strength can be predicted using the Mohr-Coulomb failure criterion, which can also be used to characterize the formation. [14]

The formation permeability also plays a vital role on penetration rate. The drilling filtrate propagates ahead of the bit into the rock, and thus equalizes the pressure differential acting on the chips underneath each tooth. [7]

Another formation property that affects ROP is the mineral composition. Rocks with hard, abrasive minerals can cause quick dulling teeth, while those that have gummy clay minerals can cause balling and reduce efficiency. [7]

Properties of drilling fluid: The following drilling fluid properties are reported to affect ROP:

- Fluid density
- Rheology

- Filtration characteristics
- Solid content and size distribution
- Chemical composition

ROP tends to decrease with increasing fluid density, viscosity and solid content, and increases with increasing filtration rate.[13] Differential pressure across crushed zone is controlled by the density, solid content and filtration properties of the mud; while the parasitic pressure losses in the drill string and hydraulic energy across the bit nozzles are controlled by the viscosity. Chemical composition affects hydration rate and bit balling of some clays, which in turn affects penetration rate. [7]

Operating conditions: Operating conditions such as weight on bit and rotation speed affect penetration rate in a unique way. This effect has been studied by various authors both in the laboratory and in the field. *Figure 2.10* shows the relationship between ROP and weight on bit obtained experimentally, with other variables being held constant. Three regions are observed. Region I, with a non-linear relationship between ROP and WOB; there is loss of energy expended by the bit to shear the rock due to inadequate depth of cut. Region II, showing a linear relationship indicating and efficient bit operation; efficiency is observed to be between 30-40%. Region III, with a drop in ROP with increasing WOB; point of drastic change is referred to as founder point**.** The founder could be as a result of poor hole cleaning, bit balling and vibrations (to be discussed later)

Similar plot for ROP vs rotary speed is as shown in *figure 2.11*, with all other variables also held constant. ROP usually increases linearly with RPM at low values of RMP. However at higher values, the response of ROP decreases, also due to poor hole cleaning. [15]

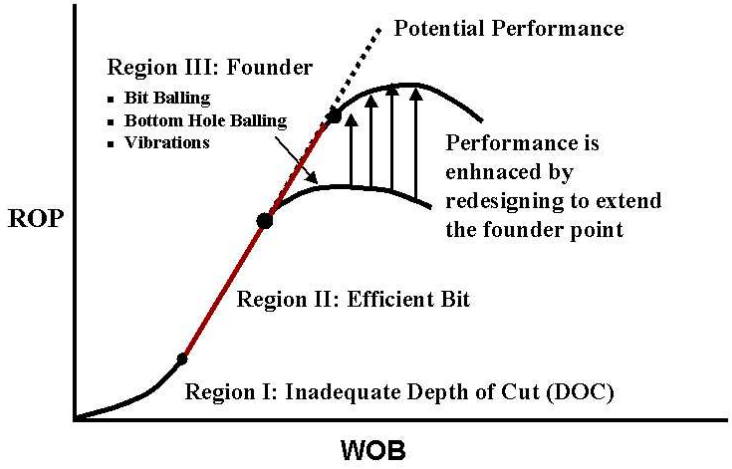

Figure 2.10: Plot showing the efficiency of bits. Bit is efficient if ROP responds linearly to WOB. Performance is enhanced by extending the founder point. [15]

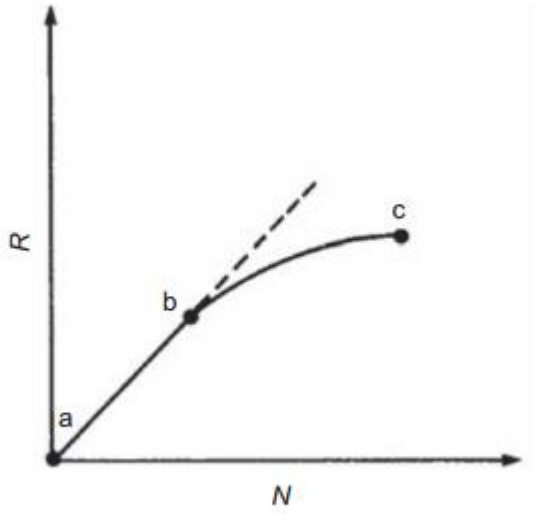

Fig. 6.47—Relation between ROP and rotation speed (Bourgoyne et al. 1991).

Figure 2.11: Relationship between ROP and RPM. Similar to figure 2.10. [7]

Bit Tooth Wear: During drilling, most bits drill slower because the tooth length is continually reduced by abrasion and chipping. For tungsten carbide insert type of roller-cone, the bits fail by breaking rather than by abrasion. [7]

The reduction in ROP as a result of bit wear is normally not as severe for the insert bits as for a milled tooth bit, unless several teeth are broken. Diamond and PDC bits are also known to fail from either cutter failure or the loss of diamonds from the matrix. [7]

Galle and Woods (1963) proposed a model to compute the effect of tooth wear on ROP for roller-cone bits: [7]

$$ROP \propto \left(\frac{1}{0.928125h^2 + 6h + 1}\right)^{a_7} \quad \ldots\ldots\ldots\ldots\ldots\ldots 2.5$$

Where:

h = fractional tooth height worn away

a_7 = exponent = 0.5 was recommended for self-sharpening wear of milled tooth bits. Borgouyne & Young also suggested a similar, but simple relationship (to be discussed later)

$$ROP \propto e^{-a_7 h} \quad \ldots\ldots\ldots\ldots\ldots\ldots 2.6$$

Bit Hydraulics: In 1953, introduction of the jet type roller cone bits has shown that substantial improvements in ROP could be achieved by the improving the jetting action at the bit, as there is better cleaning of the bit and the hole. Historically, bit hydraulic horsepower, jet-impact force, flow rate and nozzle velocity play important role in characterizing the effect of hydraulics on bit performance. This in turns affects the penetration rate. [7]

2.4 ROP Models

Several models have been developed to account for all these factors in order to optimize ROP and to have an efficient, save and cost effective drilling operation.

2.4.1 Mechanical Specific Energy (MSE)

Teale in 1965 proposed MSE as the energy needed by the drill bit to efficiently destroy a volume of rock as drilling operation proceeds. This expresses the relationship between input energy and penetration rate.[15]

$$MSE = \frac{Input\ Energy}{Output\ ROP}$$

……2.7

He equally observed that MSE value was numerically equal to the uniaxial compressive strength of the rock sample in *psi*. The following equation was proposed, which includes the drilling operating conditions, i.e. the weight on bit *(WOB)*, rotary speed *(N)*, bit torque *(T)* and drill bit diameter *(d_b)* [15, 16]

$$MSE = \frac{4WOB}{\pi d_b^2} + \frac{480 * N * T}{d_b^2 ROP} \approx UCS$$

……2.8

The expression was arrived at by considering a rotary non-percussive drilling, with the work done in one minute by the thrust, F *(Ib)* and torque, T *(Ib)* due to the indentation and rotation actions. If the rotary speed is N *(rev/min)*, area of hole is A *(in^2)* and penetration of u *(in)* in one minute, and then dividing the total work done by the volume of rock drilled, Au (in^3).[16]

$$e = \frac{F}{A} + \frac{2\pi}{A}\frac{NT}{u}$$

……2.9

An improvement on this equation was proposed by Dupriest to adjust the MSE by including a mechanical efficiency factor(EFF_M). [15]

$$MSE_{adj} = EFF_M * MSE$$

……2.10

$$MSE_{adj} = EFF_M \left(\frac{4WOB}{\pi d_b^2} + \frac{480 * N * T}{d_b^2 ROP}\right) \approx UCS$$

……2.11

MSE can be monitored to ensure drilling efficiency by detecting when it changes. [15] An increase in MSE results in a higher demand of work to drill and thereby a lower drilling

efficiency. As indicated in earlier section 2.3 under operating conditions, drill bit efficiency ranges from 30-40%, before the founding point is reached.[15] However in the industry, a uniform value of 0.35 of EFF_M has been set irrespective of the bit type or weight on bit. [17] Large sources of error are observed while calculating MSE from surface measurements, making the field plots being used only quantitatively as a trending tool. Any error is observed to uniformly shift the curve, which still makes it useful as a visual trending tool. [17]

The torque at the bit can be measured in the laboratory and by a MWD system in the field, but in most cases the measurements does not exist. Pessier & Fear, 1992, related the bit torque to the WOB and coefficient of friction, μ. [18]

$$T = \frac{\mu . d_b . WOB}{36} \quad \ldots\ldots\ldots\ldots\ldots\ldots 2.12$$

Caceido & Calhoum, 2005 proposed an empirical model for the friction factor relating it to formaton strength. [18]

$$\mu = 0.9402\exp(-1.16 * 10^{-9} * CCS) \quad \ldots\ldots\ldots\ldots\ldots\ldots 2.13$$

Substituting in the adjusted MSE, and making ROP subject of the equation, we have the following:

$$ROP = \frac{13.33\mu . N}{d_b \left(\frac{MSE_{adj}}{EFF_M . WOB} - \frac{4}{\pi d_b^2} \right)} \quad \ldots\ldots\ldots\ldots\ldots\ldots 2.14$$

2.4.2 Borgouyne & Young ROP Model

Initial drilling models proposed for drilling optimization were largely established upon limited data and imprecise results. Bourgoyne & Young introduced a ROP model that is considered the most appropriate for real-time drilling optimization and an essential optimization method as it depends on statistical past drilling values.[19, 20] The modeling is done by a multiple regression analysis of the past drilling data, including effects of variables, to produce the rate of penetration.

The model considers the relationship between the ROP as a function of several drilling variables. The variables are: formation characteristics, sediment compaction with depth, under-compaction experienced in abnormal pressured formation, bit type, impact force, bit weight, RPM, drilling fluid properties and bit hydraulics. [19, 20]

The model can be mathematically expressed with the exponential function integrated as:

$$ROP = f_1 * f_2 * f_3 * f_4 * f_5 * f_6 * f_7 * f_8 \quad \ldots\ldots\ldots\ldots\ldots\ldots 2.15$$

Where the functions f_1 to f_8 are expressed as normalized effects of the above-listed variables on ROP; and are functions of experimental model constants a_1 to a_8 chosen on the basis of prevailing drilling conditions. [7, 21]

f_1, models the formation strength and bit type effects,

$$f_1 = e^{2.303a_1} \quad \ldots\ldots\ldots\ldots\ldots\ldots 2.16$$

f_2, the effect of increase in rock strength due to normal compaction with depth (D in ft),

$$f_2 = e^{2.303a_2(10{,}000-D)} \quad \ldots\ldots\ldots\ldots\ldots\ldots 2.17$$

f_3, the effect of under-compaction due to abnormal pressured formations,

$$f_3 = e^{2.303a_3D^{0.69}(g_p-9)} \quad \ldots\ldots\ldots\ldots\ldots\ldots 2.18$$

where g_p – the pore pressure gradient in pound per gallon equivalent.

f_4, the effect of overbalance on ROP, produced by increase in mud weight,

$$f_4 = e^{2.303a_4D(g_p-\rho_c)} \quad \ldots\ldots\ldots\ldots\ldots\ldots 2.19$$

where ρ_c = mud weight in pound per gallon.

f_5 , models the effect of WOB,

$$f_5 = \left[\frac{\left(\frac{WOB}{d_b}\right) - \left(\frac{WOB}{d_b}\right)_t}{4 - \left(\frac{WOB}{d_b}\right)_t}\right]^{a_5}$$

……..2.20

Drill-off tests are used to estimate the threshold bit weight, $\left(\frac{WOB}{d_b}\right)_t$, and bit weight exponent values have been reported to vary from 0.6 to 2.0. [19]

f_6 , the effect of rotary speed, RPM (i.e. N) on the ROP,

$$f_6 = \left(\frac{N}{60}\right)^{a_6}$$

……2.21

f_7 , the effect of bit wear on the ROP,

$$f_7 = e^{-a_7 h}$$

…….2.22

where, h = fraction of bit wear

$$h = \frac{(Depth_{Current} - Depth_{in})}{(Depth_{Out} - Depth_{in})} * \frac{DG}{8}$$

……2.23

DG is the IADC dull grade to indicate the condition of bit wear that is reported when the bit is pulled out. Has a value from 0 – 8.

f_8 , the effect of bit hydraulics on the ROP,

$$f_8 = \left(\frac{F_j}{1000}\right)^{a_8}$$

……2.24.

where, F_j is the hydraulic impact force beneath the bit in Ib_f. Based on Eckel's microbit experiments [22], Eckel discovered that the ROP was proportional to Reynolds number group $\left(\frac{\rho q}{\mu . d_n}\right)^{0.5}$. Here ρ is mud density [lb/gal], q is flow rate [gal/min], μ is the apparent viscosity [cp], and d_n is the bit nozzle diameter [in].

$$F_j = \frac{pq}{0.35\mu . d_n} \qquad \ldots\ldots\ldots\ldots\ldots\ldots 2.5$$

2.4.3 Real-time bit wear model

Borgouyne & Young defined ROP as the effect of eight functions as stated above. The equation may be inverted to obtain the formation drillability stated as the function f_1 (in ft/hr.) While drilling data such as RPM, ROP, WOB, mud weight, pore pressure and flow rate obtained from offset well data at each depth of meter or foot being drilled may be used to estimate the rock drillability value. [9, 21]

The fractional bit wear is simplified and assumed as linear decreasing trend vs. depth using the expression given by:

$$h = \frac{(Depth_{Current} - Depth_{in})}{(Depth_{Out} - Depth_{in})} * \frac{DG}{8} \qquad \ldots\ldots\ldots\ldots\ldots\ldots 2.26$$

Where DG is the IADC dull grade bit wear state that is reported when the bit is pulled out. Has a value from 0 – 8.

2.4.4 Maurer model

According to Maurer, a theoretical equation for roller-cone bits relating the ROP to WOB, RPM, bit size and rock strength was developed. The assumption of perfect bottomhole cleaning as well as incomplete bit tooth penetration was considered. The equation was based on observations made in single tooth impact experiments: [7]

1. The crater volume is proportional to the square of the depth of cutter penetration.

2. The depth of cutter penetration is inversely proportional to the rock strength.

Details of the model is presented in the *Appendix A.*

2.4.5 Perfect-cleaning model

This is a ROP model for soft formation using roller cone bits, developed by Warren and later modified by Hareland and Hoberook. The model correlates ROP to WOB, RPM, rock strength and bit diameter from dimensional analysis and generalized response curves. Principle of steady-state drilling conditions (otherwise called perfect cleaning) is employed, where rate of cutting removal from the bit and rate at which new chips are formed are equal. This implies that ROP is controlled by cutting-generation process, or cutting removal process or both. [13] [23]. The dimensionless bit constants in the model are based on experiments

2.4.6 Imperfect-cleaning model

In field cases, ROP is significantly inhibited by the rate of cutting removals. Thus a perfect cleaning is not ideal. The model is a modification of the Perfect-Cleaning model. It consists of the modified impact force and mud properties in order to take the cuttings removal into considerations.

This indicates that the continuous transition from cuttings generation to cuttings removal is the controlling factor on ROP. The model also shows that as the bit size increases, the impact force must also be increased to achieve a certain level of cutting removal, but the particular nozzle size used becomes less significant with increasing bit size. [13] [23]

2.4.7 Hareland and Rampersad Model

This ROP model is based on PDC bit performance, for 100% efficient bit cleaning. The model includes: a coefficient determined by the bit and blade geometry *(G)*, bit wear function calibrating ROP values for a worn bit (W_f), WOB, RPM, bit diameter and uniaxial rock strength value, (σ). [24] Check Appendix A for details

2.5 Drillability d-exponent

The drillability d-exponent normalizes the ROP by excluding the effects of external drilling parameters like pressure and rock strength. The exponent increases with depth in normally pressured formations, proportionally to the rock strength. When drilling into an abnormally pressured shale however, the exponent decreases with depth. Here the drilling experiences an under-compacted, where the decreased density and increased porosity results in a more drillable formation. With all other drilling parameters unchanged, the rate of penetration increases in this section. ROP also increases by having less pressure differential between drilling fluid and pore pressure. These abnormal pressure zones are detected far earlier by a bit with no wear, than a worn down bit. A dull bit may be far into the abnormally pressured zone before the transition is detected. A projected plot of the d-exponent is in *Figure 2.12*. [25, 26]

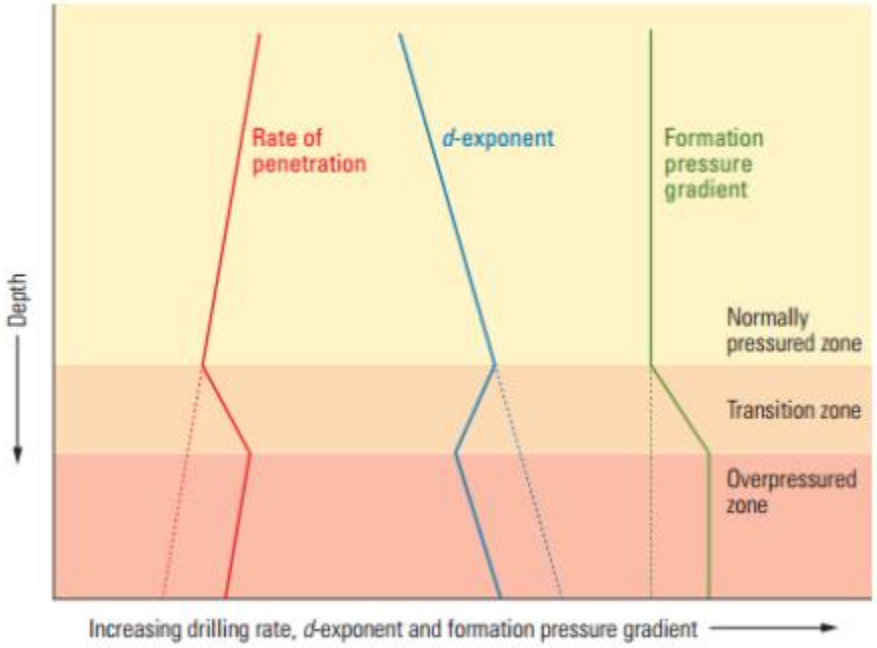

Figure 2.12: D-exponent plot example [59]

The use of changes in ROP values as an indicator of abnormal pressure is not ideal. Therefore, the d-exponent is used to normalize or correct the drilling rate. This gives a more effective indicator of pore pressure and abnormally pressured zones. The basic d-exponent, originated

from the study by Bingham (1965) and Jordan and Shirley (1967) [27], and the mathematical formulation is given as follows.

$$d = \frac{\log\left(\frac{ROP}{60RPM}\right)}{\log\left(\frac{12WOB}{10^3 d_b}\right)} \qquad \text{……..2.27}$$

Here, ROP is in feet/hr, WOB is in kilo pound, while $d_b$is in inches. This equation tries to correct the rate of penetration for changes in WOB, RPM and hole size. In 1971, Rehm et al. [28] produced a corrected d-exponent (d_{corr}) for changes in mud weight.

$$d_{corr} = d\left(\frac{NPP}{ECD}\right) \qquad \text{……2.28}$$

Here, NPP is normal pore pressure gradient, and ECD is equivalent circulating density. This correction is universally used as it makes the exponent more sensitive to mud weight changes and increasing pore pressure, even though it still lacks thorough theoretical basis [25].

Three limitations of the drillability exponent have been expressed [25]:

- The drillability exponent requires clean shale or clean argillaceous limestone.
- Large increase in mud weight results in lower values of the corrected drillability exponent (d_{corr})
- The corrected drillability exponent (d_{corr}) is affected by lithology, type of bit, bit wear, poor hydraulics, unconformities, and motor or turbine runs.

2.6 Principles of Multiple Regression

A multiple regression model is a statistical regression model with two or more regression variables [29]. This is also referred to as a multivariate analysis, which characterizes an observation factor by several variables.[30] The method takes into account changes of several

properties simultaneously (in this case, drilling parameters). The multiple regression equation of Y on X_1, X_2, X_3,…, X_n is commonly given by:[31]

$$Y = b_0 + b_1 X_1 + b_2 X_2 + b_3 X_3 + \ldots + b_n X_n \quad \ldots\ldots\ldots\ldots\ldots\ldots 2.29$$

Where b_0 is the intercept and b_1, b_2, b_3, …, b_n are analogues to the slope in linear regression equation, also called regression coefficients. [31] This flexible method of data analysis can be applicable when a quantitative variable is to be examined in relation to other factors.[32] The principle is applicable to model the influence of drilling parameters on ROP, MSE and D-exponent as will be seen later in this report.

2.7 Hydraulics

Fluids are basically classified into two major categories, Newtonian and non-Newtonian. *Figure 2.13* below shows the different classifications. Newtonian fluid has the shear stress (τ) directly proportional to the shear rate ($\dot{\gamma}$), which implies viscosity (μ) is independent on the shear rate. Examples of Newtonian fluids are water, air and benzene. [7]

$$\mu = \frac{\tau}{\dot{\gamma}} = constant \quad \ldots\ldots\ldots\ldots\ldots\ldots 2.30$$

While for a non-Newtonian fluid, the shear stress varies non-linearly with the shear rate. It implies that viscosity is dependent on the shear rate and could even be time-dependent. Examples of non-Newtonian fluids are most drilling fluids, blood, toothpaste and paint.

$$\mu = \frac{\tau}{\dot{\gamma}} = not\ constant \quad \ldots\ldots\ldots\ldots\ldots\ldots 2.31$$

There are different models to study the shear stress of non-Newtonian fluids. (Ref: *Figure 2.13*) [7] We have the:

1. Bingham plastic model, which show a linear relationship between shear stress and shear rate as shown in *Figure 2.13*, τ_0 is the yield stress needed to be overcome in order for the fluid to flow, and (μ_p) is called Bingham plastic viscosity in (cP)

$$\tau = \tau_0 + \mu_p * \dot{\gamma}$$

……..2.32

2. Power law model, which gives a good description of fluid flow properties. It includes proportionality constant (*K*) and flow behavior index (*n*).

$$\tau = K * (\dot{\gamma})^n$$

…….2.33

3. Herschel-Bulkley model, which combines Bingham and Power law models

$$\tau = \tau_0 + K * (\dot{\gamma})^n$$

……..2.34

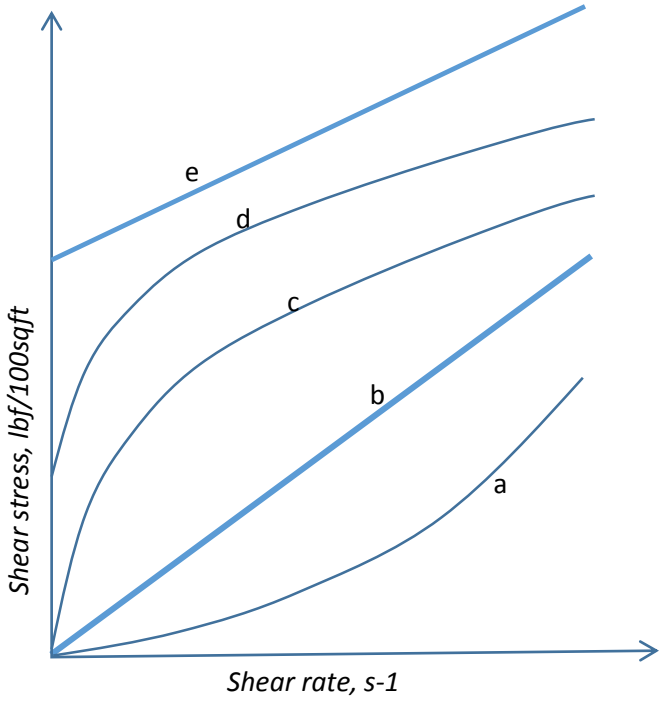

Figure 2.13: Classification of fluids with shear stress as a function of shear rate.

(a: Dilatant b: Newtonian, c: Pseudoplastic, d: Real fluid , e: Bingham)

Viscosity is a measure of the resistance to the flow of a fluid or the resistance to the movement of an object through a fluid. It is measured in Pa.s or centi poise (cP).

For the purpose of this work (i.e. DrillBotics), we will consider water as drilling fluid, with constant viscosity of 1.002e-3 Pa.s

Density of fluids varies with changing temperature and pressure. But in Drillbotics, we are assuming density of 998.2 kg/m^3 at room temperature of 20 ^{0}C and atmospheric pressure.

2.7.1 Flow regimes (wrt Reynolds number)

Reynolds number gives an indication of the type of flow regime we are. This is the ratio of inertial resistance to viscous resistance for a flowing fluid.

$$Re = \frac{\rho u D}{\mu} \qquad \text{.....2.35}$$

Laminar flow regime: This is a flow regime dominated by viscous flow with $Re \leq 2000$. The flow is smooth and also constant.

Turbulent regime: This is characterized with chaotic and instable flow, with $Re \geq 4000$. It is however dominated by inertial forces, as compared to viscosity in lamina.

Transition regime, on the other hand has Reynold's number in-between lamina and turbulent flow. i.e. $2000 < Re < 4000$. The flow properties are neither lamina nor turbulent. Hence an interpolation is employed to characterize the flow.

2.7.2 Friction Factor

Depending on the flow regime we are, there are different friction factor models used in order to calculate the pressure drop in the section of concern. Darcy-Weisbach friction factor, f_D should never be confused with Fanning friction factor, f. Darcy-Weisbach friction factor, commonly applied by civil and mechanical engineers, is 4 times larger than the Fanning friction factor, which is commonly used by chemical engineers. [33]

$$f = \frac{f_D}{4}$$

…….2.36

For a lamina flow, Darcy-Weisbach friction factor is used according to the equation below.

$$f_D = \frac{64}{Re}$$

…….……2.37

However for turbulent flow regime, the original Colebrook-White relation is used. This is an implicit equation that requires that friction factor be solved by iterations. The expression takes into consideration the roughness of the flow conduit, ε in *mm*. [33]

$$\frac{1}{\sqrt{f_D}} = -2.00 \log\left(\frac{2.51}{Re\sqrt{f_D}} + \frac{\varepsilon/D}{3.7}\right)$$

……2.38

For simplicity and easy calculation, an explicit approximation of Colebrook equation proposed by Haaland can be used. [33] This is given as

$$\frac{1}{\sqrt{f_D}} = -1.8 \log\left(\frac{6.9}{Re} + \left(\frac{\varepsilon/D}{3.7}\right)^{1.11}\right)$$

……..2.39

The friction factor for a transitional flow is obtained by simply doing a linear interpolation between lamina and turbulent flows. This is shown in the expression below, while a Matlab implementation code is shown in *Appendix F-1*.

$$f_D = (1 - x_{int}) * f_{lamina} + x_{int} * f_{turbulent}$$

…….2.40

Where $x_{int} = \frac{Re-2000}{4000-2000}$ and Re is the Reynolds number of the transition flow.

2.7.3 Pressure Drop Equations

Hydraulic pumps are required to pump and circulate drilling fluid from the surface down to the bottom hole through several conduits and finally through the bit. Circulation of fluids in the annulus is equally important in order to remove the cuttings generated during the drilling operation, out of the hole. In the drillbotic setup, we will have the following conduits through which the drilling fluid will pass through. These several conduits (ref: *Figure 2.14*) contribute to the pressure losses (head losses) that must be overcome by the pumps. They are:

- Hose from the pump to swivel
- Swivel
- Drill pipe
- BHA
- Bit
- Annulus

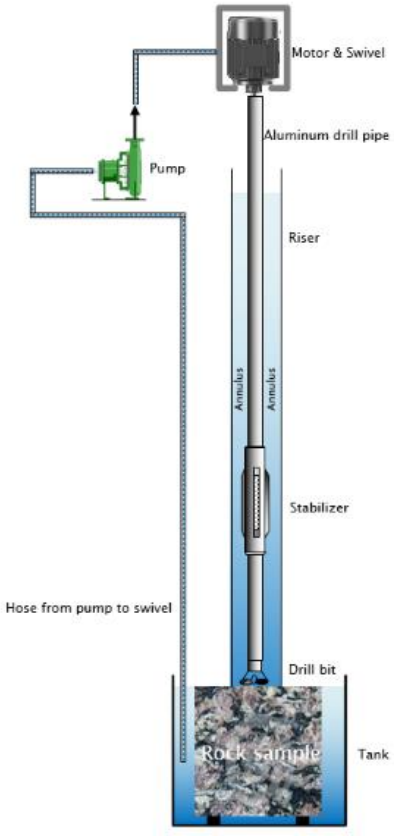

Figure 2.14: Schematic of the hydraulic loop

The pressure loss in each section is calculated using the following expressions.

The General pressure loss equation in a pipe is considered for the hose, drill pipe and BHA sections, and it is given as follows:

$$\Delta P = \frac{\rho u^2 f_D L}{2D}$$

…….2.41

Where the flow velocity $u = \frac{Q}{A}$ and $A = \frac{\pi D^2}{4}$

Thus;

$$\Delta P[Pa] = \frac{\rho u^2 f_D L}{2D} = \frac{\rho Q^2 f_D L}{2D * A^2}$$

……..2.42

$$\Delta P[Pa] = \frac{8\rho Q^2 f_D L}{\pi^2 D^5}$$

……..2.43

Q [m^3/s] is the flowrate, A [m^2] is the cross-sectional area, L [m] is the length of the pipe/hose and D [m] the internal diameter of the conduit.

For pressure lose in the swivel, the following expression is used.

$$\Delta P_{swivel}[psi] = \frac{\rho}{A^2}\left(\frac{Q}{C_v}\right)^2$$

……2.44

Where C_v is the flow coefficient, Q is the flow rate in gpm, A is the flow area in sq. in. and density of fluid ρ in ppg. Sometimes, the density and flow area are factored into the value of C_v, by some manufacturers. For example as indicated by John Henry Foster Company. [34] So we have:

$$\Delta P_{hose}[psi] = \left(\frac{Q}{C_v}\right)^2$$

……2.45

Or simply as

$$\Delta P_{swivel}[Pa] = 6894\left(\frac{0.264Q}{C_v}\right)^2$$

……2.46

where Q is in lpm and $C_v = 5.25$

Pressure loss across the Bit: The expression for the pressure loss across the bit, considering impact force through the jet bit is:

$$\Delta P_{bit}[Pa] = \frac{\rho Q^2}{2A^2 0.95^2}$$

……..2.47

where, $A = \frac{\pi {d_{en}}^2}{4}$, is the total nozzle flow area. If we have more than one nozzle, the total nozzle flow area is the addition, but the equivalent nozzle diameter, d_{en} is obtained as indicated below for *n* number of nozzles. [35]

$$A = A_1 + A_2 + A_3 + \ldots + A_n$$

……2.48

$$d_{en} = \sqrt{d_1^2 + d_2^2 + d_3^2 + \ldots + d_n^2}$$

……..2.49

Pressure loss in the Annulus: Both the drilling fluid and the cuttings generated during drilling contribute to the pressure loss in the annulus. This is evident in the mixture density, mixture viscosity and the annular velocity. In order to have an effective hole cleaning, the annular velocity must be greater than or equal to the settling velocity of the cuttings. This will be discussed later. Similar pressure drop equation used for pipe is equally used, except that the diameter here is the effective flow diameter.

$$\Delta P[Pa] = \frac{8\rho_m Q^2 f_D L}{\pi^2 {D_e}^5}$$

……2.50

Where the equivalent circular diameter D_e, can be obtained using different criteria. Usually, we use the hydraulic radius criterion, where:

$$r_H = \frac{x - sectional\ area}{wetted\ perimeter} = \frac{\pi({r_2}^2 - {r_1}^2)}{2\pi(r_1 - r_2)} = \frac{d_2 - d_1}{4}$$

……..2.51

And thus $D_e = 4r_H = d_2 - d_1 = ID_{hole} - OD_{BHA}$

……..2.52

Note: There are others criteria that can also be used to define D_e (check Appendix)

In the annulus, presence of cuttings suspended in a fluid increases the effective density of the mixture.

$$\rho_m = \rho_f(1 - CC) + \rho_s * CC$$

……..2.53

So also is the effect on the viscosity, provided CC < 0.25. [7]

$$\mu_m = \mu_f(1 + 2.5CC + 10.05CC^2)$$

……2.54

Therefore Reynold's number for the annular flow can be calculated as follows:

$$Re = \frac{\rho_m v D_e}{\mu_m}$$

……2.55

2.7.4 Arrangement of Pumps

In circulation systems, there is need sometimes to use more than one pump connected in series or in parallel. (Ref: *Figure 2.15* and *Figure 2.16*) The serial/parallel arrangement is dependent on what operation we need to achieve. We might need serial connection to overcome higher system

head losses at constant flow rate than one pump can handle. Parallel connection is required if we intend to overcome higher flowrate at constant head loss. [36]

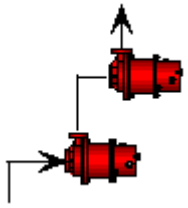

Figure 2.15: Two pumps in series

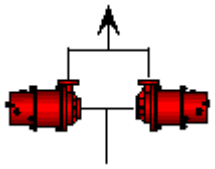

Figure 2.16: Two pumps in parallel

An example of a pump characteristics curve is seen in *Figure 2.17*, where the flow rate decreases as the pressure loss across the pump increases. For pumps in series, the head losses are added to get the combined effect of the arrangement, i.e. the performance curve. (Ref: *Figure 2.18*)
For parallel arrangement, the flow rates are added together instead. (See *Figure 2.19*) [36]

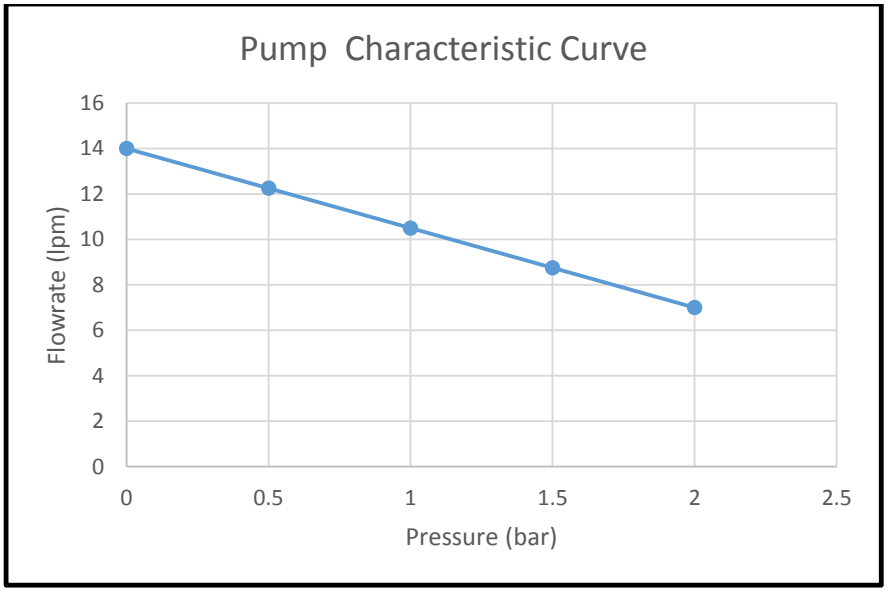

Figure 2.17: Pump characteristics of a 12V water pump (Biletema 25987)

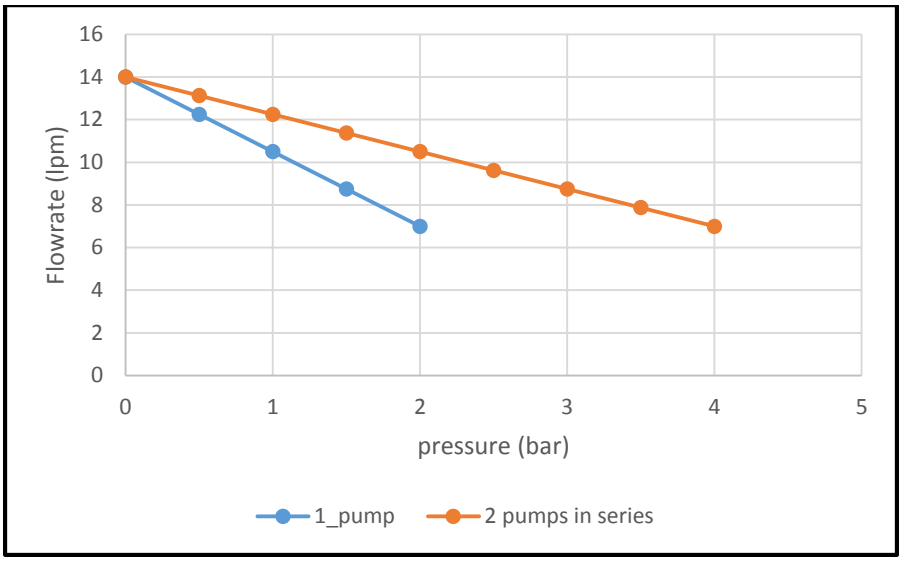

Figure 2.18: Performance curve for two the Biltema water pumps above in series. The pressure heads are added together

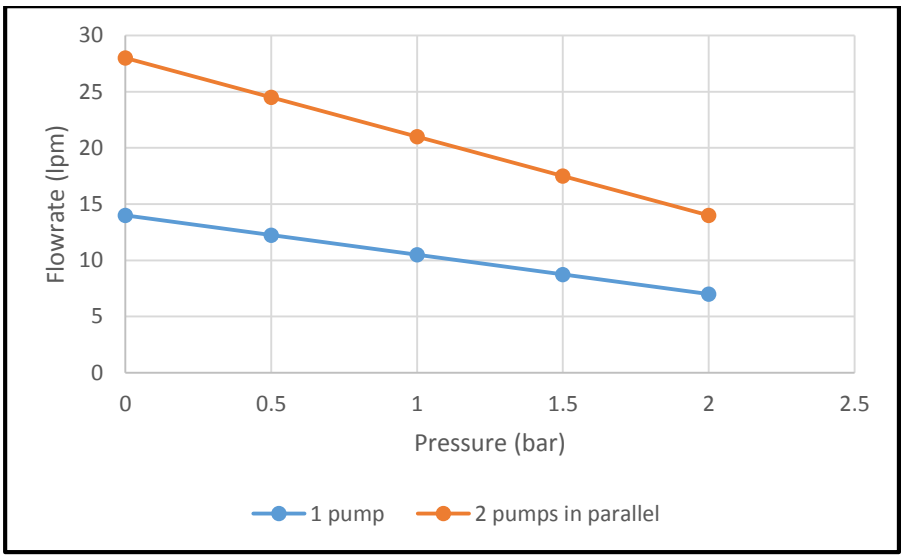

Figure 2.19: Performance curve for two the Biltema pumps above in parallel. The flowrates are being added

2.8 Cuttings Transport

Cuttings transportation out of the annulus is a very important topic in order to avoid many issues during drilling. So the need to establish a minimum annular velocity required to lift the cuttings. In a vertical, Sifferman and Berker suggested that 100 ft/min (0.508 m/s) may be required when drilling fluid is water, while a minimum of 50 ft/min (0.254 m/s) for a typical drilling fluid may be suitable. [37]

Transport efficiency in vertical wells is usually assessed by determining the settling velocity (i.e. cuttings slip velocity) which is dependent on the following: [37, 38]

- Particle size, density and shape
- Drilling fluid rheology, density and velocity;
- Hole/pipe configuration (i.e. annular geometry)
- Pipe rotation and eccentricity

For transport of cuttings to happen, the fluid velocity must be higher that the particle slip velocity.

2.8.1 Settling Velocity of Particles

Settling velocity/slip velocity is the "sinking velocity" for particles in liquid. Empirical equations correlate for factors such as cuttings density, cuttings size, mud weight and viscosity of the mud. This velocity is primarily determined by the relative magnitude of the gravity and the viscous drag forces acting on the particle [7] [39]

Three settling laws are required to cover the possible ranges of settling conditions from low Reynolds Numbers i.e. small particle diameter/high viscosity fluid to settling with high Reynolds Numbers i.e. large particle diameter/low viscosity fluid.

Force in the direction of flow exerted by the fluid on the solid is called drag. *Figure 2.20* shows a stationary smooth sphere of diameter DP situated in a stream, whose velocity far away from the sphere is u to the right. [7]

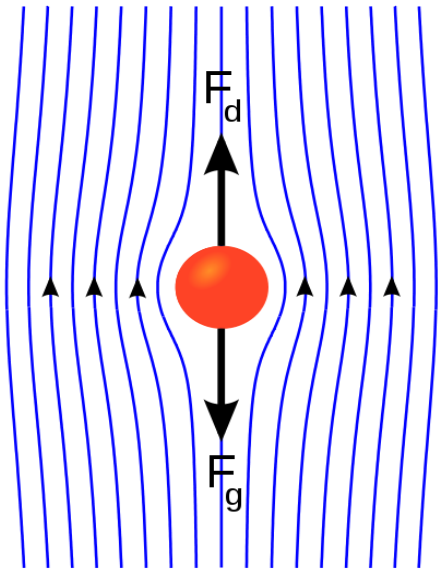

Figure 2.20: Drag forces on a solid particle in fluid

For a spherical grain of diameter d_s and density ρ_s, apparent weight acting due to gravity F_g is: [39]

$$F_g = \frac{\pi}{6} d_s^3 (\rho_s - \rho_f) g \qquad \ldots\ldots\ldots\ldots\ldots\ldots 2.56$$

Where ρ_f = fluid density, g= acceleration due to gravity.

The drag force, which is the primary force associated with the interaction between a moving fluid and an immersed solid sphere is: [39]

$$F_D = \frac{\pi}{8} d_s^2 \rho_f v_s^2 C_D \qquad \ldots\ldots\ldots\ldots\ldots\ldots 2.57$$

Where $C_D$is the dimensionless drag coefficient, which depends on the particle Reynolds number.

Equating *Equations 2.56 and 2.57* gives the particle settling velocity

$$v_s = \sqrt{\frac{4 d_c g (\rho_s - \rho_f)}{3 \rho_f C_D}} \qquad \ldots\ldots\ldots\ldots\ldots\ldots 2.58$$

Particle Reynolds number is expressed as the follows.

$$Re_p = \frac{\rho_f d_s v_s}{\mu} \qquad \text{.....2.59}$$

For values of particle Reynolds number $Re_p < 10^5$, $C_D$can be approximated as *Equation 2.60*, while for $Re_p > 10^5$ C_D of 0.1 can be used: [39]

$$C_D \approx \frac{24}{Re_p}\sqrt{1 + 0.2Re_p + 0.0003{Re_p}^2} \qquad \text{.....2.60}$$

A Matlab implementation code to solve for the settling velocity is shown in *Appendix F-2*.

2.9 BHA Description/ Stabilization Placement

It is important to improve our drilling performance and also to reduce drilling cost. Improving drilling performance implies optimizing the penetration rate, providing adequate depth of cut with appropriate WOB. This is achievable by the optimization of penetration rate through improved understanding of down-hole activities. [40] Methods that can improve ROP include:

1. Limiting the dog-leg severity, while ensuring gradual hole deviation
2. Applying and placement of sufficient stabilizer in the BHA

Reasons for using Stabilizers:

1. Used fundamentally to control the directional behavior of BHA
2. To concentrate weight of the BHA on the bit
3. To minimize bending and vibrations, that can wear and damage components like MWD tools
4. To prevent differential sticking and key seating
5. To prevent drill collar contact with side of the hole, thus reducing drilling torque
6. To prevent loading the bit in any other direction except the hole axis. [41]

2.9.1 BHA Assembly Types

The directional behavior of an assembly is determined by the magnitude and direction of the bit resultant force vector, which is due to the bit side force acting on the formation. (Ref: *Figure 2.21*) The drill bit continues to drill along an equilibrium angle a wellbore maintains in a given formation, until the operating conditions change. An isotropic formation attains an equilibrium angle when the resultant force vector is parallel to the hole axis. For an anisotropic formation, the angle depends on the combination of the resultant force and the drillability of the formation. [40, 42]

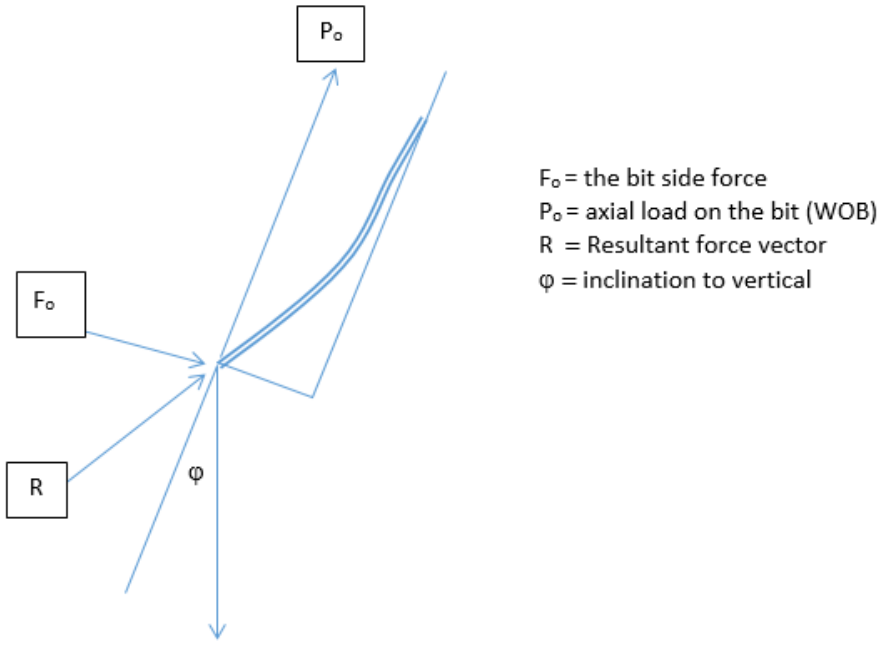

Figure 2.21: Forces acting around the bit

2.9.1.1 Pendulum Assembly

This kind of BHA assembly could be a single stabilizer or more stabilizers with the first stabilizer placed at some distance from the bit. A standard drill collar without any stabilizer behaves simply like a pendulum assembly. Effect of the pendulum force depends on the

size/diameter of the collar, as seen in the *Figure 2.22***.** Pendulum assembly tends to give a drop profile, as the angle of deviation tends to decrease and produce a vertical hole. As seen in the figure, the higher the distance "L" from the bit, the lower the length of the unsupported drill collar, and the higher the tendency of the collar to sag or make contact with the lower wall side of the hole, and thus the lower the pendulum force. [40]

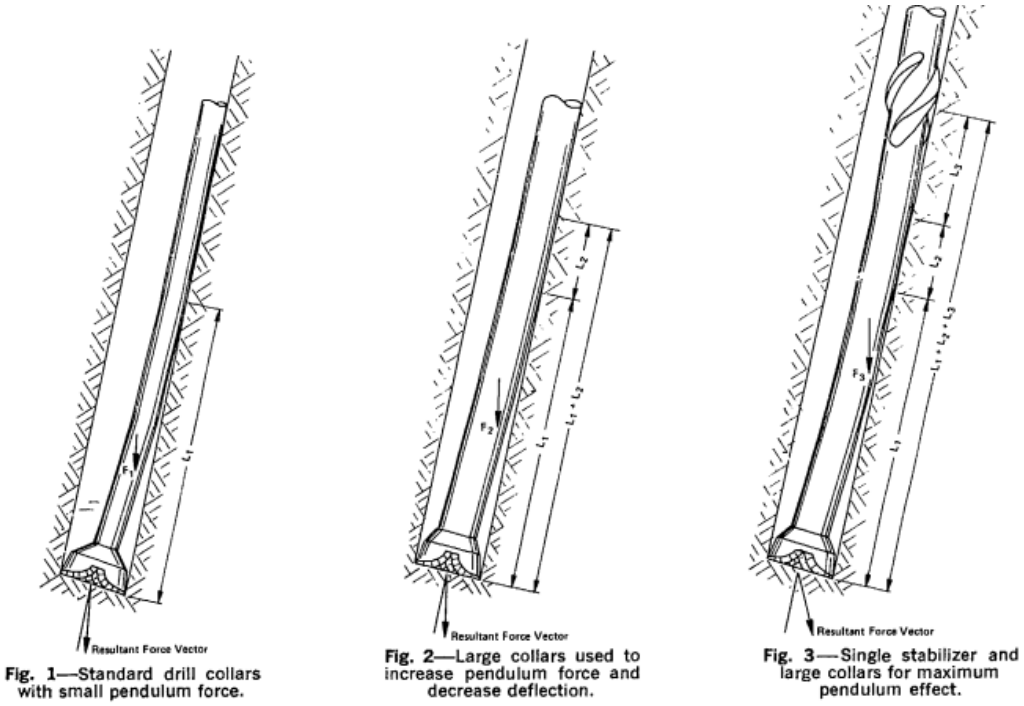

Figure 2.22: Types of pendulum assemblies we could have [40]

For a pendulum assembly or rather a drop assembly, the bit side force acts towards the low side, i.e. we tend to have a negative side force value. This can be observed in the study carried out by Tuotain, [43] where variations in the side forces are observed at different hole inclinations with one stabilizer placed some distances from the bit. (ref: *Figure 2.23*) [43]

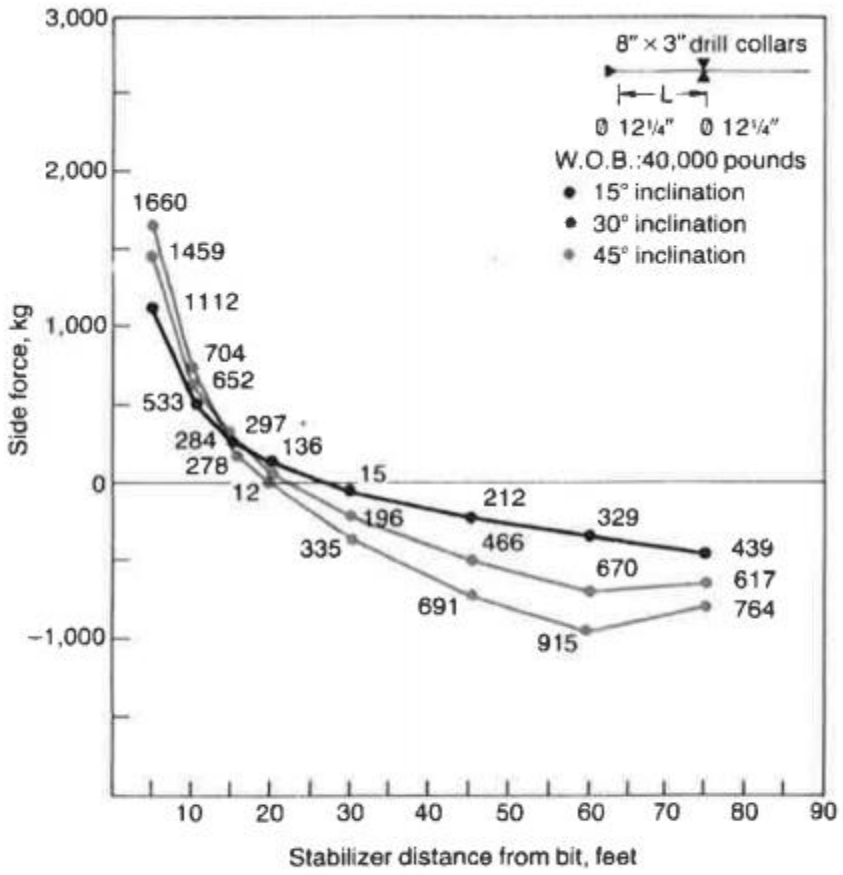

Fig. 3—Variations in side-force at different hole inclinations for a pendulum assembly with one stabilizer located at a range of distances from the bit.

Figure 2.23: Variations in side-force at different hole inclinations for a pendulum assembly [43]

The distance "L" from the bit up to point of contact with the wall determines the bit side force also referred to as the pendulum force. The bit side force acts towards the low side of the hole in a drop profile. At 45^0 inclination, the side force is maximum with value of - 915 kg at L=60 feet. With 30^0 inclination, maximum SF= - 670 kg at L=60 feet, while with 15^0 inclination, maximum side force is not reached and even located beyond 75 feet. [43]

2.9.1.2 Near-bit Assembly

This involves the use of at least two stabilizers, with one positioned as close as possible to the bit, giving a build profile. The assembly minimizes the lateral bit force and also the lateral bit movement. The distance between the near bit and the second bit is used to adjust the side force.

Build profile tends to increase when there is increase in the distance, making the side force to act towards the high side of the hole (i.e. positive side force value). Maximum build rate is reached when increase in the distance between the stabilizers causes the drill collar to bend and make tangent with the low side of the hole. This bending also depends on the following:

- Hole size
- Collar size
- Inclination
- Stabilizer gauge
- Weight on bit (WOB)
- Rotary speed (RPM)

The build rate increases as hole inclination increases, because the weight of the drill collar causes the bend. Bending of the drill collars behind the near bit stabilizer is high as the WOB increases, thus increasing the build rate. Higher RPM reduces the build rate, as it is likely to straighten out the drill collars – low RPMs like 70 – 100 rev/min are usually used for near bit assemblies. [44]

2.9.1.3 Packed Hole Assembly

This type of assembly is basically used to maintain the direction we are drilling, to hold the profile. It usually contains three to five stabilizers which are properly spaced in order to maintain the angle. Also referred to as a stiff assembly. What prevents the drillstring from bending is the increased stiffness on the BHA due to the added stabilizers. The purpose of the assembly is also to minimize rate of change in deviation, although slight build or drop tendency is allowed to respond to formation changes. [44]

2.10 Bruce Walker Model

This is a model that describes the deflection of drill string/collar with respects to stabilizer position acting like a point load on the collar, applying Rayleigh-Ritz method. (See *Figure 2.24*) The following assumptions are considered. [40]

1. A rigid borehole wall
2. A rigid cantilever of length, *L (m)* and uniform weight per unit length, *w*.

3. Centrally located bit with no moment with the formation
4. No moment between tubular and supports both at the top and at the bottom
5. Bit can freely rotate about the origin in the vertical plane.
6. Effect of rotation and vibration is negligible
7. Constant weight on bit, $P_o\,(N)$ represented as an applied axial load
8. Drill collars behave as elastic bodies, with Young's modulus of elasticity, E
9. The bit side force is $F_0\,(N)$

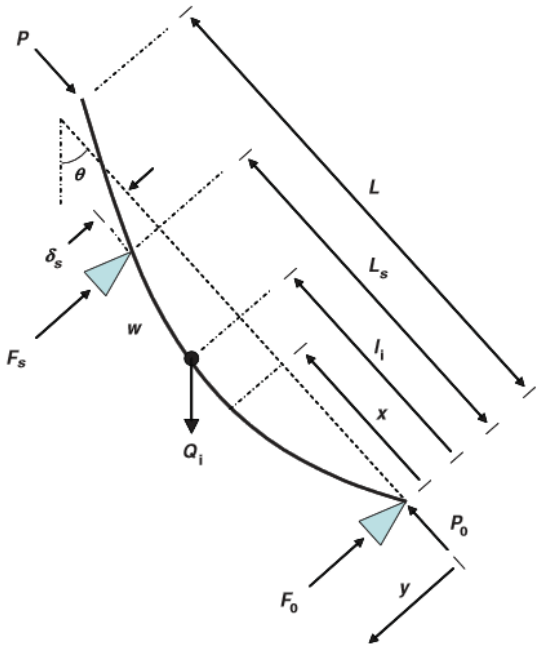

Figure 2.24: A coordinate system for a drill pipe composed of an inclined, uniform column with an axial load and an arbitrary number of intermediate point loads. [45]

2.10.1 Series Representation of Displacement Function

A function *y(x)* to describe the state of the BHA (i.e. the deflected shape inclined at an angle), can be represented by a Fourier series [40] [42]

$$y(x) = \sum_{n=0}^{\infty} A_n \sin \alpha_n x + \sum_{n=0}^{\infty} B_n \cos \alpha_n x$$

…….2.61

Where A_n, B_n and α_n are to be determined by boundary conditions and by using the principle of minimum potential energy described by Rayleigh-Ritz. (Ref: *Appendix E*)

Satisfying the boundary conditions of no moments between the tubular and supports, both at the top and the bottom.

i.e. $-EI\frac{d^2y}{dx^2} = 0, when\ x = 0\ and\ when\ x = L$

$$y(x) = \sum_{n=0}^{\infty} A_n sin\left[\frac{(2n+1)\pi x}{2L}\right]$$

……2.62

Figure 2.25 shows the maximum deflection obtained with an axial load of 2.65 kg using equation 2.62 which uses the values of A_n obtained from the solution to equation E-25 (ref: *Appendix E*). A C++ program developed by IRIS (with the implementation code in *Appendix F-3*) was used to implement this model. WOB equal to or higher than 2.65 kg at zero degree inclination could cause buckling of the pipe.

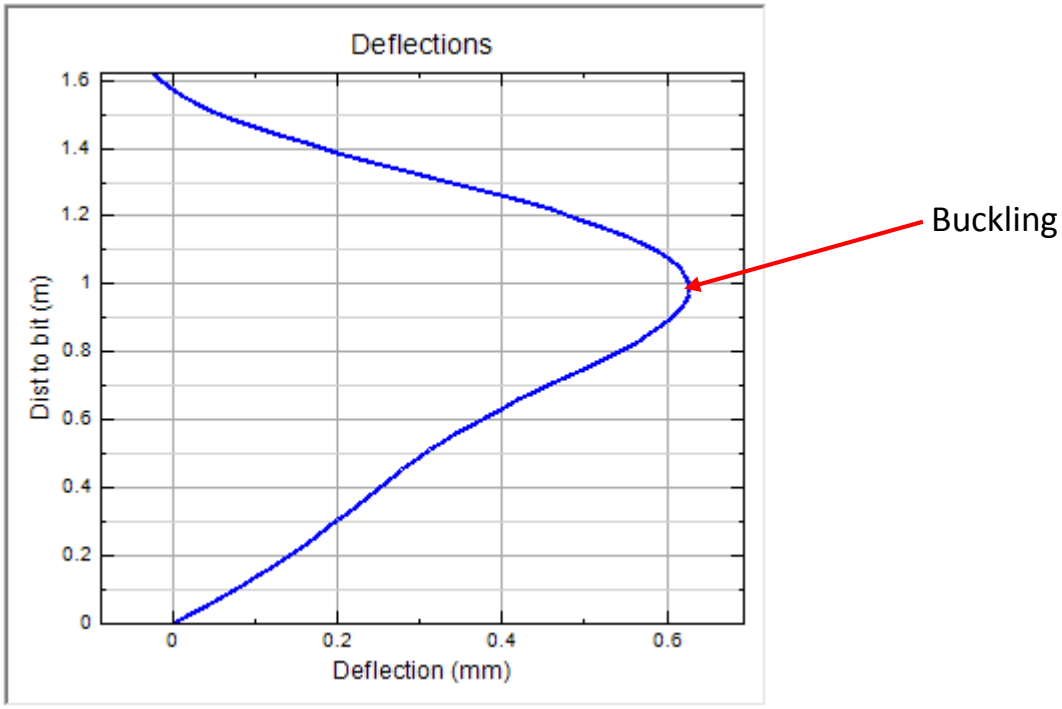

Figure 2.25: Buckling limit using Walker's minimum potential energy model, showing the maximum deflection of 0.63 mm at WOB of 2.65kg.

3 DRILLBOTICS DESIGN AND CONSTRUCTION

This section describes the implementation of the theories highlighted in previous section. It shows the basis of the Drillbotics setup and different factors considered during the construction; all with the objective to have a working setup.

3.1 Drillbotics Design Calculation

A PDC micro bit of 1.125 in (28.6 mm) diameter with brazed cutters and two nozzles was being specified in the rules and guidelines for Drillbotics 2016. The cutter back rake was 20 degree and cutter diameter was 0.529 in (13.44 mm). Each nozzle size was 2.35 mm in diameter, placed approximately at 180 degrees apart.

The drill pipe for the experiment was 100 cm long and was constructed from a round aluminum tube, the outer diameter being 10 mm with a wall thickness of 1.0 mm, thereby deriving an ID of 8 mm. The modulus of elasticity of the drill pipe is 68.9 GPa, while the shear modulus of elasticity is 24 GPa. The area moment of inertia I, was given by,

$$I = \frac{\pi}{64}(OD^4 - ID^4) \qquad \text{……..3.1}$$

$$I = \frac{\pi}{64}(0.01^4 - 0.008^4) = 2.898 * 10^{-10}\ m^4$$

While the polar moment of inertia J_z was,

$$J_z = \frac{\pi}{32}(OD^4 - ID^4) = 5.796 * 10^{-10}\ m^4$$

3.1.1 BHA Dimensioning

The BHA was limited to a length of 18-in (45.72 cm) as per the Drillbotics 2016 guidelines. As the hole size was 28.6 mm, the BHA needs to be scaled to accommodate sufficient clearance for cuttings evacuation out of the hole. The 2mm clearance on each side of the BHA was probably inadequate to allow cuttings to pass through. In order to allow better flow of cuttings a 3.5mm clearance would be more suitable. This would then maximize the BHA outer dimensions to 21 mm, consecutively allocating a thickness of 7mm to the BHA. The BHA's linear weight was approximately 2.24 kg/m. The linear weight was derived from the following equation. [47]

$$W\ \left[\frac{Ib}{ft}\right] = 10.68(OD - t_w)t_w$$

.....3.2

In equation 3.2, the outer diameter (OD) and wall thickness are in inches.

However in SI units, this can be expressed as,

$$W\ \left[\frac{kg}{m}\right] = 24657.254(OD - t_w)t_w$$

.....3.3

3.1.2 Determination of the Maximum Torque

The Drillbotics setup suggested that the pure aluminum pipe was the weakest point, with an ultimate tensile strength (UTS) of 110 MPa. The ultimate shear strength (USS) calculation exclusive to aluminum is calculated as follows [48]:

USS = 0.65*UTS = 0.65*110 = 71.5 MPa

Therefore the maximum torque that the drill pipe can undertake prior to breaking is,

$$\mathrm{T}_{max} = \frac{USS}{r}\frac{\pi}{32}(OD^4 - ID^4)$$

.....3.4

$$\mathrm{T}_{max} = \frac{71.5 * 10^6}{0.005}\frac{\pi}{32}(0.01^4 - 0.008^4) = 8.30\ Nm$$

The tensile yield strength (TYS) for aluminum is 95 MPa [48] hence the shear yield strength (SYS) will be [48]:

SYS = 0.55*TYS = 0.55*95 = 52.25 MPa

Therefore, the aluminum drill pipe should not be torqued higher than the yield torque. The yield torque is defined as,

$$\mathrm{T}_{yield} = \frac{SYS}{r}\frac{\pi}{32}(OD^4 - ID^4)$$

.....3.5

$$\mathrm{T}_{max} = \frac{52.25 * 10^6}{0.005}\frac{\pi}{32}(0.01^4 - 0.008^4) = 6.06\ Nm$$

This implies that the top drive should have a maximum operating torque limit of 6.06 Nm and should never exceed 8.30 Nm to prevent drill pipe breakage.

The Omron stepper motor (Model: Nema 23, 700W) and its associated drive system was used to drive the drill pipe. This stepper motor could deliver a constant torque of 2.4 Nm and peaked at 7 Nm.

Internal documentation within IRIS determined that should an instantaneous stoppage occur at the drill bit while rotating the drill-string (thereby replicating stick-slip conditions), it would take a short time before the controller of the top-drive motor would stop rotating. During this time interval, the drill-pipe would twist-off and the additional torque might damage the drill-string. The time required to stop this drill pipe rotation is dependent on the signal relay time (loop duration) between the PLC (Programmable Logic Controller) and top-drive motor (Model: Nema 23).

The torque induced on the drill-string due to twisting, considering a shear modulus, G of 24 GPa for aluminum is,

$$\mathrm{T}_{twist} = \frac{J_z}{l} G\theta \qquad \text{……...3.6}$$

where J_z is the polar moment of inertia, θ is the twisting angle and l is the length of the drill-pipe.

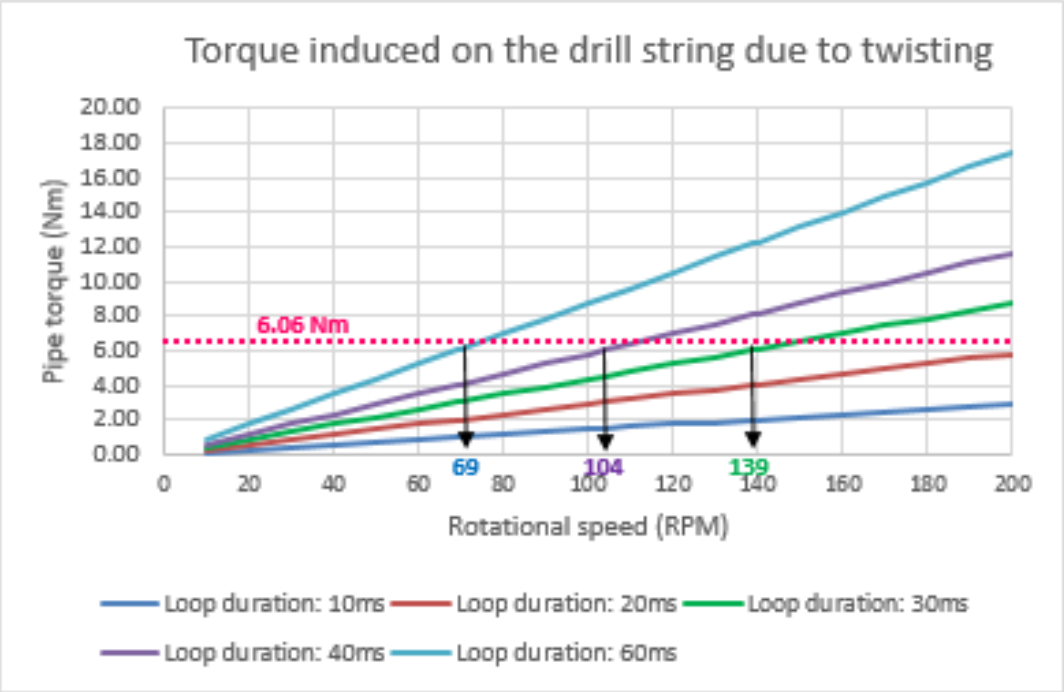

Figure 3.1: Twist torque as a function of initial rpm for different loop durations

Figure 3.1 illustrates the resulting drill pipe twisting torque, T_{twist} as a function of the initial rotational speed for different PLC control loop durations. Using the maximum yield torque limit of 6.06 Nm, the following signal relay times correspond to the drill-pipe rotations are tabulated below:

Maximum Operating Torque Limit of the drillpipe (Nm)	Drill-pipe rotational speed (rpm)	Reaction time for relaying signal (ms)
6.06	69	60
6.06	104	40
6.06	139	30

Table 3.1: Response times of motor at corresponding RPM to avoid twisting of drill pipe

From the above, we can see that as the drill-pipe rotational speed increases, a quicker reaction time is required in order to prevent the drill pipe from reaching its maximum torque limitation.

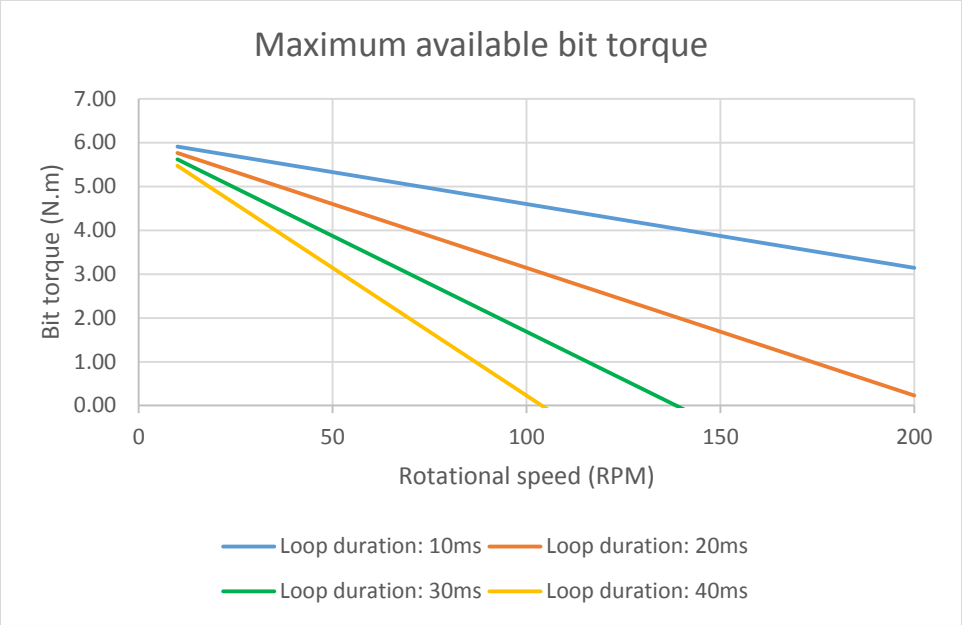

Figure 3.2: Maximum available bit torque as a function of the rpm different loop duration

From *Figure 3.2*, we can see that a bit with higher bit torque (bit wear) will take a shorter time interval to reach the maximum yield torque limit, 6.06 Nm of the drill pipe.

These findings relate to the formulation below that the maximum drill pipe yield limitation is a function of the torque generated by the drill pipe twist and torque at bit. (*IRIS internal document*)

$$T_{yield} = T_{pipe\ twist} + T_{bit}$$

Therefore, ……3.7 (a)

$$T_{bit} = T_{yield} - T_{pipe\ twist}$$

……3.7 (b)

3.1.3 Determination of the Maximum WOB

The maximum WOB we can apply is obtained from the relation proposed by Pessier & Fear, as described in *Section 2.4.1*, which relates WOB directly to the available bit torque, (*i.e. Equation 2.12)* For simplicity in SI unit, we use *Equation 3.8*. The bit torque used here is gotten from the values obtained from previous *Section 3.1.2*. WOB is in *kg*, T_{bit} is in Nm, d_{bit} is in m and g acceleration due to gravity, 9.81 m/s^2

$$WOB = \frac{3.T_{bit}}{\mu.d_{bit}.g}$$

……...3.8

Drillbotics competition indicates a minimum UCS of 13 MPa which gives an estimated coefficient of friction of $\mu = 0.92$, and a maximum UCS of 35 MPa, corresponding to $\mu = 0.90$. These values have been obtained using *Equation 2.13*.

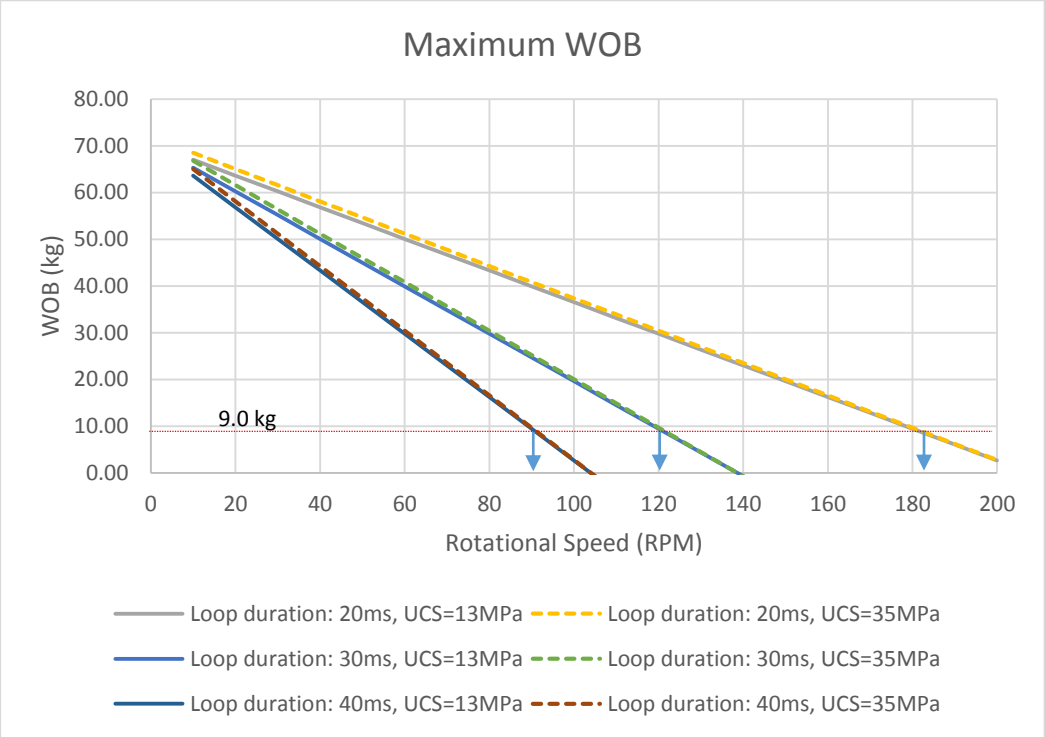

Figure 3.3: Maximum WOB as a function of the rotational speed for three different control loop durations and two formation hardness

Maximum Allowable WOB by Drillbotics Rules (kg)	Drill-pipe rotational speed (rpm)	Reaction time for relaying signal (ms)
9.04	> 90	40
9.04	> 120	30
9.04	> 185	20

Table 3.2: Limits of RPM wrt maximum allowable WOB of 9.04 kg

It is clearly shown from *Figure 3.3* that the maximum WOB decreases as the rotational speed increases. Since Drillbotics 2016 guidelines limited the maximum allowable WOB to 9.04kg, we will thus concentrate on WOB below this value. *Table 3.2* indicates with different reaction times,

the limits of RPM below which we will exceed the stipulated maximum allowable WOB of 9.04 kg.

3.1.4 Estimation of maximum ROP

The mechanical specific energy (MSE) as described in *Section 2.4.1* is a function of rotation speed, WOB, bit size and ROP. As MSE is directly related to the formation strength, we then anticipate possible penetration rates for different formation strengths using the limits of bit torque and WOB described previously in *Sections 3.1.2 and 3.1.3*. For simplicity again, we work in SI unit.

$$MSE = \frac{UCS}{0.35} = \frac{4WOB}{\pi {d_{bit}}^2} + \frac{4\mathrm{T}_{bit}.\dot{\omega}_{bit}}{\pi ROP\ {d_{bit}}^2} \quad \ldots\ldots\ldots\ldots\ldots\ldots 3.9$$

$\dot{\omega}_{bit}$ is the bit angular velocity, referred to as the RPM.

Substituting *Equation 3.7* and then solving for ROP, we get

$$ROP = \frac{1}{\pi {d_{bit}}^2}\left(\frac{4T_{bit}RPM}{\frac{UCS}{0.35} - \frac{4WOB}{\pi {d_{bit}}^2}}\right) \quad \ldots\ldots\ldots\ldots\ldots\ldots 3.10$$

Figures 3.4 and 3.5 thus show the estimated maximum ROP we expect with the two formation strengths of 13 MPa and 35 MPa as a function of the rotational speed for different loop durations.

It is seen from these two *Figures (3.4 and 3.5)* that the rate of penetration will drastically drop when transitioning from a soft to a hard formation.

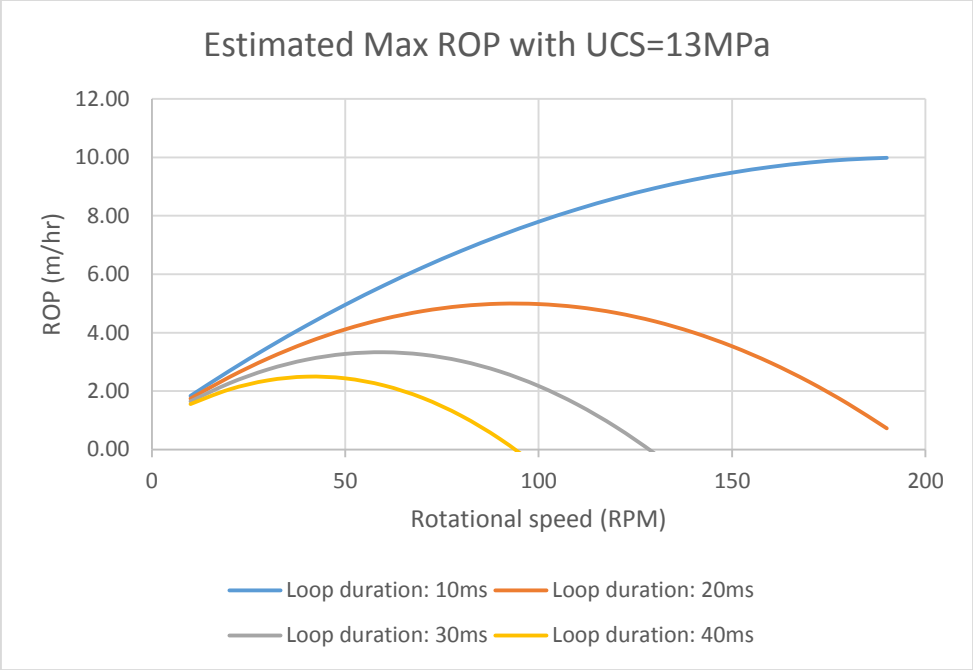

Figure 3.4: Estimated max ROP as a function of rotational speed for a formation strength of 13 MPa

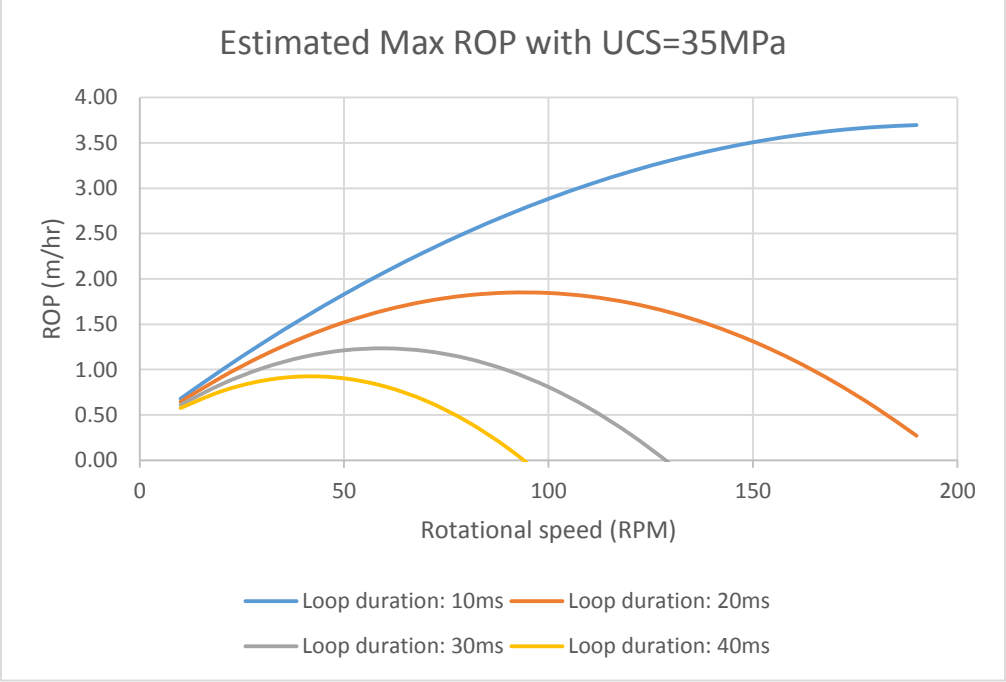

Figure 3.5: Estimated max ROP as a function of rotational speed for a formation strength of 35 MPa

3.1.5 Hydraulics design

The total pressure drop expected in the system is expressed in the following equation

$$\Delta P_T = P_{hyd} + \Delta P_{hose} + \Delta P_{swivel} + \Delta P_{pipe} + \Delta P_{BHA} + \Delta P_{bit} + \Delta P_{annulus}$$

……..3.11

As stated earlier, water is being considered as the drilling fluid for this work with constant viscosity of *1.002e-3 Pa.s*, and density of *998.2 kg/m*^{3} at room temperature of 20 ^{0}C and atmospheric pressure.

Based on the assumption of Sifferman and Berker mentioned in section 2.8 for a minimum flow velocity to ensure cutting transport in the annulus with water as drilling fluid, a flow velocity greater than or equal to *0.5 m/s* is being used.

Also, with the use of the settling model described in *Section 2.8*, a settling velocity of *0.5 m/s* was obtained with particle size of 5000 micron, and density of *2750 kg/m*^{3}. (Ref: *Figure 3.6*)

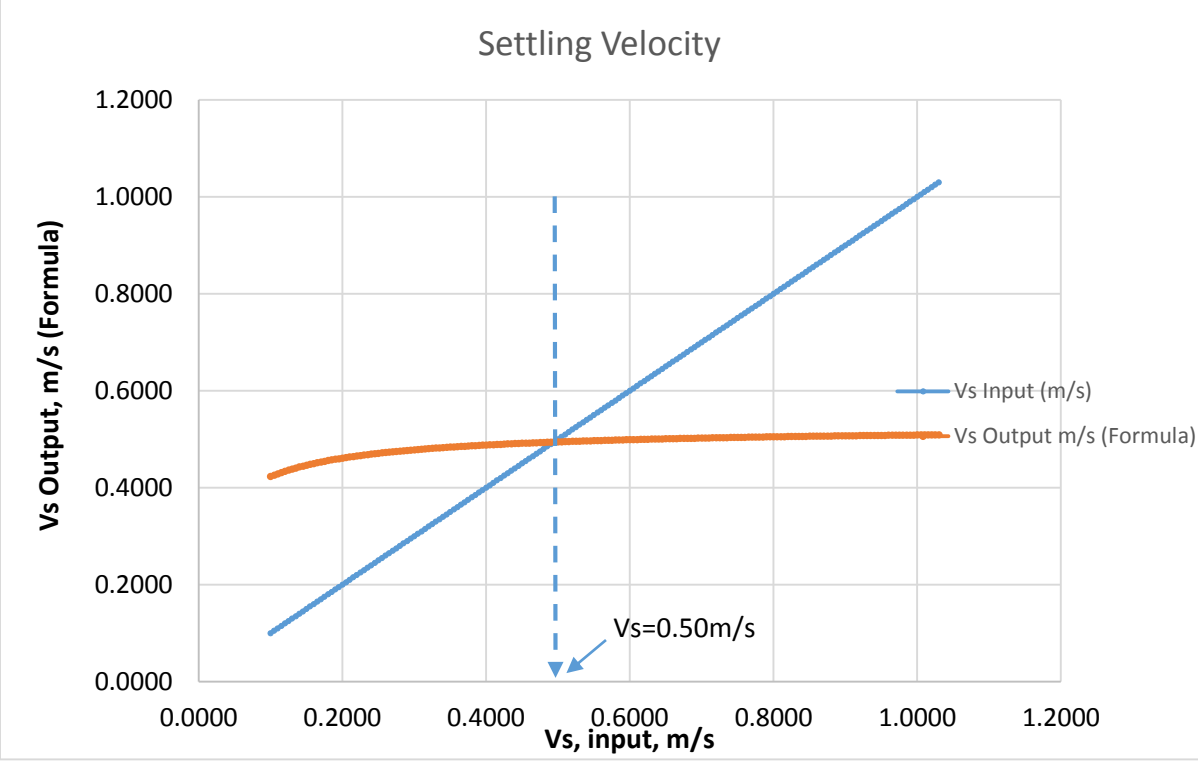

Figure 3.6: settling velocity solving by iteration of Equations 2.58, 2.59 and 2.60, as the equations are implicit functions of particle Reynolds number

This gives the minimum flow rate expected in the annulus as:

$$Q = 0.5 * \frac{\pi}{4}(0.0286^2 - 0.0216^2)\frac{m^3}{s}$$

$$Q = 1.3801 * 10^{-4}\, m^3/s = 8.28\, l/min$$

It is expected that the minimum flow rate to be delivered by the pump is ***8.28 l/min*** or higher. Note that OD of BHA has been used because the rock sample to drill is of height 30 cm, which is lower than the length of the BHA.

1. P_{hyd}, which is the hydrostatic at the pump level is dependent on the height of the rig.
   The pump is positioned on the table at the height of about ***1.0 m***. Therefore, height of the rig is estimated to be 1.0 m from the pump.
   So that $P_{hyd} = 0.0981 * 0.9982 * 1 = 0.098\, bar$

2. Pressure drop across the hose connecting the pump to the swivel of the top drive is being done assuming length of hose to be ***1.5 m***, with ID of 0.5-in (12.7 mm) and made of plastic (roughness 0.03 mm). The flow velocity inside the hose is flowrate divided by the flow area. The flow is turbulent as indicated from the Reynold's number calculated below:

$$Re = \frac{\rho u D}{\mu} = \frac{4\rho Q}{\mu.\pi D} = \frac{4 \times 998.2 \times 8.28}{\pi 1.002 * 10^{-3} \times 0.0127 \times 60000} = 13780.9$$

   Using equation 2.39, the friction factor is

$$f_D = \left[-1.8 \log\left(\frac{6.9}{Re} + \left(\frac{\varepsilon/D}{3.7}\right)^{1.11}\right)\right]^{-2}$$

$$f_D = \left[-1.8 \log\left(\frac{6.9}{13780.9} + \left(\frac{0.03/12.7}{3.7}\right)^{1.11}\right)\right]^{-2} = 0.032$$

   Thus the pressure drop is:

$$\Delta P_{hose} = \frac{8\rho Q^2 f_D L}{\pi^2 D^5}$$

$$\Delta P_{hose} = \frac{8 \times 998.2 \times (1.308 * 10^{-4})^2 \times 0.032 \times 1.5}{\pi^2 0.0127^5}$$

$$\Delta P_{hose} = 2238.8\ Pa = 0.022\ bar$$

3. For the top-drive swivel (rotary union), with flow rate of 8.28 *l/min* and $C_v = 5.25$, pressure drop is

$$\Delta P_{swivel} = \left(\frac{Q}{C_v}\right)^2 = 0.06894 \left(\frac{8.28 \times 0.264}{5.25}\right)^2 = 0.012\ bar$$

4. In the aluminum drill pipe with length 1.29 m (i.e. drill pipe + slip ring pipe), ID of 8.0 mm and a roughness of 0.03, with a flow rate of 8.28 l/min, we have a turbulent flow as indicated below

$$Re = \frac{\rho u D}{\mu} = \frac{4\rho Q}{\mu . \pi D} = \frac{4 \times 998.2 \times 8.28}{\pi 1.002 * 10^{-3} \times 0.008 \times 60000} = 21877.3$$

$$f_D = \left[-1.8 \log\left(\frac{6.9}{21877.3} + \left(\frac{0.03/8}{3.7}\right)^{1.11}\right)\right]^{-2} = 0.032$$

And thus the pressure loss is

$$\Delta P_{pipe} = \frac{8 \times 998.2 \times (1.308 * 10^{-4})^2 \times 0.032 \times 1.29}{\pi^2 0.008^5}$$

$$\Delta P_{pipe} = 19448.3\ Pa = 0.194\ bar$$

5. The pressure drop inside the BHA is defined by its length (0.42 m), ID of 6 mm and surface roughness for steel as 0.15 mm.

$$Re = \frac{\rho u D}{\mu} = \frac{4\rho Q}{\mu.\pi D} = \frac{4 \times 998.2 \times 8.28}{\pi 1.002 * 10^{-3} \times 0.006 \times 60000} = 29169.7$$

$$f_D = \left[-1.8 \log\left(\frac{6.9}{29169.7} + \left(\frac{0.15/6.0}{3.7}\right)^{1.11}\right)\right]^{-2} = 0.054$$

And thus the pressure loss is

$$\Delta P_{BHA} = \frac{8 \times 998.2 \times (1.308 * 10^{-4})^2 \times 0.054 \times 0.42}{\pi^2 0.006^5}$$

$$\Delta P_{BHA} = 45206.7\ Pa = 0.45\ bar$$

6. Pressure loss through the two bit nozzles of diameter 2.35 mm each is obtained using *Equation 2.49.*

   Equivalent nozzle diameter,

$$d_{en} = \sqrt{2.35^2 + 2.35^2} = 3.32\ mm$$

$$\Delta P_{bit} = \frac{\rho Q^2}{2(A)^2 0.95^2} = \frac{998.2 \times (1.308 * 10^{-4})^2}{2 \times \left(\pi \times \frac{0.00332^2}{4}\right)^2 \times 0.95^2}$$

$$\Delta P_{bit} = 139918.4\ Pa = 1.39\ bar$$

7. The pressure drop through the annulus will probably be small as it is shorter than 40 cm. So if we assume cuttings of density 2750 kg/m^3 with concentration of 20% and depth of 20cm.
   Effective diameter $D_e = 0.0286 - 0.0216 = 0.007\ m$
   Mixture density using eq. 2.53, $\rho_m = 998.2 * 0.8 + 2750 * 0.2 = 1348 kg/m^3$
   Mixture viscosity using eq. 2.54, $\mu_m = 0.001002(1 + 2.5 * 0.2 + 10.05 * 0.2^2 = 0.0019$

$$Re = \frac{\rho_m u D_e}{\mu_m} = \frac{4\rho_m Q}{\mu_m.\pi D_e} = \frac{4 \times 13482 \times 8.28}{\pi \times 0.0019 \times 0.007 \times 60000} = 17759.3$$

$$f_D = \left[-1.8 \log\left(\frac{6.9}{17759.3} + \left(\frac{0.15/6.0}{3.7}\right)^{1.11}\right)\right]^{-2} = 0.052$$

$$\Delta P_{ann} = \frac{8 \times 1348 \times (1.308 * 10^{-4})^2 \times 0.052 \times 0.20}{\pi^2 0.007^5}$$

$$\Delta P_{ann} = 9544\ Pa = 0.095\ bar$$

Thus the expected pump pressure while pumping at 8.28 l/min will approximately be 0.098 + 0.022 + 0.012 + 0.194 + 0.45 + 1.39 + 0.095 = 2.26 bar

This implies that the pump should be able to provide pressure head of at least 2.26 bar.

Figure 3.7 shows the variation of pressure drop in the system with respect to flow rate. At a minimum from rate of 8.28 lpm, a pressure drop of about 2.26 bara is observed.

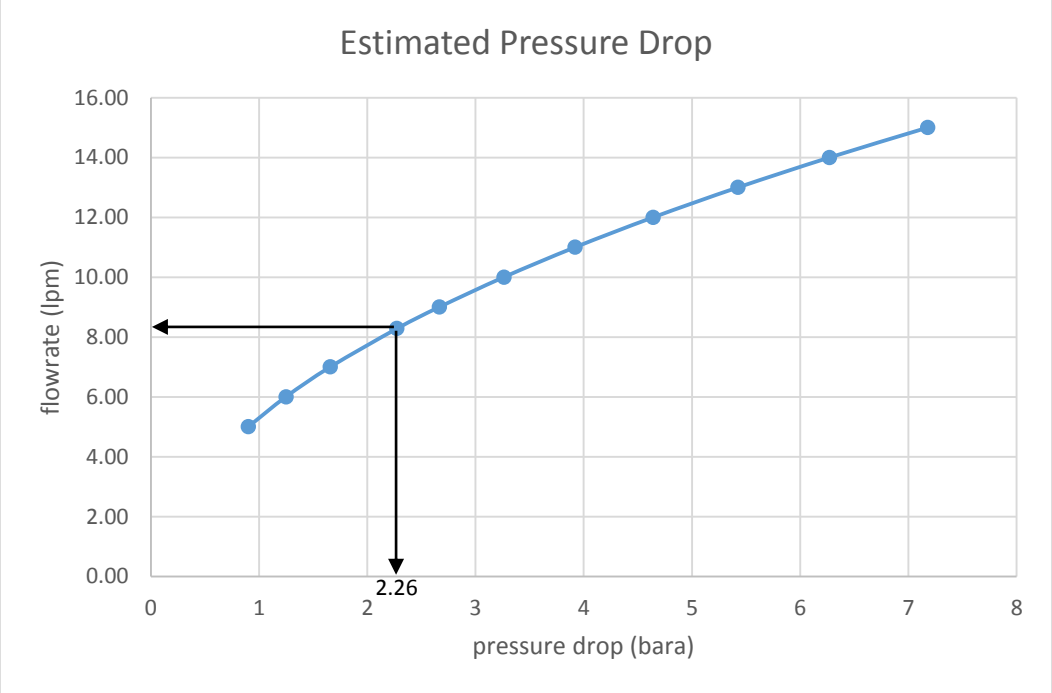

Figure 3.7: A plot showing the variation of pressure drops with flow rate. Shows the pressure drop at flowrate of 8.28 l/min

3.1.6 Deformation/Deflection of Drill Pipe

Figure 3.8 illustrates a fixed and pinned supported type of beam column loaded axially. Using Euler criteria, the buckling critical force for the aluminum drill pipe is calculated by;

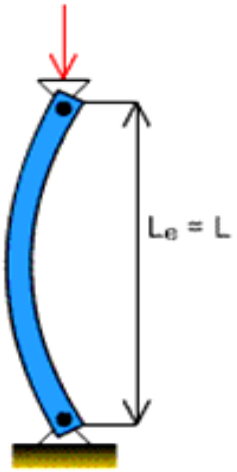

Figure 3.8.: One fixed and one pinned type support

$$P_c = SF\frac{\pi^2 EI}{(kL)^2} \qquad \text{.....3.12}$$

Where k is the buckling effective length factor, which varies from 0.7, in the case of a pinned-pinned configuration, to 2.0 where one end of the beam can sway. [49] Applying safety factor SF of 87.5%

Therefore for k = 0.7,

$$P_c = 0.875\frac{\pi^2 68.9 * 10^9 \times 2.898 * 10^{-10}}{(0.7 \times 1.0)^2} = 352\ N$$

while for k = 2.0

$$P_c = 0.875\frac{\pi^2 68.9 * 10^9 \times 2.89 * 10^{-10}}{(2.0 \times 1.0)^2} = 43\ N$$

In the case of DrillBotics, the top end of the drill pipe is pinned in the top-drive shaft and is also pined to the top of the BHA. However, it is possible that the top of the BHA may move laterally especially at the start of the drilling as the bit will not have penetrated deeply into the rock. This implies our critical buckling force is 43 N. The drill pipe will thus be in compression, therefore the need to study the deflection of the string. Walker's model described in *Section 2.10* is used to analyze the deflection of the pipe. From the model, a WOB of 2.65kg accounted for a maximum

deflection of 0.63 mm. (Ref: *Figure 2.25*). This implied that we had to limit our WOB to 2.64 kg to avoid excessive deformation of the pipe.

3.2 Construction

The schematic of the frame to support the hoisting system and transmission system of the robot is shown in *Figure 3.9*. The building of the frame is split into three parts. The middle part being fixed to the supporting table, while the upper part moves upward and downward, and supports the hoisting and the power transmission system, with the aid of a C-beam linear actuator. The lower part can also move upward or downward; it is raised to the appropriate height in order to rest on the formation sample. This also houses the X-Y linear actuator required to adjust and monitor the lateral displacement of the riser. The actuators have motors to control the movement.

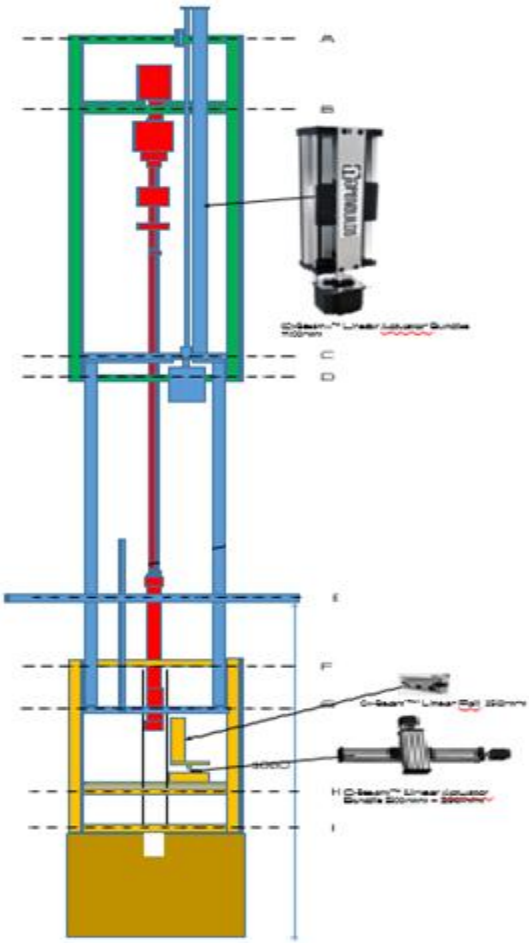

Figure 3.9: Schematic of the frame that supports the whole system

Figure 3.10: A complete structure of the Drillbotics laboratory setup

The frame was constructed using several tools purchased from the www.openbuild.org website.

The stacking of the string is shown in *Figure 3.11*, also showing the location of the accelerometers that is being used to monitor the inclination of the hole.

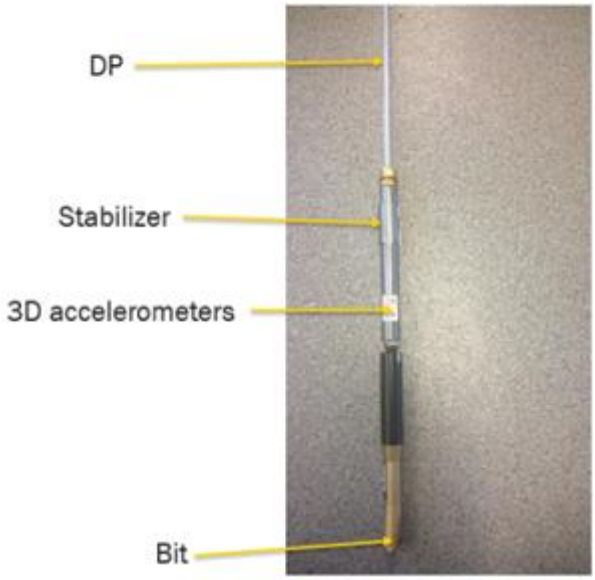

Figure 3.11: stacking of the string

3.2.1 Construction processes

Some of the processes carried out during the construction phase are,

1. Setting up the frame shown in the figure above, starting from the lower section upward
2. Stabilizing the table with hinges and cross bars as support
3. Mounting torque cell sensors (x2)
4. Mount load cell amplifiers for torque measurement (x2)
5. Mounting hook load cell sensors (x4)
6. Mounting load cell amplifiers for hook-load measurement (x4)
7. Gluing of electrical connection disk for slip ring
8. Gluing connector for lower shaft
9. Electrical wiring of slip ring rotating part
10. Electrical wiring of accelerometers
11. Fixing accelerometers on BHA
12. Applying silicon to isolate from water
13. Electrical connection of accelerometers to slip ring connecting disc
14. Electrical wiring of stator slip ring to the directional box.
15. Attaching the read sensor and anti-torque for stator slip ring

16. Electrical wiring of read sensor and connection to directional box
17. Mounting hoisting system.
18. Mounting the C-beam linear actuator plus the break on it.
19. Electrical wiring of the brake
20. Electrical wiring of hoisting motor
21. Attaching two proximity sensors for hoisting system
22. Mounting of X-Y linear actuator
23. Electrical wiring of X-Y linear actuator motors
24. Electrical wiring of directional box
25. Attaching two reed proximity sensors on X-Y actuator for monitoring directional box movement
26. Plumbing
27. Electrical wiring of pump
28. Mounting of emergency stop

3.2.2 Construction challenges

Some of the challenges encountered during the building include:

1. Stability because of the uneven floor level and stability of the table.
2. Designing of plates with holes as accurate as possible, to accommodate different components.
3. Availability of the correct dimensions of screws.
4. Need for the resizing of screw length and screw's head
5. Re-adjustment of the design to ensure accuracy

3.2.3 Riser Design

The directional controller steers two linear actuators in a X-Y configuration, i.e. perpendicular to each other, which are used to displace laterally a riser (ref: *Figure 3.12*).

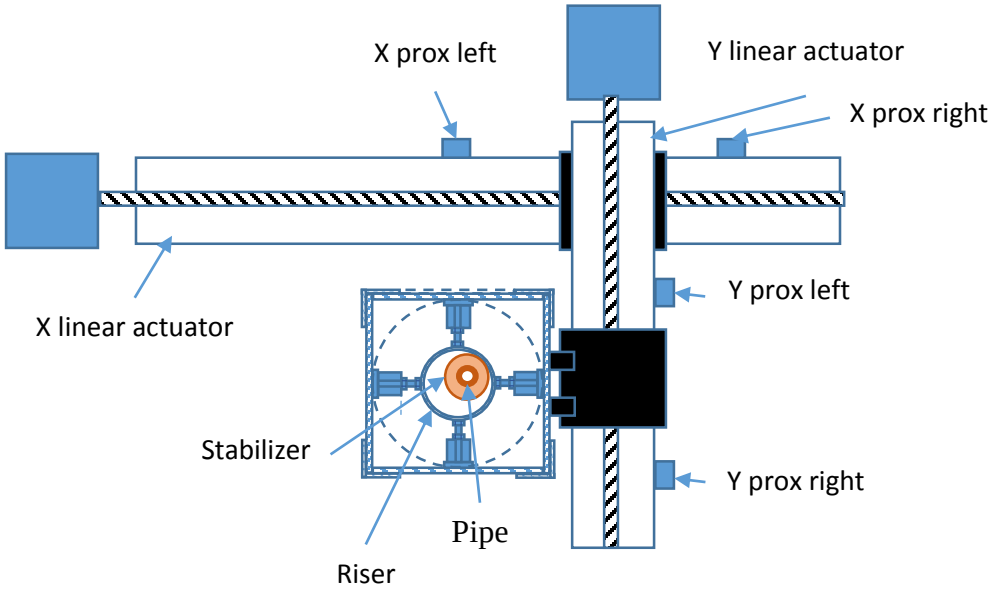

Figure 3.12: X-Y linear actuators and associated riser.

By the displacement of the riser, it is possible to exert a side force on a stabilizer at the top of the BHA and therefore actively control the drilling direction. By all practical means, this is the principle of a push the bit rotary steerable system, except that this is not the stabilizer that pushes on the borehole, but that the riser that pushes on the stabilizer.

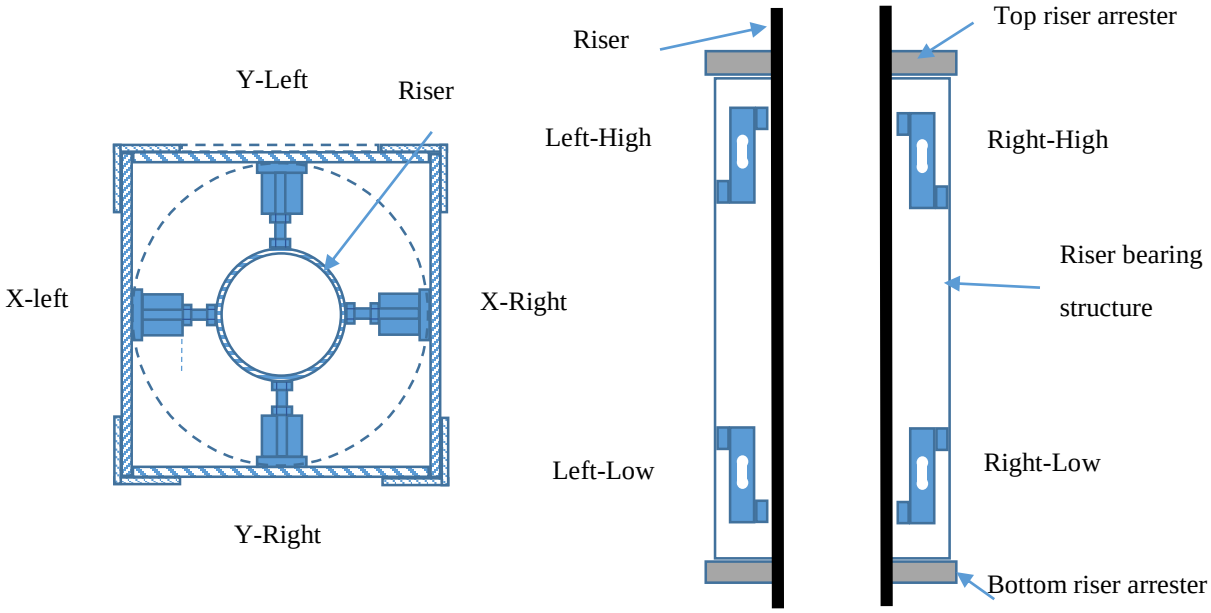

Figure 3.13: cross section of the box that holds and houses the riser

The riser is equipped with 8 load cells that read the current force applied on the stabilizer. These load cells are denoted as (ref: *Figure 3.13*):

- X-left-high
- X-left-low
- X-right-high
- X-right-low
- Y-left-high
- Y-left-low
- Y-right-high
- Y-right-low

Figure 3.14 shows the actual box that houses the riser, while *Figure 3.15* illustrates the placement of the drill string inside the riser, which is being attached to the linear X-Y actuator to control the lateral displacement of the riser.

Figure 3.14: Constructed Riser with the load cells

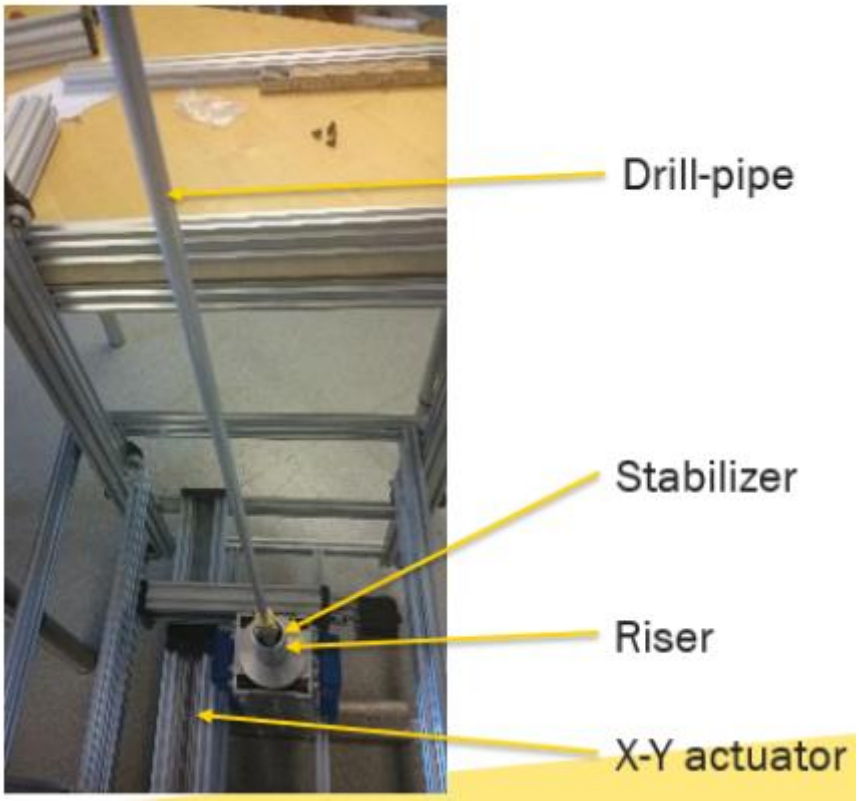

Figure 3.15: X-Y Actuator supporting the riser with the drill pipe and BHA inside

3.2.4 Load cell

Readings from the load cells are very small, usually in the range of 0-0.3 mV, thus the need for an amplifier to boost the readings to 3.3V. The amplifiers also convert the readings to a digital reading, which is eventually converted to mass and then weight in order to determine the amount of force applied. The amplifiers are actually calibrated in order to get an accurate force applied on the load cells (ref: *Figure 3.16*)

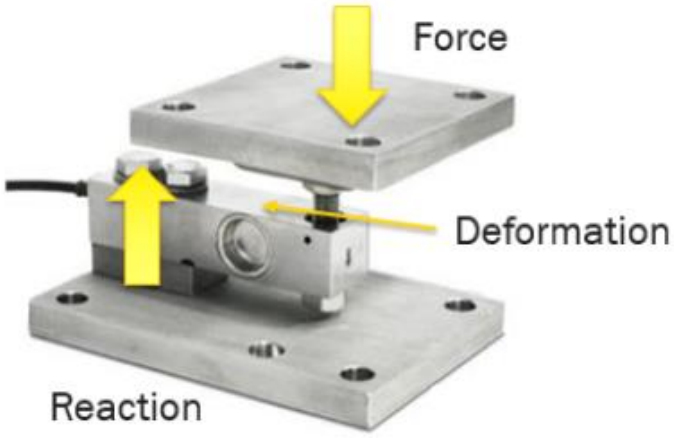

Figure 3.16: Working mechanism of the load cell

3.2.5 Measurement of Inclination

The BHA is equipped with 3D accelerometers placed at mid distance along the BHA on each side of the drill-collar (ref: *Figure 3.17*). These accelerometers are used to measure the inclination. The level of vibration can equally be measured as described in IRIS internal document summarized in *Appendix D.*

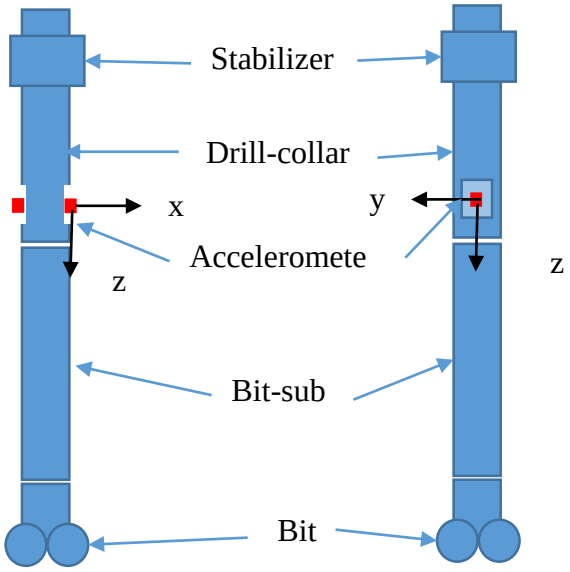

Figure 3.17: schematics of the position of 3-D accelerometer in the BHA. This is used to measure and monitor the inclination.

In order to obtain an orientation, i.e. a toolface, of the accelerometer while the drill-string rotates, there is a proximity sensor that detects each complete rotation. In addition, the drilling controller sends the current top-drive rotation angle at regular interval as a discrete value (say 10000 samples per revolution).

As also mentioned in *Appendix D*, the acceleration observed by the sensor has the following origins:

- Gravitational field of the earth
- Axial vibrations like that due to bit bouncing, which is purely translational.
- Rotation of the pipe around its axis. A combination of centrifugal and Euler accelerations, with no Coriolis acceleration.
- Lateral movement of the pipe in the over-gauge hole. A combination of translational and all the rotational accelerations.

Over a period of rotation, the average of estimations of signals from the axes of the accelerometer gives a more accurate assessment of the inclination.

However, if there are axial and/or lateral vibrations, then the accelerometer signals will contain much more noise, and applying a FFT and a pass band filter around the nominal rotational frequency, it is possible to eliminate the lateral acceleration effects.

On the other hand, by measuring the amplitude of the "noise", i.e. eliminating the main rotational frequency, it is possible to estimate the vibration level. If the vibration level goes above a defined threshold, then we can stop the rotation in order to avoid any potential destruction of the drill-string.

3.3 Control Algorithm for the circulation system

The following is the description of the control algorithm for the circulation system, also described in *Figure 3.18*.

- Auto-calibration:
    - At power up, the system auto-calibrate itself
    - Start pump
    - Record reference pressure
- Abnormal operation #1:
    - Pressure increasing abnormally (partial obstruction):
        - Pull up to top of block
        - If pressure improved go to drilling mode
        - Else (still obstruction): shutdown
- Abnormal operation #2:
    - Pressure very fast (total obstruction):
        - Stop pump
        - Stop rotation
        - Pull up to top of block
        - If no overpull, go to drilling mode
        - Else (still obstruction): shutdown
- Abnormal operation #3:
    - Pressure too low (leakage):
        - Stop rotation
        - Stop pump
        - Stop hoisting
        - Stop directional control
        - End!!

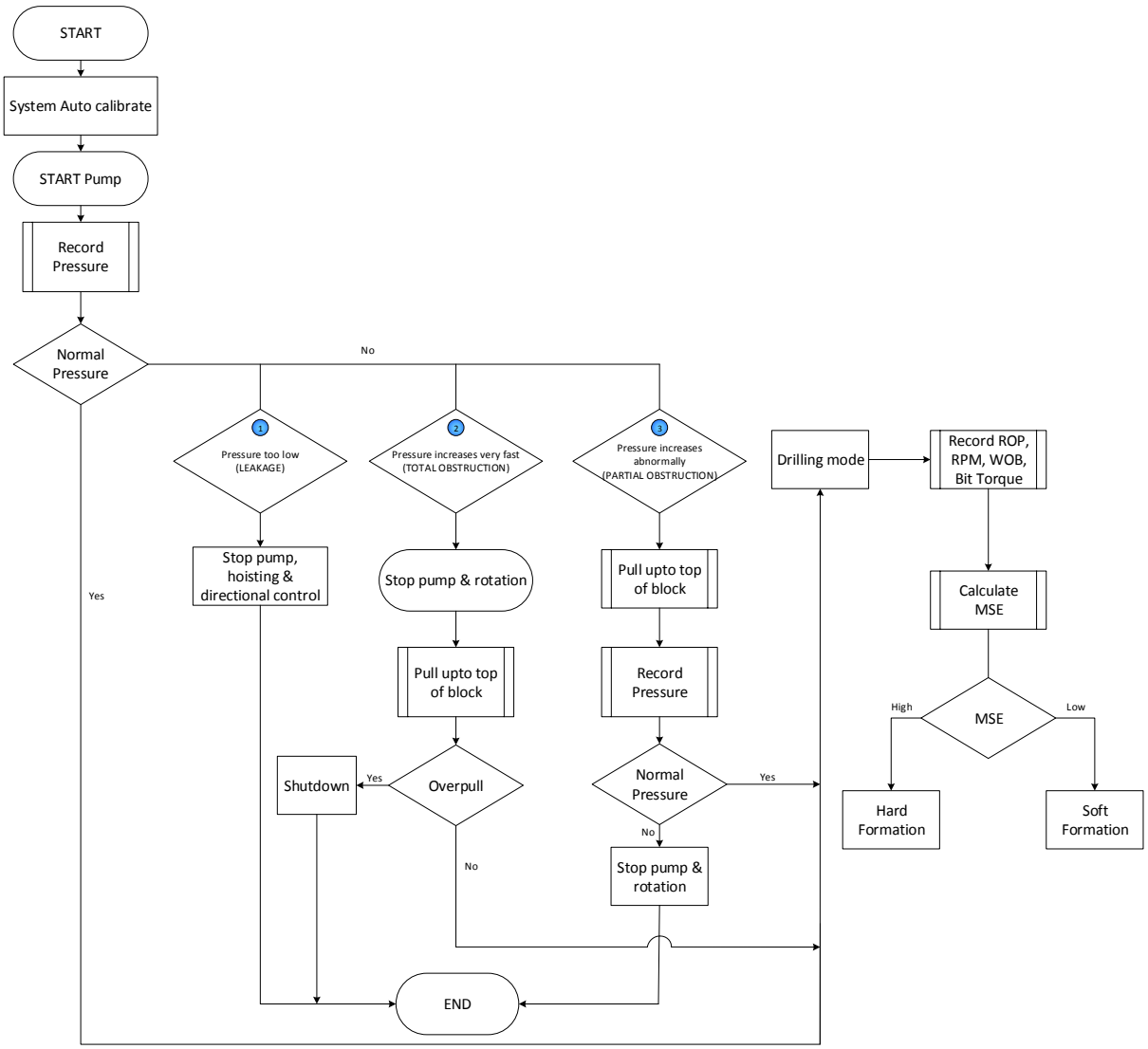

Figure 3.18: Control Algorithm for the Circulation System

4. DRILLBOTICS TEST RESULTS

This section presents the experimental testing and results of some of the components for Drillbotics. Presented below are the test results from the load cells used for hook load and torque measurements.

4.1 Testing of load cells

Testing has been performed for both hook load and torque measurements. The results attained have been listed under the following sections.

4.1.1 Hook load

The hook load is total load expected to be read by the load cells including the top drive weight plus all the components down to the bit. The plate supports the top drive and motor systems, hence, top drive weight (is the sum of plate weight + 2 Torque load cells + motor weight) = 7.77 kg

Slip ring = 0.94 kg

Drill string + fittings = 0.18 kg

BHA alone = 0.47 kg

BHA + Baker bit = 0.97 kg

Total expected weight = 9.86 kg

#	**Component**	**Weight (kg)**
1.	Top drive	7.77
2.	Slip ring	0.94
3.	Drill string + fittings	0.18
4.	BHA + Baker bit	0.97
	Total	**9.86**

Table 4.1: Weight of the top drive and string components

Hook load cells output readings calculations

The total weight of 9.86 kg is distributed among the four load cells. (Ref: *Figure 4.1*) Therefore, each load cell will read 2.465 kg (i.e. 9.86 ÷ 4)

Maximum output reading for the gain on each load cell = 3.3 V

With a safety margin of 20 %

Hence, output gain reading = 0.80 * 3.3 = 2.64 V

This implies that 2.465 kg is equivalent to output reading of 2.64 V

The relative calibrating weight of 1.68 kg for each load cell corresponded to an output reading of 1.80 V. This reading for each load cell was obtained by adjusting the calibrating pins on each of the amplifiers as indicated in the *Figure 4.2*. The gain readings obtained from each of the four load cells with respect to weight of 1.68 kg were 1.801 V, 1.802 V, 1.802 V and 1.802 V.

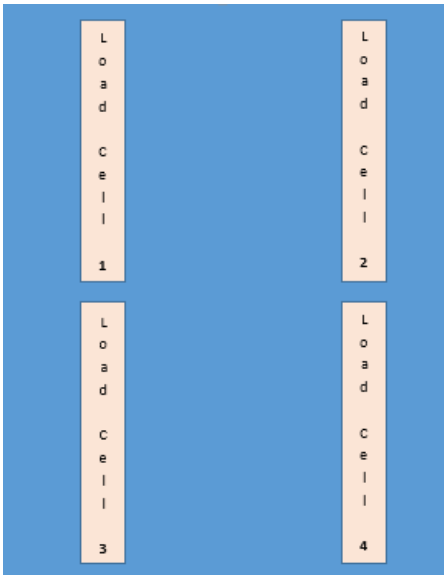

Figure 4.1: Schematic of load cells layout for hook load

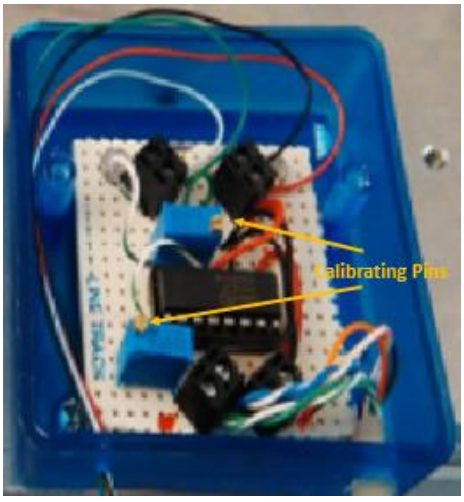

Figure 4.2: Amplifier to boost readings from load cells.

4.1.2 Torque from the torque load cells

Two torsional load cells were installed on the top drive (ref: *Figure 4.3*) in order to read and monitor the torque delivered from the Omron stepper motor being used to run the top drive.

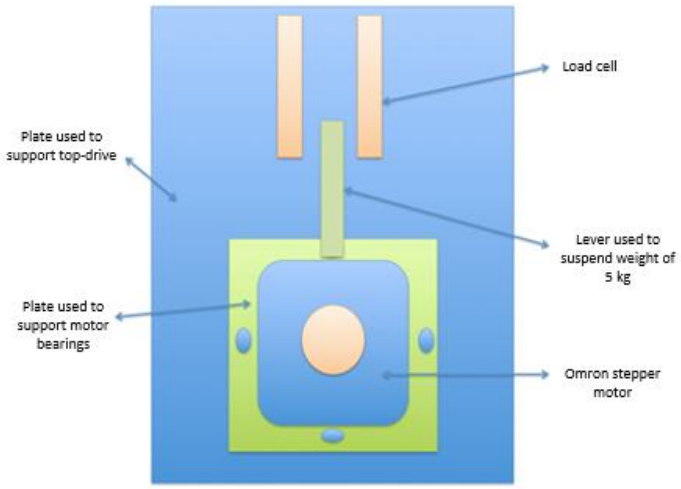

Figure 4.3: Schematic for the Torque measurement from load cells

A weight of 5 kg was utilized for calibrating the load cells for torsional measurements. This weight was attached to the lever (or rather tail) and suspended on either side of a cell at a time. This methodology was followed in order to generate a torque reading for the corresponding load of 5 kg from each of the torsional load cells. The laboratory setup has been illustrated in *Figure 4.4.*

Figure 4.4: Drillbotics laboratory setup to test torsional load cells

Torsional load cells output readings calculations

Maximum torque expected from the motor	= 7.0 Nm
Maximum readings from each load cell	= 3.3 V
Applying 20% safety factor,	
Hence output gain reading = 3.3*0.80	= 2.64 V
Distance of torsional load cell sensor to geometric center of motor	= 8.25 cm
Distance of torsional load cell sensor to weight 5 kg on level	= 3.25 cm
Hence, corresponding torsional readings for 5 kg at distance 3.25 cm	= 1.5941 Nm

If the maximum torque from the motor corresponds to 2.64 V

Then, $1.5941\ Nm \equiv 2.64 * \frac{1.5941}{7} = 0.601\ V$, which is the value the torsional load cells need to be calibrated with.

4.2 Pump testing

The pump illustrated in *Figure 4.5,* was tested in order to determine the pump characteristics and pump performance for the Flojet pump.

Figure 4.5: Flojet pump, showing the input and outflow connections and electrical cables for the pressure sensor

The tests were performed for the following two scenarios:

1. Firstly, the system's pressure was steadily build-up by adjusting the choke valve. The quantity of water being pumped within 20 sec was then recorded to calculate the flowrate for each pre-set pressure. For each pre-set pressure, four readings were obtained.
2. Secondly, pressure readings and flowrate values were recorded by systematically adding a series of components into the circulation system. This was done in order to record the pressure losses associated with each component that was added into the system and provide an overview of the total system pressure loss.

It was observed in *Figure 4.6* that upon adding each component into the flow loop a corresponding increase in pressure drop was recorded for each component. This was validated through the milli ampere reading from the pressure sensor signals. Additionally, it was seen that the recorded flow rate values exiting each component decreased. This justified the pump pressure drop theory, wherein upon adding every new component caused an increase in the pressure drop which in turn reduced the resultant flow rate exiting the end component.

A pressure sensor was used to take the pressure readings which were recorded in milli amperes (mA). This was converted to gauge pressures (barg) and then later to atmospheric pressure (bara), using the lower and upper limits of the sensor.

The components are added in the following order:

- Swivel
- Swivel + slip ring
- Swivel + slip ring + drill pipe
- Swivel + slip ring + drill pipe + BHA
- Swivel + slip ring + drill pipe + BHA + drill bit

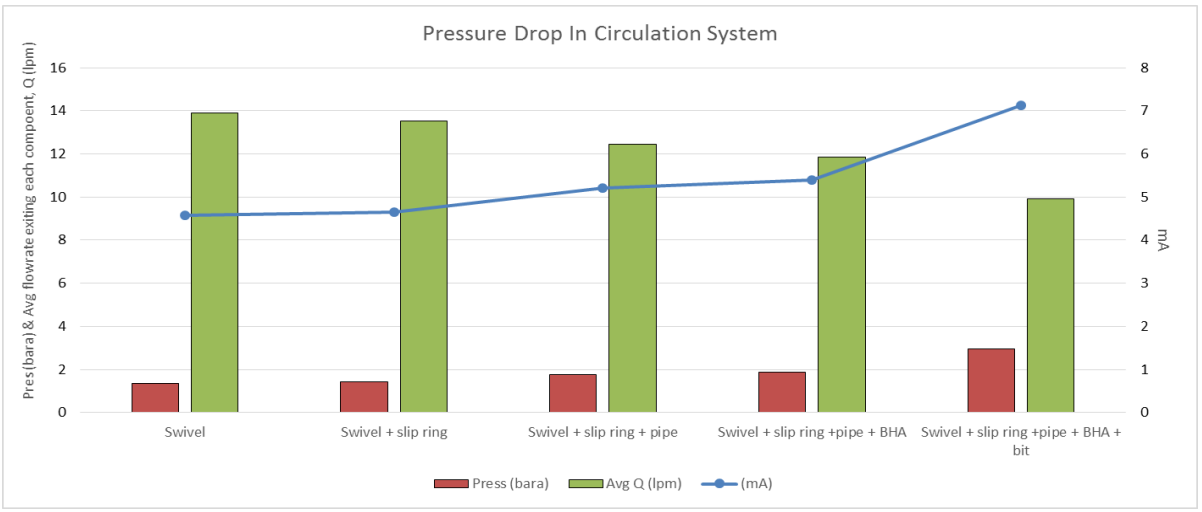

Figure 4.6: Pressure drop in circulation system.

The graphical representation generated in *Figure 4.7* was attained upon considering 36 measurements for scenarios 1 and 2.

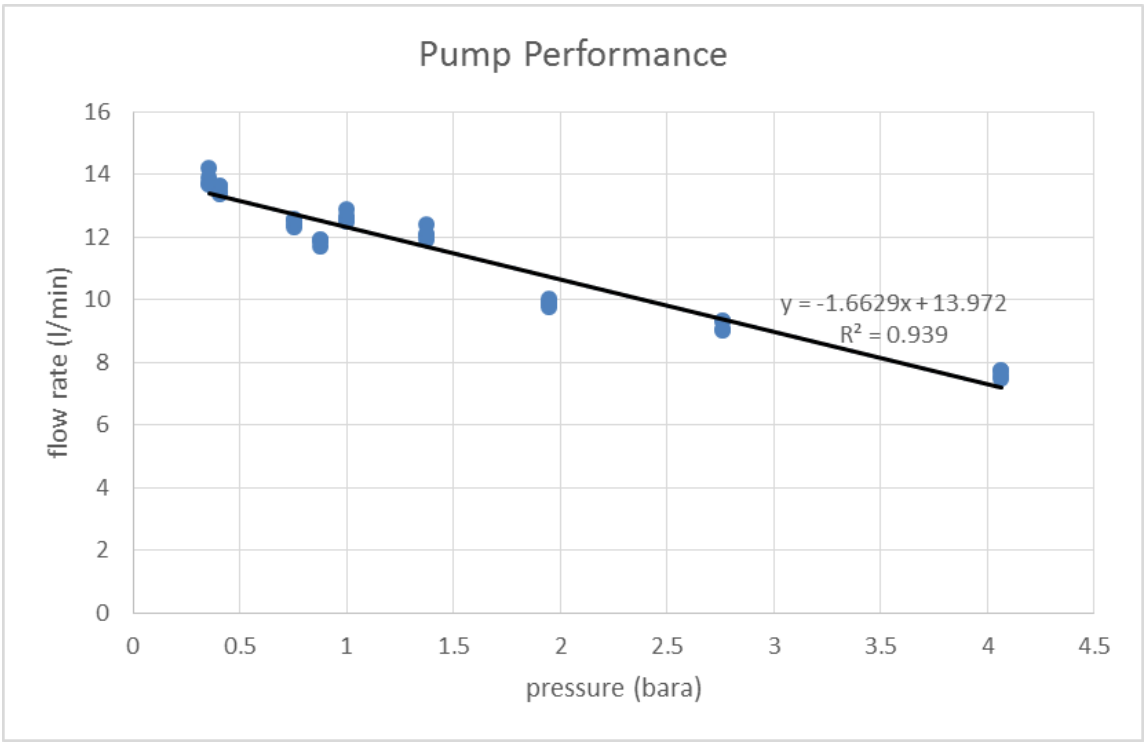

Figure 4.7: Pump performance curve obtained from the testing. Straight line showing the line of best fit for the points, with R^2=0.939

Upon systematically adding a series of components into the circulation system, the pressure sensor reading was noted. Additionally, the flowrate was derived by measuring the volume of water pumped every 10 or 20 seconds.

Calculation of pressure readings from the sensor:

Lower limit of pressure sensor @ pressure (0 barg) = 4.00 mA

Highest limit of sensor @ pressure of 10 barg = 20.00 mA

By linear interpolation, pressure equivalent of sensor reading of X mA $= \left[\frac{(X-4)}{16}.10 + 1\right] bara$

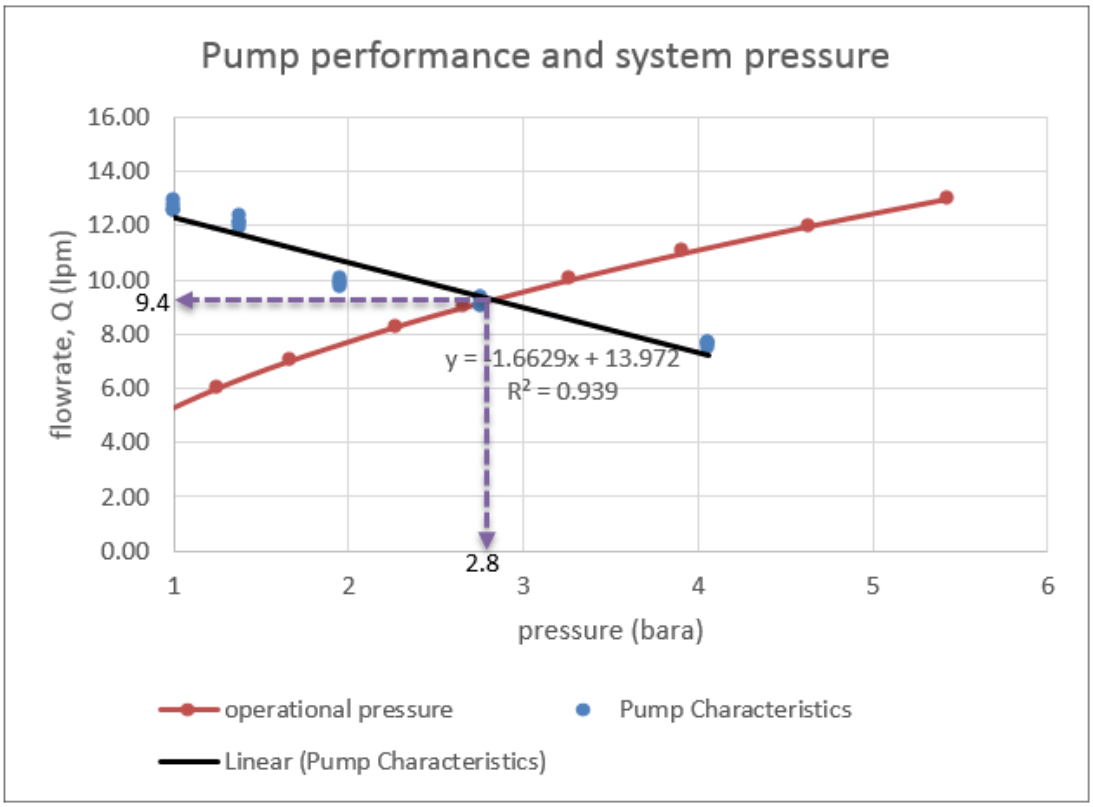

Figure 4.8: Pump performance with system pressure.

Point of intersection of the pump characteristics curve (aka pump performance) and the operational pressure loss (aka system pressure loss) derives the pump operating pressure and its corresponding flowrate. From *Figure 4.8* this indicates that a flowrate of 9.4 lpm is required to facilitate the pump operating efficiently at 2.8 bara.

5 ROP MODELLING AND APPLICATION

The modelling of rate of penetration in this work is done by using the multiple regression techniques on relevant drilling data in order to give a good estimate of the ROP. Drilling data from the Norwegian North Sea is used to ensure realistic testing of the techniques. The data is processed to be compatible with the use of Microsoft Excel. The modelling is based on using coefficients or certain values from neighboring wells to predict the ROP and comparing these with actual data. These coefficients and values are obtained by use of the models and/or techniques described in this thesis. The purpose of this work is in an attempt to improve the ability to predict the ROP for wells to be drilled near an already drilled well.

Drilling data from two fields in the Norwegian Sea is used to verify the accuracy of the models presented in this thesis. Each field is represented by two close-by wells. The drilling data was provided by the Norwegian Petroleum Directorate in the form of "Final Well Report" mud log reports for each well in portable document format (PDF). With the exception of ECD, all the pertinent data are listed for every 5-meter depth. ECD data are derived from its plotted values. The data is processed and converted to Microsoft Excel format. Further structural editing of the data was required to make it compatible for processing with in Microsoft Excel.

There are four wells considered in this thesis for the modelling of ROP. Two from block 24/6, better known as Alvheim field, located in the North Sea, approximately 224 km west of Haugesund on the west coast. The two wells used are operated by Marathon Petroleum Company (Norway), wells 24/6-B-2-H and 24/6-B-3-H. Both wells were drilled in 2008 at a water depth of 124 m MSL with 24/6-B-2-H of total depth of about 2111.1 m TVD, while 24/6-B-3-H has a total depth of about 2154.5 m to 2285.7 m TVD.

The two other wells are located in block 34/11, also known as Kvitebjør field, a gas and condensate field located east of Gullfaks and about 140 km west of Bergen, in the Norwegian North Sea. The two wells used are operated by STATOIL, wells 34/11-A-06 and 34/11-A-07. 34/11/A-06 was drilled in 2003 at a water depth of 200 m MSL and total depth of about 4457.9 m TVD. 34/11/A-07 was drilled in 2003 at a water depth of 190 m MSL and total depth of about 4380.3 m TVD.

The method of implementing the multiple regression techniques and models to predict rates of penetration in this thesis is largely based on the well-to-well correlation procedure. Together with drilling data, coefficients are used to obtain the ROP for a well. These same coefficients are then used together with "planned" drilling data for a close-by well to predict the ROP of this well. It is assumed the neighbor well will experience similar effects from drilling parameters on the ROP. The technique involves simply doing a multivariate analysis of different parameters that affect ROP. This procedure is then extended to the MSE model and the drillability d-exponent model.

8 ½ - inch hole section has been considered in all the data reportedly used in this thesis.

5.1 Multiple regression

The analysis characterizes an observation factor and several variables, taking into account changes of several properties simultaneously. In this work, rate of penetration is considered as the observation factor (Y). Relevant drilling factors make up the regression variables (let's say X_1 to X_7). These data are processed with a regression data analysis in Microsoft Excel. Thus, from this analysis, the required coefficients (b_0 to b_7) are computed. With these coefficients, it is possible to compute values for the corresponding "modelled" observation factor.

This analysis is done primarily for the 8.5-in hole sections. The data used for the multiple regression analysis in this work are WOB, torque, RPM, stand pipe pressure (SPP), flowrate, mud weight and equivalent mud weight (ECD), together with the observation factor ROP. Performing the regression data analysis in Microsoft Excel (*Figure 5.1*), ROP is input as the Y-area. The remaining data is selected as the X-area. Depth is included only as a reference and is not selected as part of the analysis. The analysis then provides output data it has computed, where the coefficients are of interest. The first value of coefficients is the intercept (b_0), while other coefficients (b_1 to b_7) are to be multiplied with the regression variables (X_1 to X_7) according to their order (*Figure 5.2*). The ROP is thus modelled by the following equation.

$$Y = b_0 + b_1X_1 + b_2X_2 + b_3X_3 + b_4X_4 + b_5X_5 + b_6X_6 + b_7X_7 \quad \text{.....5.1}$$

In terms of ROP and other parameters, the equation can be re-written as *Equation 5.2*

$$ROP = b_0 + b_1 WOB + b_2 Torque + b_3 RPM + b_4 SPP + b_5 Flowrate + b_6 MW + b_7 ECD$$

……..5.2

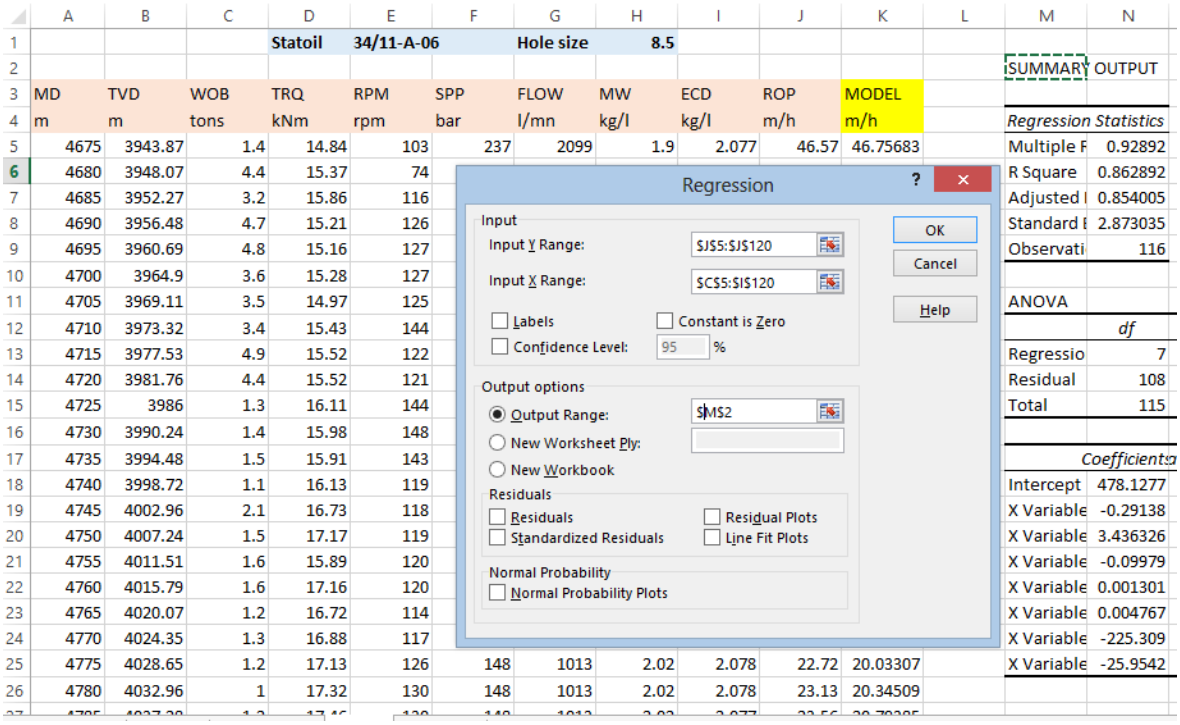

Figure 5.1: Multiple regression data analysis (Microsoft Excel)

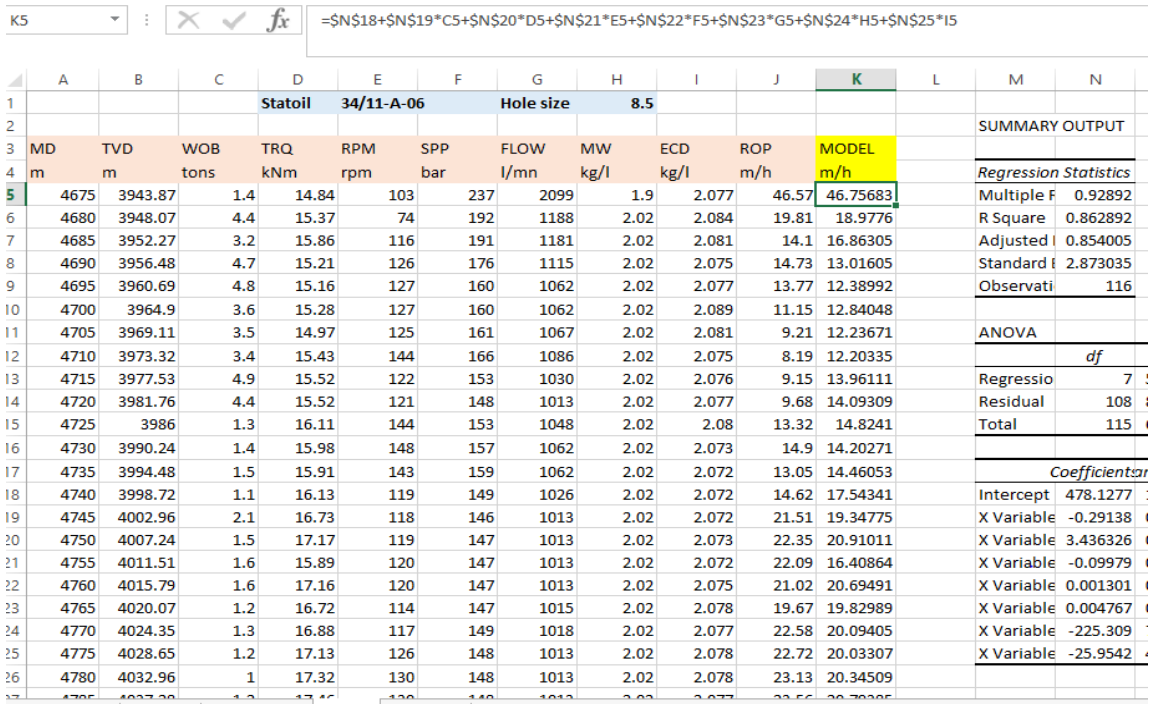

Figure 5.2: Application of Equation 5.2 in Microsoft Excel

In Microsoft Excel, *Equation 5.3* is used for to obtain the modelled ROP for each depth of a set of drilling data. The coefficients are listed from cell N18 to N25 and are denoted by a $ sign to keep their values constant for the whole procedure. Cell columns C, D, E, F, G H and I contain the regression variables, varying with depth intervals by rows. The equation computes the modelled ROP for each row by changing the row reference number.

Modelled ROP

=$N$18+$N$19*C5+$N$20*D5+$N$21*E5+$N$22*F5+$N$23*G5+$N$24*H5+$N$25*I5

……..5.3

The multiple regression procedure shown in *Figure 5.3* is done for each well, providing each with a set of coefficients. Each set of well coefficients is then applied in the model to produce ROP values for the neighboring well. With this method, it is possible to predict ROP values of the neighboring wells.

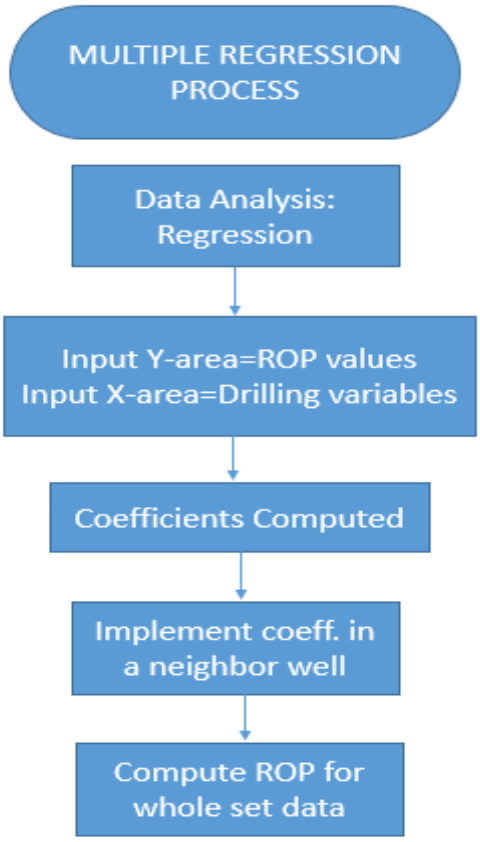

Figure 5.3: Multiple regression process flowchat

5.2 Multiple regression with MSE Model

Multiple regression technique is equally used to predict the ROP for a near-by well. In this case, we model the MSE values for a well and use the generated coefficients of regression to solve for the ROP of a nearby well. The MSE value is calculated using the model developed by Teale, as described in *Section 2.4* of this thesis.

$$MSE = \frac{4WOB}{\pi d_b^2} + \frac{480 * N * T}{d_b^2 ROP} \approx UCS$$

……5.4

The MSE model obtained from well 1 (i.e. 24/6-B-3H) is stated as follows in *Equation 5.5*. Note that these calculation is done at each depth interval starting from Row 6 of the excel figure shown (see *Figure 5.4*). The respective coefficients are obtained from the regression analysis. The expression in *Equation 5.5* can thus be transformed to *Equation 5.6*.

MSE = $L$19 + $L$20*C6 + $L$21*D6 + $L$22*E6 + $L$23*F6

……5.5

MSE = -21.0831 - 0.02477*RPM + 10.19576*TQ - 0.02379*WOB - 1.13346*ROP

……5.6

	A	B	C	D	E	F	G	H	I	J	K	L
1			24/6-B-3 AY2H									
2	MD	MD						MODEL				
3	From	To	Surf	TQ On	WOB	Avg ROP	MSE	MSE			SUMMARY OUTPUT	
4	m	m	RPM	klb-ft.ft	kp	ft/hr	ksi	ksi				
5											*Regression Statistics*	
6	4252	4254	70	13.27612	15.43234	26.24672	82.42659	82.42659			Multiple F	0.845592
7	4254	4265	138	15.4888	15.43234	86.61418	57.47768	34.87846			R Square	0.715025
8	4265	4269	138	19.91418	22.0462	52.49344	121.8688	118.5156			Adjusted I	0.678254
9	4269	4294	138	19.17662	17.63696	61.51575	100.1401	100.874			Standard E	38.64152
10	4294	4317	138	19.17662	17.63696	61.67979	99.8741	100.6881			Observati	36
11	4317	4323	138	19.17662	17.63696	62.1063	99.18897	100.2047				
12	4323	4352	138	21.3893	17.63696	67.15879	102.3072	117.0379			ANOVA	
13	4352	4381	138	21.3893	17.63696	76.11549	90.28128	106.8859				*df*
14	4381	4398	138	21.3893	22.0462	31.85696	215.5842	156.9461			Regressio	4
15	4398	4410	138	21.3893	22.0462	94.48819	72.77493	85.95632			Residual	31
16	4410	4439	138	21.3893	22.0462	76.11549	90.30847	106.781			Total	35
17	4439	4468	138	21.3893	22.0462	47.57218	144.412	139.1336				
18	4468	4497	138	21.3893	22.0462	67.15879	102.3344	116.933				*Coefficients*
19	4497	4526	138	21.3893	22.0462	76.11549	90.30847	106.781			Intercept	-21.0831
20	4526	4556	138	21.3893	22.0462	65.6168	104.7361	118.6808			X Variable	-0.02477
21	4556	4585	138	21.3893	22.0462	76.11549	90.30847	106.781			X Variable	10.19576
22	4585	4614	138	21.3893	22.0462	81.56168	84.2873	100.608			X Variable	-0.02379
23	4614	4642	138	21.3893	22.0462	61.25328	112.1875	123.6267			X Variable	-1.13346

Figure 5.4: Application of Equation 5.5 and 5.6 in Microsoft Excel

The ROP values for the near-by well (24/6-B-2H) is thus obtained using *Equation 5.7* by solving for ROP. Note that the cell numbers of the coefficients are being adjusted to the new excel file as shown in the *Figure 5.5*, and also that the values of MSE of the new well are being used.

$$ROP = (F7 - \$K\$8 - \$K\$9*C7 - \$K\$10*D7 - \$K\$11*E7) / \$K\$12 \quad \ldots\ldots\ldots\ldots\ldots\ldots 5.7$$

F7 is the MSE value for the new well at corresponding depth. The equation can thus be rewritten as:

$$ROP = (MSE_{New} - \$K\$8 - \$K\$9*RPM - \$K\$10*TQ - \$K\$11*WOB) / \$K\$12 \quad \ldots\ldots\ldots\ldots\ldots\ldots 5.8$$

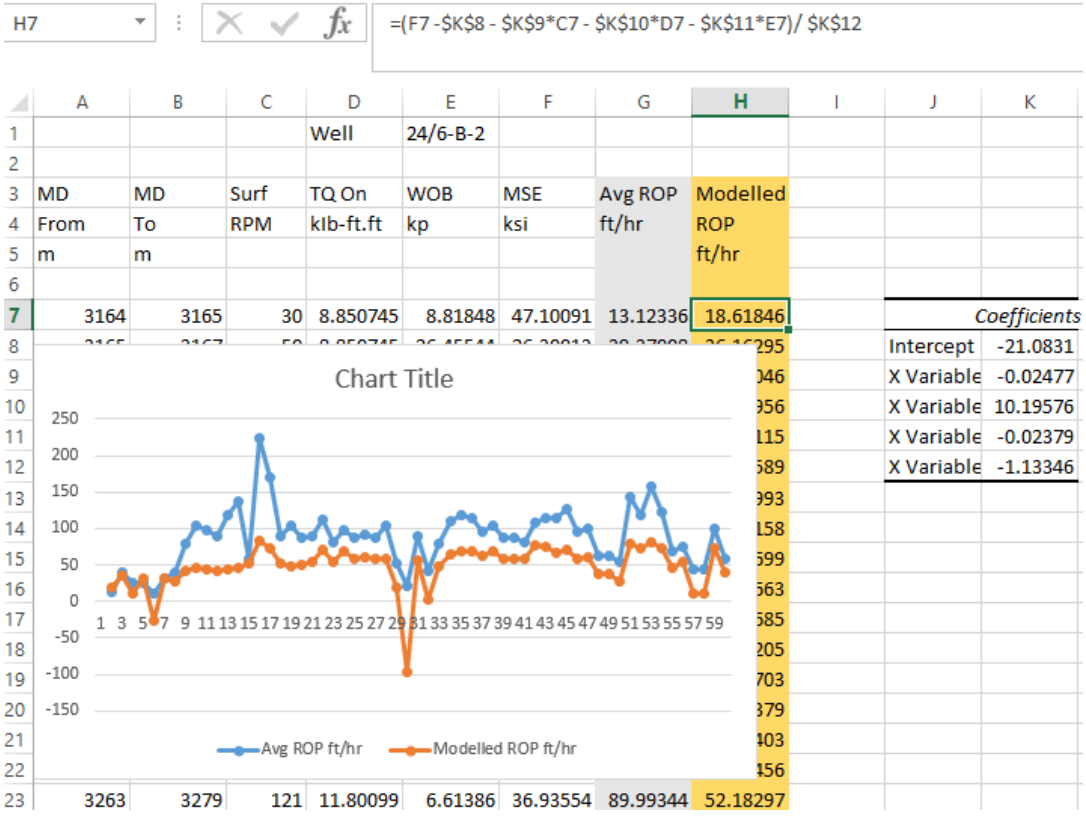

Figure 5.5: Application of Equation 5.7 in Microsoft Excel

5.3 Multiple regression with D-Exponent Model

Similar technique used in the previous section for mechanical specific energy, MSE, is applied here also for the D-exponent. The D-exponent, which is a dimensionless quantity used to describe the drillability of a formation, for well 1 (i.e. 24/6-B-3H) is obtained as from operation parameters using the equation below described in *Section 2.4*.

$$d = \frac{\log\left(\frac{ROP}{60RPM}\right)}{\log\left(\frac{12WOB}{10^3 d_b}\right)} \qquad \ldots\ldots\ldots\ldots\ldots\ldots 5.9$$

The corrected d-exponent is not used since we do not have information about the equivalent circulating density used. However, this is taken into consideration in case we have it.

The coefficients obtained from the multi regression analysis gives rise to the model in *Equation 5.10*, where the coefficients describes the hidden science of the parameters contributing to d-exponent. See *Figure 5.6* for the implementation of *Equation 5.10* in excel.

D-exp = $K$19 + C6*$K$20 + D6*$K$21 + E6*$K$22 ……5.10

Substituting the values of the coefficients and the corresponding parameters, we end up with the following expression as the model

D-exp = 0.961065 + 0.000759*RPM + 0.025535*WOB - 0.00312*ROP ……..5.11

	A	B	C	D	E	F	G	H	I	J	K
1			24/6-B-3 AY2H								
2	MD	MD									
3	From	To	Surf	WOB	Avg ROP	D-exp	MODEL			SUMMARY OUTPUT	
4	m	m	RPM	kp	ft/hr		D-exp				
5										*Regression Statistics*	
6	4252	4254	70	15.43234	26.24672	1.326373	1.326373			Multiple F	0.941803
7	4254	4265	138	15.43234	86.61418	1.19174	1.189683			R Square	0.886994
8	4265	4269	138	22.0462	52.49344	1.45857	1.464983			Adjusted I	0.876399
9	4269	4294	138	17.63696	61.51575	1.327488	1.324254			Standard E	0.047414
10	4294	4317	138	17.63696	61.67979	1.326767	1.323743			Observati	36
11	4317	4323	138	17.63696	62.1063	1.324901	1.322412				
12	4323	4352	138	17.63696	67.15879	1.303722	1.306655			ANOVA	
13	4352	4381	138	17.63696	76.11549	1.269821	1.278721				*df*
14	4381	4398	138	22.0462	31.85696	1.602508	1.529343			Regressio	3
15	4398	4410	138	22.0462	94.48819	1.289168	1.334012			Residual	32
16	4410	4439	138	22.0462	76.11549	1.351484	1.391311			Total	35
17	4439	4468	138	22.0462	47.57218	1.486941	1.480331				
18	4468	4497	138	22.0462	67.15879	1.387565	1.419245				*Coefficients*
19	4497	4526	138	22.0462	76.11549	1.351484	1.391311			Intercept	0.961065
20	4526	4556	138	22.0462	65.6168	1.39426	1.424054			X Variable	0.000759
21	4556	4585	138	22.0462	76.11549	1.351484	1.391311			X Variable	0.025535
22	4585	4614	138	22.0462	81.56168	1.331567	1.374326			X Variable	-0.00312
23	4614	4642	138	22.0462	61.25328	1.414092	1.437663				

Figure 5.6: Application of Equation 5.10 in Microsoft Excel

The ROP values for the near-by well (24/6-B-2H) are thus obtained using *Equation 5.12* by solving for ROP. Note that the cell numbers of the coefficients are being adjusted to the new excel file as shown in the *Figure 5.7*, and also that the values of D-exp of the new well are being used.

$$ROP_{New} = (E7 - \$J\$9 - \$J\$10*C7 - \$J\$11*D7) / \$J\$12 \quad \ldots\ldots\ldots\ldots\ldots\ldots 5.12$$

E7 is the D-exp value for the new well at corresponding depth. The equation can thus be rewritten as:

$$ROP_{New} = (D\text{-}Exp_{New} - \$J\$9 - \$J\$10*RPM - \$J\$11*WOB) / \$J\$12 \quad \ldots\ldots\ldots\ldots\ldots\ldots 5.13$$

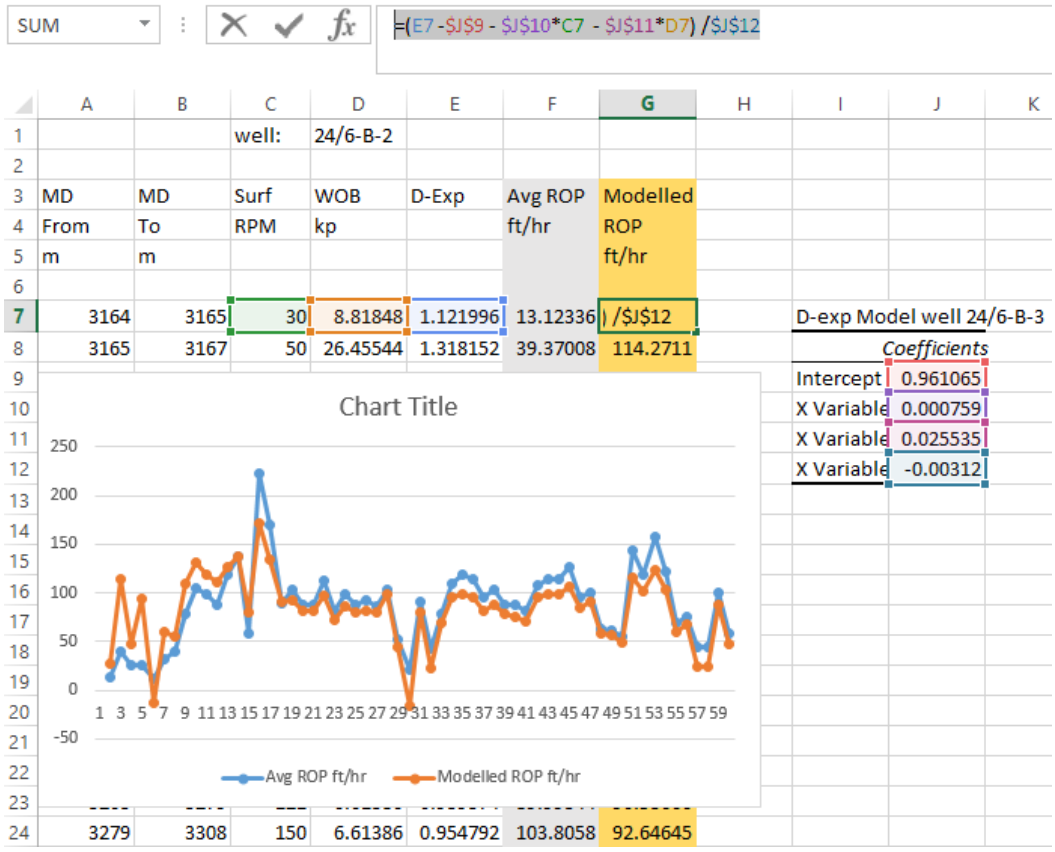

Figure 5.7: Application of Equation 5.12 in Microsoft Excel

6 RESULTS AND DISCUSSION

This chapter discusses the results obtained, challenges and limitations experienced from the Drillbotics experimental test setup. Additionally, *Section 6.2* discusses the results attained using ROP modelling techniques and analysis.

6.1 Drillbotics results

The results in this section were attained using the Drillbotics laboratory setup wherein initial testing evaluated the pump's performance in the circulation loop. Due to unforeseen challenges, only the circulation system experiments are presented in this thesis. Other experimental evaluations namely torque and power transmission, hoisting and directional control systems have not been included due to the following reasons:

- Limited time constraint for the construction of the Drillbotics testing skid.
- Last minute changes to some of the key design requirements set by the organisers (i.e. DSATS).
- More students participation required on the project to meet stringent deadline. (DSATS specified five (5), but only 3 participants were available from university of Stavanger.
- Time set-back experienced while procuring materials instrumental to constructing the test skid.

Tests results presented in *Figures 6.1* to *6.5* illustrate the effects on pump performance during different operational scenarios. Testing commenced on 9th June, 2016. Each of the figures have been analysed using two operational parameters namely flowrate (l/min) and pressure drop (bara). As emphasized in *Section 4.2*, pressure drop measurements were obtained from a pressure sensor, while the flowrates were derived using the pump performance curve (ref: *Figure 4.7)*. Additionally, during preliminary testing of the pump, two operational limits were identified beyond which the pump would cease from operating and this consequently would disrupt circulation in the flow loop. The limitations experienced during testing were coherent to real life drilling operations, wherein the ECD is limited within the pore and fracture pressures window. Ideally it is paramount to work within this window in order to mitigate drilling problems. During testing, the pressure drop was limited between 1.7 bar and 3.5 bar based on the Flojet pump's pumping capabilities.

The three (3) operational scenarios simulated were for:

- Normal operations (pressure within limit).
- Abnormal – obstruction in the system (pressure close or above upper limit)
- Abnormal – leakages in the system (pressure close or below lower limit)

6.1.1 Normal Scenario

The results obtained under normal conditions (ref: *Figure 6.1)* demonstrated that the flow rate and pressure drop readings from the experimental setup were marginally different from the results in the design calculations.

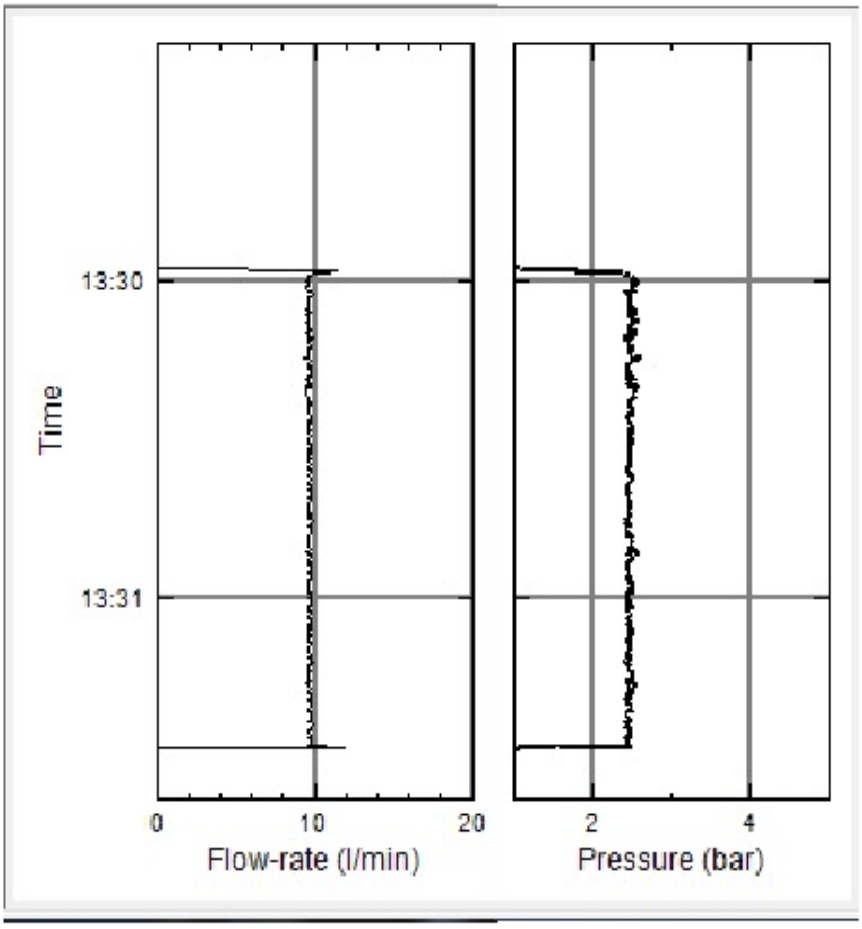

Figure 6.1: Normal operation. The pump is being run without any obstruction or leakages in the whole circulation system. Normal pressure identified was 2. 5 bar, with a corresponding flowrate of 9.8 l/min.

The design calculations model used Darcy friction factor and different pipe roughness replicating different sections of the flow loop. Below lies the comparison of the two results, wherein an adjusting factor 'K' was deduced in order to account for the marginal difference.

From *Equation 2.43*,

$$\Delta P = \frac{8\rho Q^2 f_D L}{\pi^2 D^5}$$

Every other parameter is constant apart from pressure drop, ΔP, friction factor, $f_D$and flow rate, Q.

This implies that:

$$f_D \propto \frac{\Delta P}{Q^2}$$

……..6.1

$$\therefore f_{D,exp} = \frac{\Delta P_{exp}}{Q_{exp}^2} \ and \ f_{D,model} = \frac{\Delta P_{mod}}{Q_{mod}^2}$$

Where the subscript 'exp' refers to experimental value, while 'mod' refers to model value

Thus, we can conveniently introduce an adjusting factor 'K' such that,

$$f_{D,exp} = K.f_{D,model}$$

$$K = \frac{f_{D,exp}}{f_{D,model}} = \left.\frac{\frac{\Delta P_{exp}}{Q_{exp}^2}}{\frac{\Delta P_{mod}}{Q_{mod}^2}}\right.$$

From the results under normal condition,

The pump operated efficiently at pressure, $\Delta P_{exp} = 2.5\ bar$, $Q_{exp} = 9.8\ l/min$,

While according to the model, $\Delta P_{mod} = 2.8\ bar$, $Q_{mod} = 9.4\ l/min$

$$K = \left.\frac{\frac{\Delta P_{exp}}{Q_{exp}^2}}{\frac{\Delta P_{mod}}{Q_{mod}^2}}\right. = \left.\frac{\frac{2.5}{9.8^2}}{\frac{2.8}{9.4^2}}\right. = 0.8215$$

$$K = 0.8215$$

6.1.2 Obstruction Scenarios

With small obstruction, there was pressure increase to 2.9 bar with a corresponding decrease in the flowrate from 9.8 l/min for normal to 8.4 l/min. Likewise, at medium or partial obstruction, pressure further increased to 3.1 bar, while flowrate reduced to 8.0 l/min. (Ref: *Figure 6.2).* These kinds of characteristics correspond to the relationship observed in *Figure 4.7* wherein the flowrate decreases with increasing pressure drop.

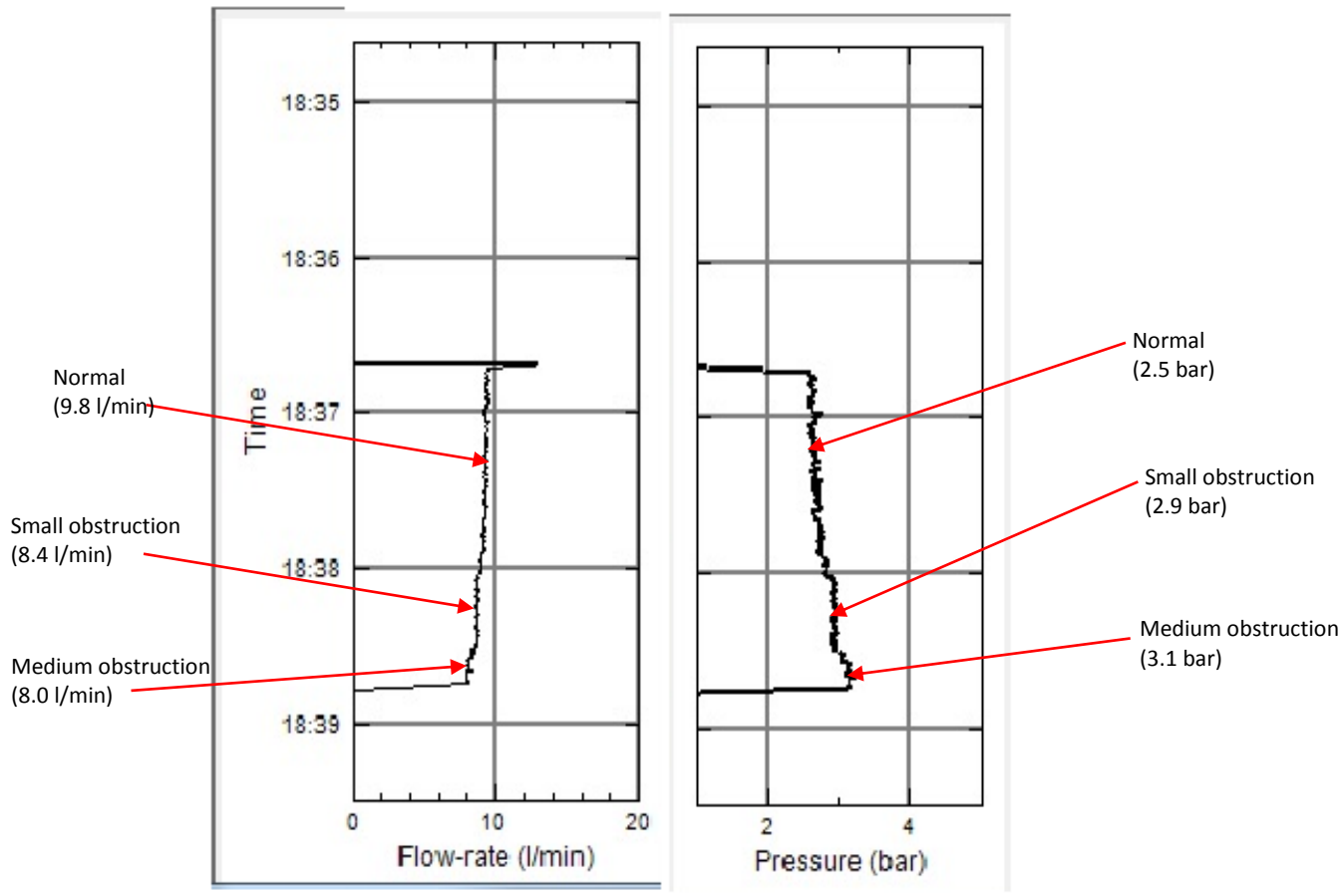

Figure 6.2: 1st scenario showing readings for small and large obstructions.

A repetition of the test was performed with a larger obstruction. (Ref: *Figure 6.3).* Minimal and medium obstructions gave similar results as before which were comparable to those in *Figure 6.2*. When simulating a larger obstruction, the pump stopped operating when the observed pressure drop was 3.4 bar which was closer to upper operational limit of the pump (i.e. 3.5 bar). The flowrate of 7.8 l/min corresponded to 3.4 bar pressure drop.

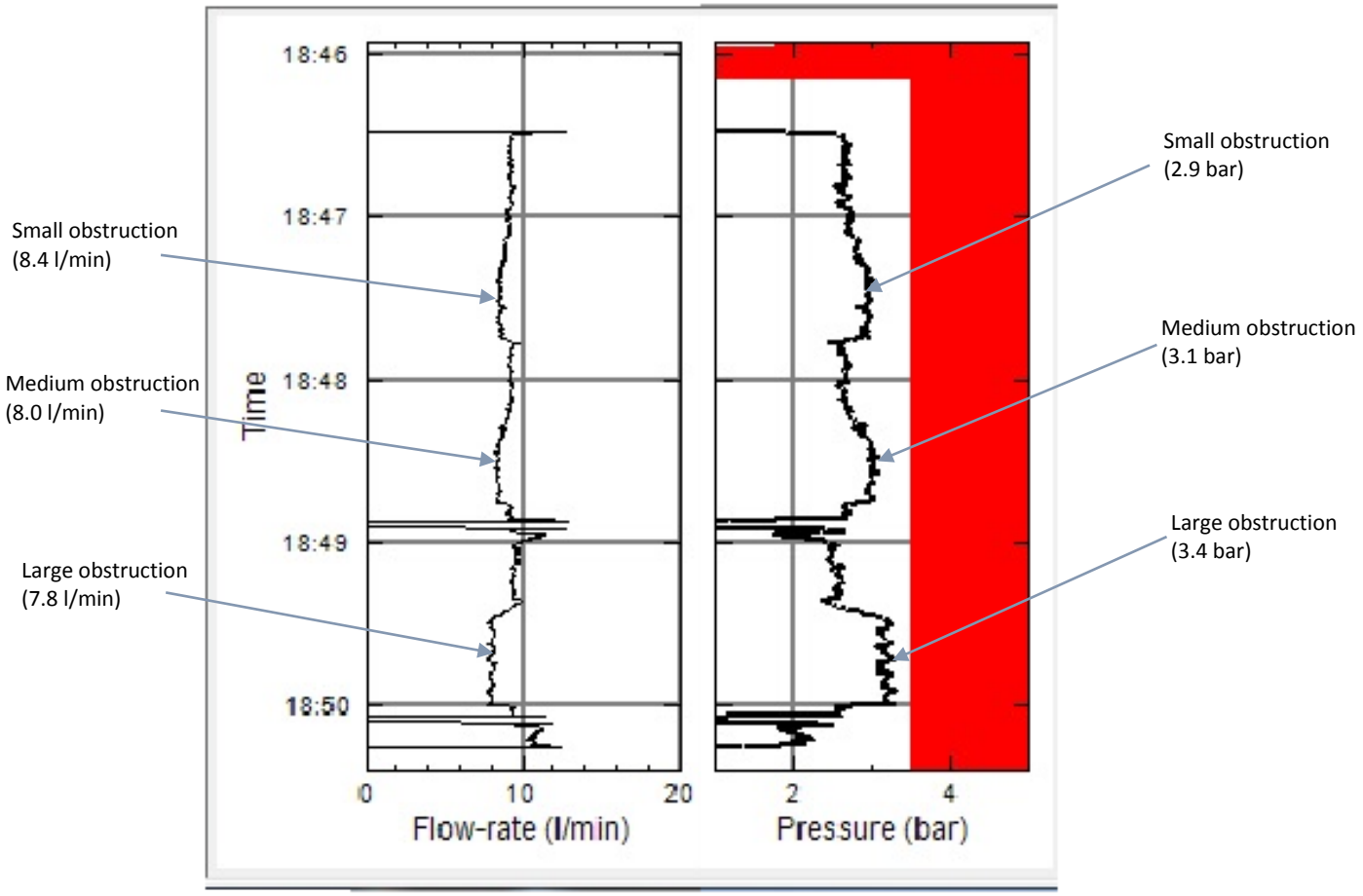

Figure 6.3: 2nd scenario showing readings for small, medium and large obstructions

6.1.3 Leakage Scenarios

The scenario that replicated a leak in the flow loop demonstrated a reduction in the pressure drop. Hence, a small leakage generates a small pressure drop, while a large leak shows a higher pressure drop. *Figures 6.4* and *6.5* collaborate these observations.

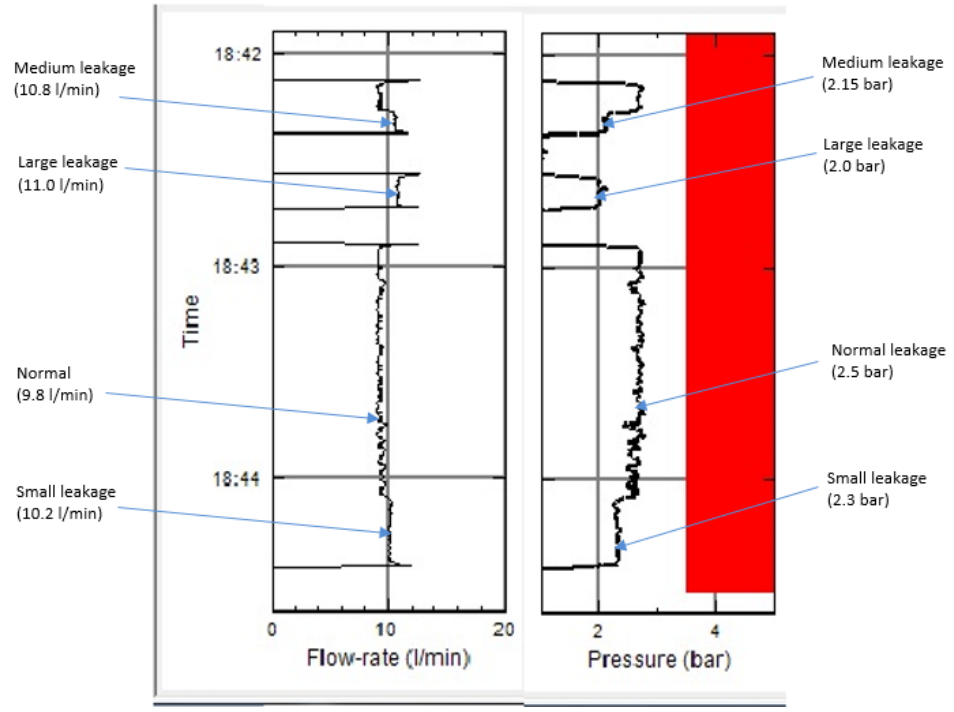

Figure 6.4: 1st Leakage scenario showing readings for small, medium and large leakages.

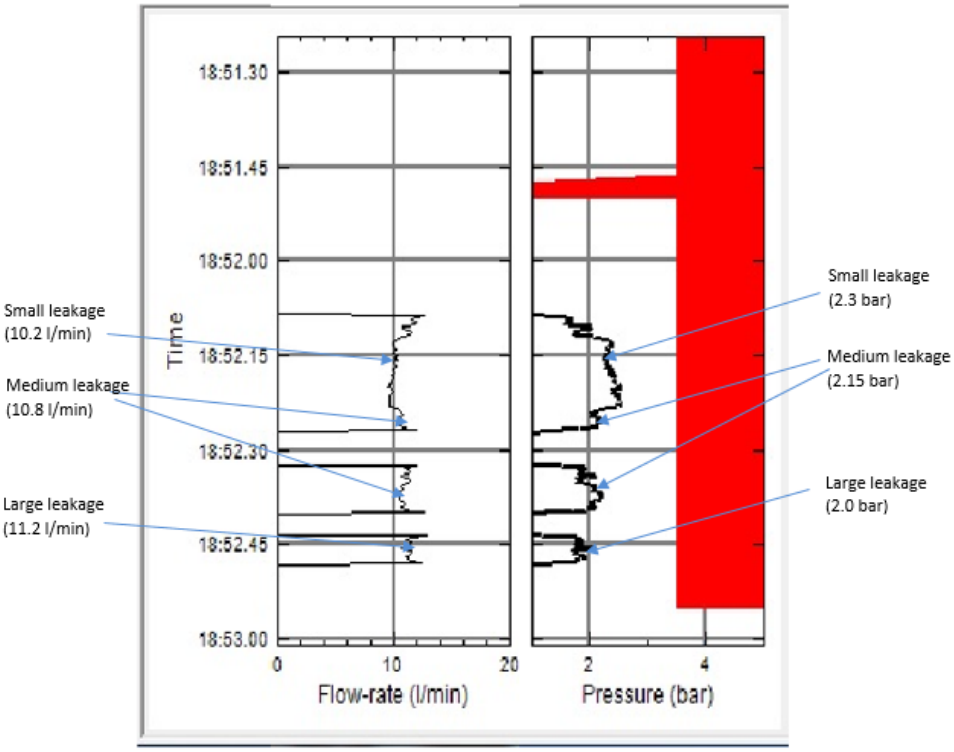

Figure 6.5: 2nd Leakage scenario showing readings for small, medium and large leakages

6.2 ROP modelling

The following section of the thesis presents the results and discussions regarding ROP modelling. Presented are coefficients obtained from the multiple regression of the operational parameters with respect to ROP as discussed in *Section 5*. The regression coefficients with respect to MSE and D-exponent are also presented, which have also been used to model the ROP of a nearby well in a known field. These plots are representative of data points along the depth of a well and their corresponding measured and modelled ROP, MSE or D-exponent values.

6.2.1 Multiple regression

The following are the coefficients obtained using the multiple regression method.

Table 1 and 2 are purely derived from other operational parameters for ROP.

34-11-A-06	Coefficients
Intercept	478.1277257
X Variable 1	-0.291375306
X Variable 2	3.436326482
X Variable 3	-0.099790251
X Variable 4	0.001300788
X Variable 5	0.004767237
X Variable 6	-225.309196
X Variable 7	-25.95421469

Table 1

34-11-A-07	Coefficients
Intercept	130.6112054
X Variable 1	0.531760146
X Variable 2	-0.33316848
X Variable 3	0.117414653
X Variable 4	-0.105471459
X Variable 5	0.003258296
X Variable 6	-53.84640649
X Variable 7	-0.764983793

Table 2

Tables 3 and 4 have been derived for MSE using other operational parameters

24-6-B-2	Coefficients
Intercept	23.6250375
X Variable 1	0.21873164
X Variable 2	4.88901861
X Variable 3	-0.45303648
X Variable 4	-0.63921968

Table 3

24-6-B-03	Coefficients
Intercept	-21.083115
X Variable 1	-0.0247681
X Variable 2	10.1957561
X Variable 3	-0.0237851
X Variable 4	-1.133457

Table 4

Tables 5 and 6 have been derived for D-exponent using other operational parameters

24-6-B-2	Coefficients
Intercept	0.82939737
X Variable 1	0.00170391
X Variable 2	0.02401244
X Variable 3	-0.00263527

Table 5

24-6-B-03	Coefficients
Intercept	0.96106549
X Variable 1	0.00075855
X Variable 2	0.02553507
X Variable 3	-0.0031187

Table 6

Figures 6.6 to 6.11 show the resulting plots upon implementing the generated coefficients versus the recorded real-time ROP, MSE or D-exponent values from the original wells. The lines in 'blue' are the original operational data of the respective field, while lines in 'red' are the modelled values from the regression coefficients tabulated under *Tables 1* to *6*.

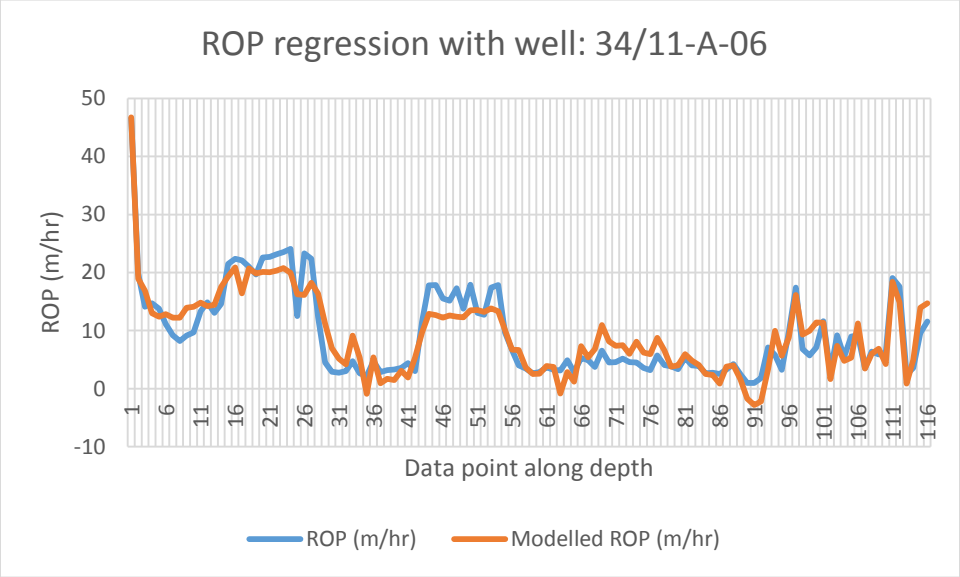

Figure 6.6: ROP multiple regression for well: 34/11-A-06. A similar trend is observed for both modelled and original data sets, with slight deviations.

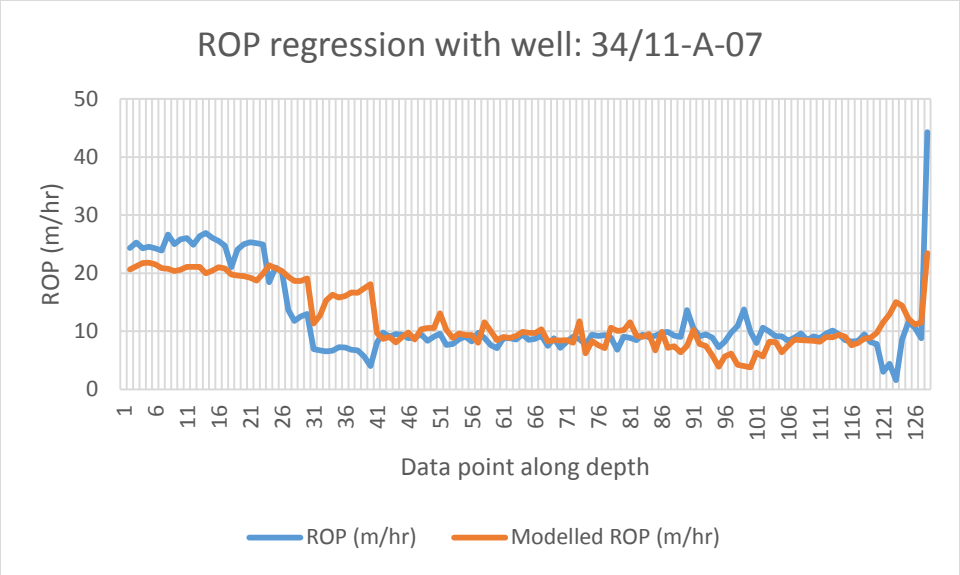

Figure 6.7: ROP multiple regression for well: 34/11-A-07. Both modelled and original data sets show similar trends. However, large deviation is observed at the early data points up to 41, and close match from point 41 to 95 and 106 to 120. This discrepancy is assumed to be affiliated with noise the data.

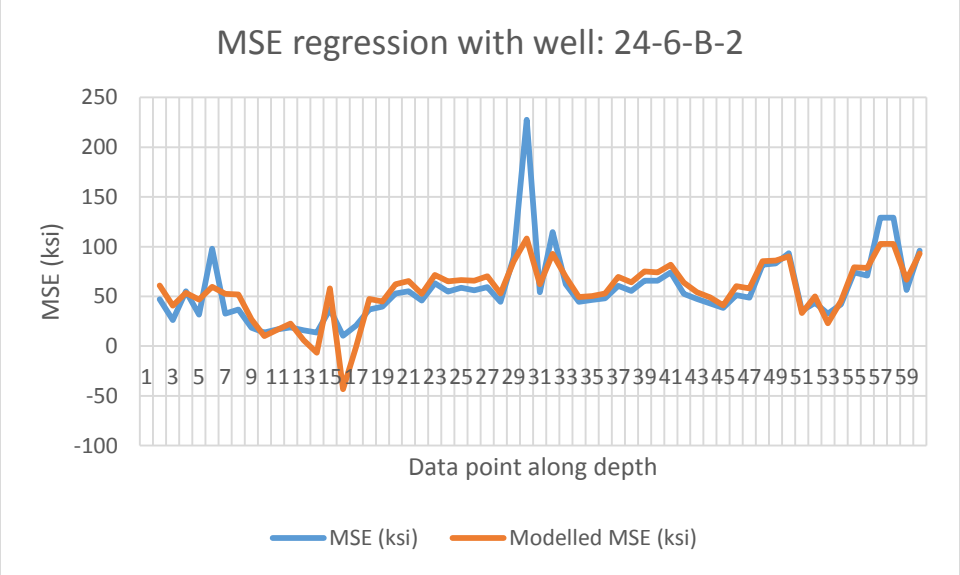

Figure 6.8: MSE multiple regression for well: 24-6-B-2. Modelled and original data set are analogous. Large deviation is observed at data points 6, 16 and 30. Slight deviation is also observed for data point ranging from 19 to 29.

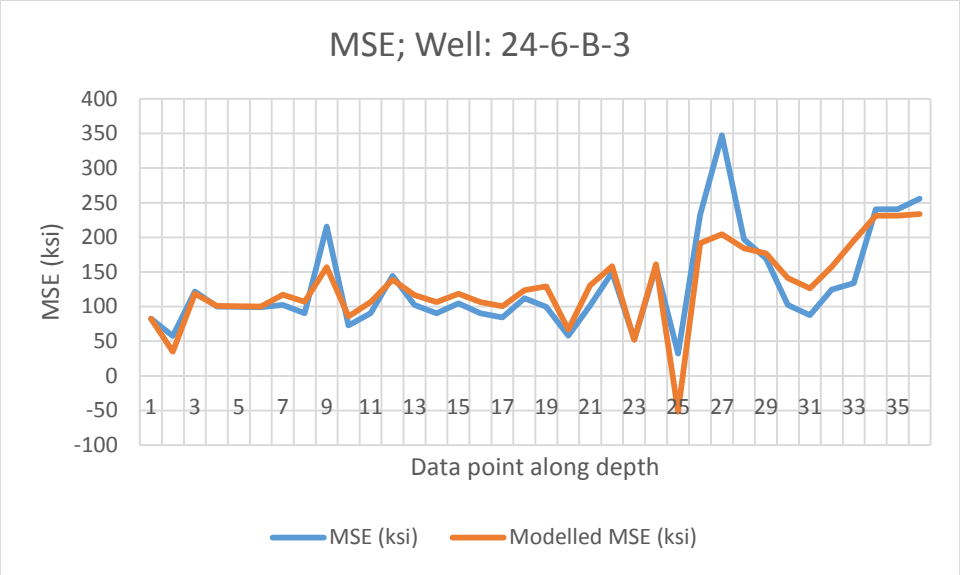

Figure 6.9: MSE multiple regression for well: 24-6-B-3. Similar trend is observed for both the modelled and the original data set. However, there are points with large overshoots.

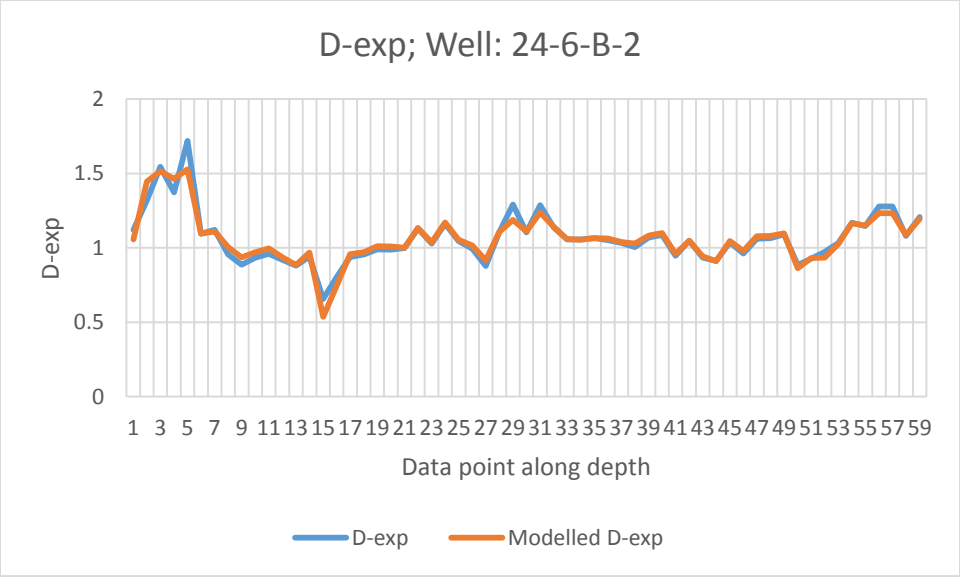

Figure 6.10: D-exponent multiple regression for well: 24-6-B-2. Modelled and original data fitted almost perfectly for all data points except at 6 and 30 that show slight deviation.

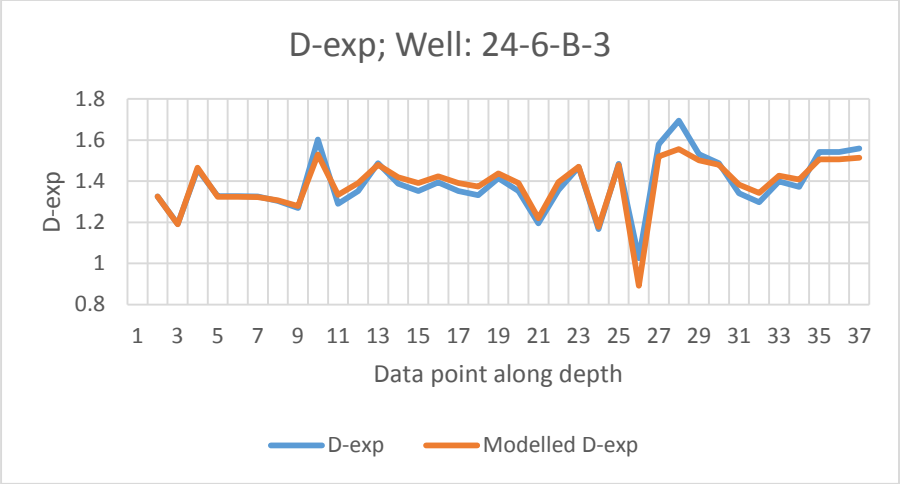

Figure 6.11: D-exponent multiple regression for well: 24-6-B-3. Both modelled and original data sets fitted almost perfectly, with slight deviations at point 27 and 28.

6.2.2 Modelling from nearby well coefficients

Figure 6.12 to *Figure 6.17* show the plots for the modelled ROP values, obtained by using the coefficients of a nearby well. In comparison, the original data sets are equally plotted on the same figure. Original data sets are in 'blue', while modelled are in 'red'. They all show similar trends even though there are slight deviations at some data points along the depth. The deviations could be attributed to noises in the original field data.

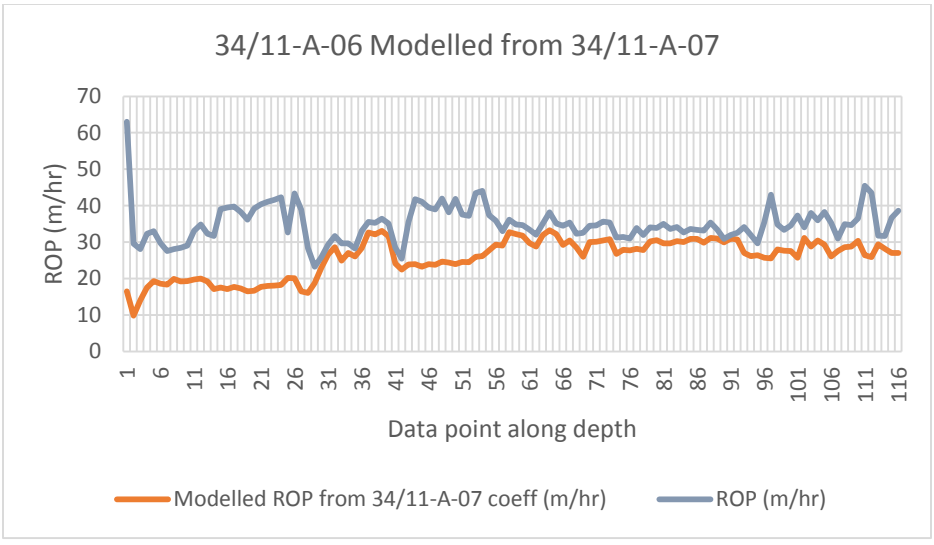

Figure 6.12: Modelled ROP of well: 34/11-A-06 from the regression coefficients of well: 34/11-A-07. Similar trend is observed. But wide variance at the beginning of the section and in the middle.

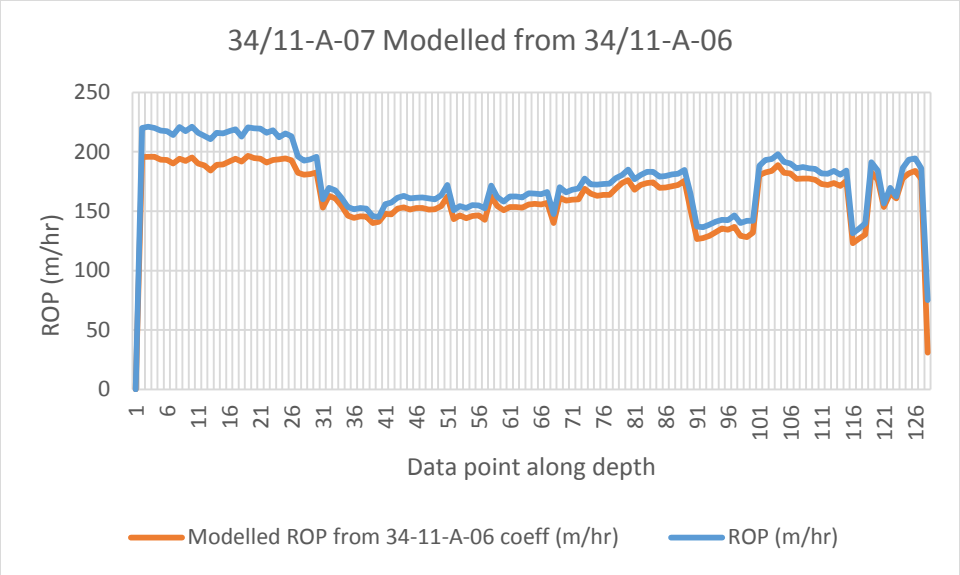

Figure 6.13: Modelled ROP of well: 34/11-A-07 from the regression coefficients of well: 34/11-A-06. Modelled and original data replicate similar trends with small discrepancies, in comparison to Figure 6.12 above

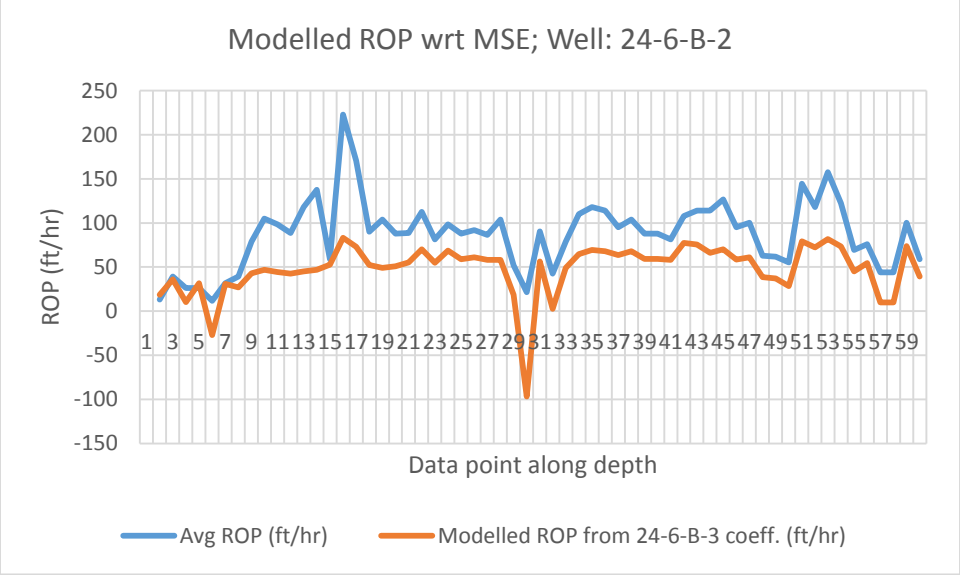

Figure 6.14: Modelled ROP of well: 24-6-B-2 from the regression coefficients wrt MSE of well: 24-6-B-3. Replicate similar trends for all the depth, with some variations. This analysis could be used to predict the behaviour of the well in terms of ROP.

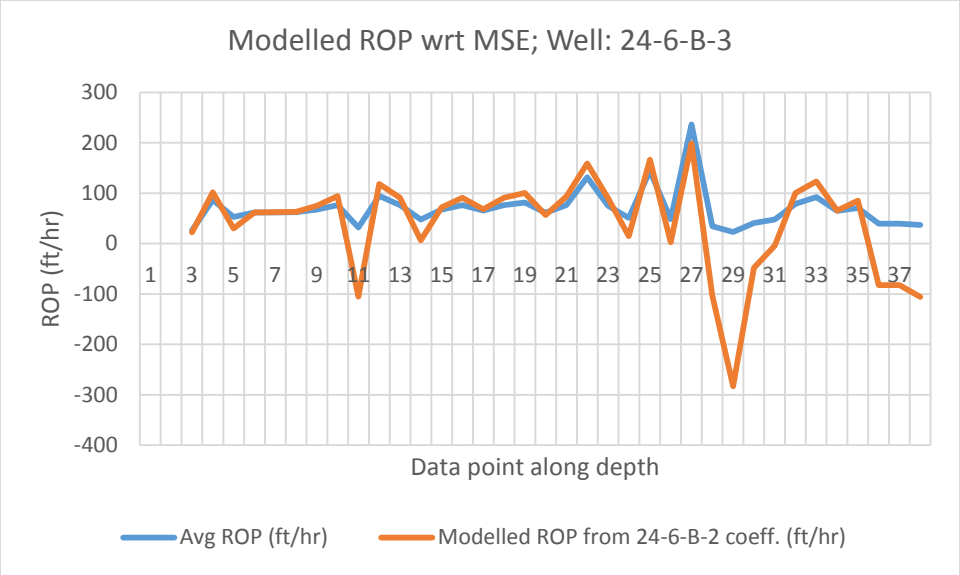

Figure 6.15: Modelled ROP of well: 24-6-B-3 from the regression coefficients wrt MSE of well: 24-6-B-2. Modelled fits perfectly with original data, up to the data point 28. The sharp deviation could result from noise from the original data.

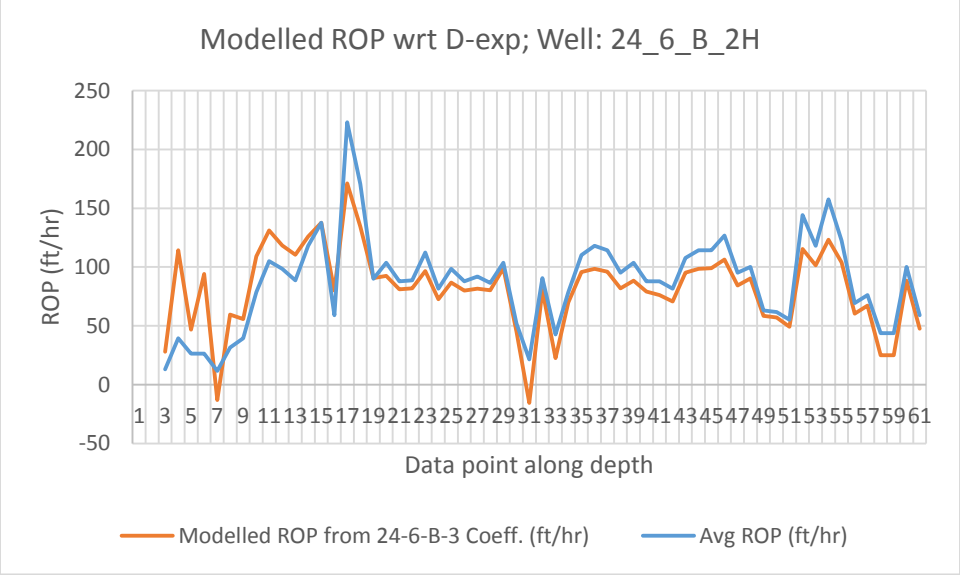

Figure 6.16: Modelled ROP of well: 24-6-B-2 from the regression coefficients wrt D-exponent of well: 24-6-B-3. Similar trend is observed. The modelled could serve as a prediction tool for the well, in order to guess the behaviour of the well.

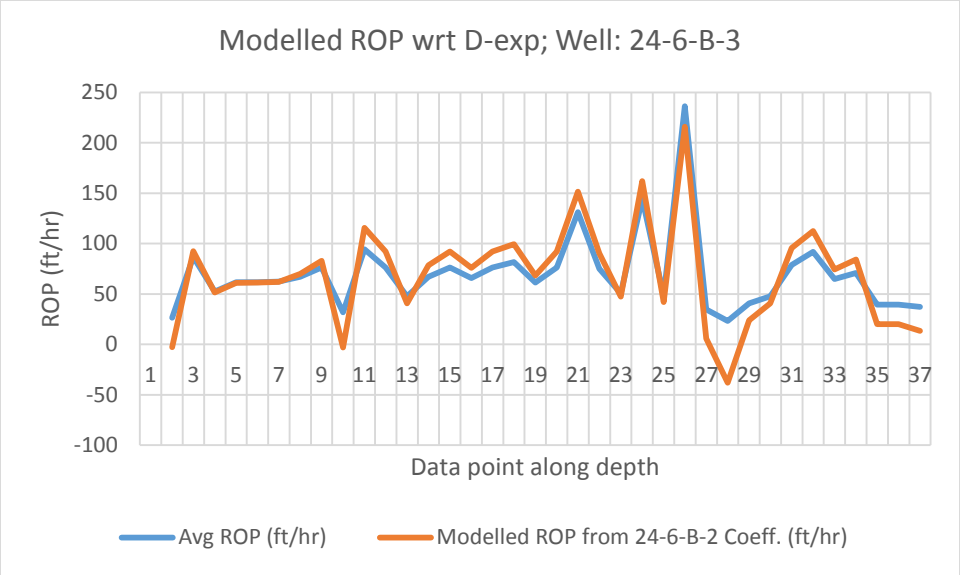

Figure 6.17: Modelled ROP of well: 24-6-B-3 from the regression coefficients wrt D-exponent of well: 24-6-B-2. Modelled fits perfectly with original data set. A significant deviation is only observed at data point 28 which lies deeper in the well.

7 CONCLUSION

Management of the rate of penetration is critical in order to ensure a steady and cost effective drilling operation. This thesis also demonstrates that variations in ROP are combined effect of several factors. Hence these factors need to be managed well in order to mitigate huge variations.

Adequate WOB, RPM, flowrate and bit torque are all necessary to avoid several bit related problems in order to increase drilling efficiency. These problems can be mitigated to some extent by focusing on the design of the circulation loop, hoisting system, torque and power transmission systems.

The Drillbotics experimental setup which was designed and discussed in this thesis, was capable of communicating with the PC controller, as evident from the test results. The collaborative functionality of this whole setup could have been discussed in further details should additional time and personnel resources were available.

Differences in pipe dimensions (i.e. drill pipe thickness) was critical in initiating the design phase, as this considerably affected the moment of inertia of the drill pipe which consecutively influenced the operational limits. The pipe dimensions were modified late during the project upon requests of the Drillbotics steering committee. Hence this made adaptation of the new design challenging as several elements required adjustments and re-designing of the test skid.

A prototype PDC bit was designed, tested and successfully reviewed in this thesis. Hence, it is recommended that a comparative analysis of the rate of penetration be conducted using another bit type such a roller cone.

Additionally, it was observed that when a drill pipe was in compression, its deflection contributed to reduction in its buckling limit. Hence further research should be emphasized towards comprehending the relationship between of drill pipe deflection and minimum potential energy in a cantilever beam.

While monitoring deflection in the test drill string setup, accelerometers were used to ensure hole verticality. However substantial background signal noises were recorded. These noises were filtered out using FFT method (Fast Fourier Transform) and low pass filters in order to attain accurate inclination readings.

Load cells were used in generating readings for torque and hook-load. It was observed that as the signals read from the load cells were weak, they required to be boosted. The amplifiers boosted the output signals which consecutively increased the accuracy.

In order to minimize HSE related issues, costs and increased efficiency of operations, substantial emphasis was allocated towards a thoroughly structured design and autonomous algorithm in this thesis.

The prediction of ROP for a well using multiple regression coefficients methodology from a neighboring well is an approach that can be easily utilized to study the ROP behavior of a new well during the planning phase for better costs estimation. This thesis has also been able to prove and validate theoretically that this approach is reliable. As this thesis has considered wells on the same block, it has been able to corroborate results from work performed also by Morten Husvæg. However, further efforts should be allocated towards predicting ROP for wells in neighboring blocks.

Similar lithological and downhole conditions on a block would facilitate correlations with respect to computing the ROP of wells in the vicinity. Formation properties have coherent effects on ROP, drillability and MSE. A majority of the modelled ROP curves in this thesis closely replicate the actual ROP trends.

As bit ROP is dependent on several other factors such as formation properties, bit type, drilling fluid properties, operating hole conditions and bit hydraulics, the regression coefficients obtained from these analysis withholds dedicated effects of these independent factors. Hence, this approach should be extended to wells in different blocks, with similar lithologies.

REFERENCES

1. SPE_DSATS, *Drillbotics Guidelines.* 2015.
2. Bratton, T., et al. "*Rock strength parameters from annular pressure while drilling and dipole sonic dispersion analysis*." SPWLA 45th Annual Logging Symposium. Society of Petrophysicists and Well-Log Analysts. 2004.
3. Aadnoy, B. and R. Looyeh, "*Petroleum rock mechanics: drilling operations and well design*" Oxford: Gulf Professional Publishing. 2011.
4. Momeni, E., et al., "*Prediction of uniaxial compressive strength of rock samples using hybrid particle swarm optimization-based artificial neural networks."* Measurement, **60**: p. 50-63. 2015.
5. Oyler, D.C., C. Mark, and G.M. Molinda, "*In situ estimation of roof rock strength using sonic logging."* International Journal of Coal Geology, **83**(4): p. 484-490.2010.
6. Amani, A. and K. Shahbazi, "*Prediction of Rock Strength using Drilling Data and Sonic Logs."* International Journal of Computer Applications, **81**(2). 2013.
7. Mitchell, R.F. and S.Z. Miska, *Fundamentals of drilling engineering.* SPE Textbook series, vol. 12. 2011.
8. Warren, T. and A. Sinor. "*Drag bit performance modeling*." SPE Annual Technical Conference and Exhibition. Society of Petroleum Engineers. 1986.
9. Boryczko, P., "*Drill bit selection and optimization in exploration well 6507/6-4A in the Nordland Ridge Area."* M.S. thesis, UIS, Stavanger, 2012.
10. Brett, J.F., T.M. Warren, and S.M. Behr, "*Bit whirl: A new theory of PDC bit failure.*" SPE Annual Technical Conference and Exhibition. Society of Petroleum Engineers. 1989.
11. Wells, M., T. Marvel, and C. Beuershausen, "*Bit balling mitigation in PDC bit design*." IADC/SPE Asia Pacific Drilling Technology Conference and Exhibition. Society of Petroleum Engineers. 2008.
12. PetroWiki, "*Principles for Polycrystalline Diamond Compact (PDC) bit design."* 2016. [online]. Available: http://petrowiki.org/PDC_bit_design. [Accessed on: 15.02.2016]
13. Warren, T., "*Penetration rate performance of roller cone bits."* SPE Drilling Engineering, **2**(01): p. 9-18. 1987.
14. Aadnoy, B.S., *Modern well design.* London: CRC Press. 2010
15. Dupriest, F.E. and W.L. Koederitz. "*Maximizing drill rates with real-time surveillance of mechanical specific energy*." SPE/IADC Drilling Conference. Society of Petroleum Engineers. 2005.
16. Teale, R. "*The concept of specific energy in rock drilling*." *International Journal of Rock Mechanics and Mining Sciences & Geomechanics Abstracts*. Elsevier. 1965.
17. Hammoutene, C. "*FEA Modeled MSE/UCS Values Optimize PDC Design for Entire Hole Section*." North Africa Technical Conference and Exhibition. Society of Petroleum Engineers. 2012.
18. Pessier, R. and M. Fear. "*Quantifying common drilling problems with mechanical specific energy and a bit-specific coefficient of sliding friction*." SPE Annual Technical Conference and Exhibition. Society of Petroleum Engineers. 1992.
19. Bourgoyne Jr, A. and F. Young Jr, "*A multiple regression approach to optimal drilling and abnormal pressure detection."* Society of Petroleum Engineers Journal. **14**(04): p. 371-384. 1974.
20. Eren, T., "*Real-time-optimization of drilling parameters during drilling operations*.", Middle East Technical University. 2010.
21. Rashidi, B., G. Hareland, and R. Nygaard. "*Real-time drill bit wear prediction by combining rock energy and drilling strength concepts*." Abu Dhabi International Petroleum Exhibition and Conference. Society of Petroleum Engineers. 2008.
22. Eckel, J.R., "*Microbit studies of the effect of fluid properties and hydraulics on drilling rate."* Journal of Petroleum Technology, **19**(04): p. 541-546. 1967.

23. Rastegar, M., et al. "*Optimization of multiple bit runs based on ROP models and cost equation: a new methodology applied for one of the Persian Gulf carbonate fields*." IADC/SPE Asia Pacific Drilling Technology Conference and Exhibition. Society of Petroleum Engineers. 2008.
24. Motahhari, H., et al., "*Method of optimizing motor and bit performance for maximum ROP."* Journal of Canadian Petroleum Technology, **48**(06): p. 44-49. 2009.
25. Rabia, H., "*Well Engineering & Construction*." Entrac Consulting Limited. 2002.
26. Ablard, P., et al., "*The expanding role of Mud logging."* Oilfield Review, **24**(1): p. 24-41. 2012
27. Jorden, J. and O. Shirley, "*Application of drilling performance data to overpressure detection."* Journal of Petroleum Technology, **18**(11): p. 1,387-1,394. 1966.
28. Rehm, B. and R. McClendon. "*Measurement of formation pressure from drilling data*. " Fall Meeting of the Society of Petroleum Engineers of AIME. Society of Petroleum Engineers. 1971
29. Runger, G.C. and D.C. Montgomery, "*Applied statistics and probability for engineers."* John willey & sons. Inc. New York, 2002.
30. Davis, J.C. and R.J. "Sampson, *Statistics and data analysis in geology*." Vol. 646. 1986: Wiley New York et al. 1986.
31. Explorable.com, "*Multiple Regression Analysis."* 2009. [Online]. Available: https://explorable.com/multiple-regression-analysis. [Accessed on 05.05.2016].
32. Berger, D.E., *Introduction to multiple regression.* Claremont Graduate University, 2003.
33. Wikipedia_Contributors, "*Darcy–Weisbach equation."* 2016. [Online]. Available: https://en.wikipedia.org/w/index.php?title=Darcy%E2%80%93Weisbach_equation&oldid=702810527.
34. Foster, J.H., "*Duff Norton Rotary Unions."* Available: https://www.jhf.com/Catalog_v6/0403.pdf
35. Lyons, W.C. and G.J. Plisga, *Standard handbook of petroleum and natural gas engineering*: Gulf Professional Publishing. 2011.
36. TheEngineeringToolBox, "*Pumps in Parallel or Serial."* 2015. [Online]. Available: http://www.engineeringtoolbox.com/pumps-parallel-serial-d_636.html. [Accessed on: 19.02.2016].
37. PetroWiki, "*Cutting Transport", 2015.* [Online]. Available: http://petrowiki.org/index.php?title=Cuttings_transport&oldid=48274. [Accessed on: 13.04.2016].
38. Chien, S.-F., "*Settling velocity of irregularly shaped particles".* SPE Drilling & Completion, **9**(04): p. 281-289. 1994.
39. Fjar, E., et al., *Petroleum related rock mechanics*. Vol. 53: Elsevier, 2008.
40. Walker, B.H., "*Some technical and economic aspects of stabilizer placement".* Journal of Petroleum Technology, 1973. **25**(06): p. 663-672.
41. Directional_Drilling_Club, "*Deflecting a Wellbore"*. 2012. [Online]. Available: https://sites.google.com/site/directionaldrillingclub/deflecting-a-wellbore. [Accessed on: 19.02.2016].
42. Sawaryn, S.J. "*Simple Engineering Applications Recycled as Effective Training Aids*." in *SPE Annual Technical Conference and Exhibition*. 2011. Society of Petroleum Engineers.
43. Toutain, P., "*Analyzing drill string behavior-2. results of two-dimensional study give recommendations for inclination control"*. World Oil;(United States), 1981. **193**(1).
44. PetroWiki, "*Bottom hole assembly (BHA) design for directional control,"* 2015. [Online]; Available: http://petrowiki.org/Bottom_hole_assembly_(BHA)_design_for_directional_control.
45. Sawaryn, S.J. and P.D. Pattillo, *The Stability of a Pipe Stand Racked in a Derrick, Part 2—A General Pipe-Stand Model.* SPE Journal, 2014. **19**(03): p. 476-486.
46. Cayeux, E., et al., "*Drill-string Mechanics: Analysis of Drill-string Deformations"*. IRIS, Stavanger, Rep. No. 2014/459, 2015.
47. Enginerring_ToolBox, "*Calculating Pipes Weight"*. [Online]. Available: http://www.engineeringtoolbox.com/pipe-weight-calculation-d_745.html. [Accessed on: 01.05.2016].

48. Wikipedia_Contributors, "*Shear Strength"*. [Online]. Available: https://en.wikipedia.org/w/index.php?title=Shear_strength&oldid=687952864. [Accessed on: 29.04.2016].
49. Wikipedia_Contributors, "*Buckling"*. [Online]. Available: https://en.wikipedia.org/w/index.php?title=Buckling&oldid=722359262. [Accessed on: 28.05.2016].
50. Schlumberger, *Oilfield Glossary, "Eccentricity"*. [Online]. Available: http://www.glossary.oilfield.slb.com/Terms/e/eccentricity.aspx. [Accessed on: 01.05.2016].

APPENDICES

Appendix A

Mauren Model:

$$ROP = \frac{K}{S^2}\left[\frac{WOB}{d_b} - \left(\frac{WOB}{d_b}\right)_t\right]^2 N$$

……A-1

Where:

K = constant of proportionality

S = compressive strength of the rock

d_b = bit diameter

$\left(\frac{WOB}{d_b}\right)_t$ = threshold bit weight

N = rotary speed (RPM)

The assumption of perfect bottomhole cleaning as well as incomplete bit tooth penetration was considered. Maurer's theoretical equation can also be verified by use of experimental data, obtained at low WOB and RPM.

Bingham suggested the equation below based on considerable laboratory and field data.

$$ROP = K\left(\frac{WOB}{d_B}\right)^{a_5} N$$

……A-2

Where:

K = proportionality constant that includes the effect of rock strength

a_5 = bit weight exponent

The threshold bit weight, $\left(\frac{WOB}{d_B}\right)_t$, was assumed to be negligible, and a_5 to be determined experimentally for the predominant conditions.

Warren's Perfect Cleaning Model:

$$ROP = \left(\frac{aS^2 d_b^3}{N^b WOB^2} + \frac{c}{N d_b}\right)^{-1}$$

……..A-3

The first term, $(\frac{aS^2 d_b^3}{N^b WOB^2})$ defines the maximum rate at which the bit breaks the formation into cuttings. The second term, $\frac{c}{N d_b}$ also takes into account the spread of the applied WOB to more teeth, and as the teeth penetrate deeper into the rock as WOB increases.

Where a, b, c are dimensionless bits constants based on experiment; $d_b$is dit diameter; S is confined rock strength and N is RPM. [13, 23]

Hareland and Rampersad Model:

$$ROP = W_f \left(\frac{G.RPM^{\gamma}.WOB^{\alpha}}{d_b.\sigma}\right)$$

……..A-4

Where α and γ are ROP model WOB and RPM exponents respectively.

The wear function is $W_f = 1 - \left(\frac{\Delta BG}{8}\right)^{\omega}$

And $\Delta BG = C_a.\sum_{i=1}^{n} RPM^{C_1}.\left(\frac{WOB}{1000}\right)^{C_2}\left(\frac{\sigma}{1000}\right)x_i$

ω is the wear function exponent. $C_a$is a property of the bit, $C_1$and $C_2$are bit wear model exponents and x_i is length of ith interval.

Real-Time Bit Wear Model Development:

This is derived from the Borgouyne & Young model by inverting the model to estimate the formation drillability f_1 (in ft/hr.), as stated in the body of this work.

$$f_1 = \frac{ROP}{f_2 * f_3 * f_4 * f_5 * f_6 * f_7 * f_8}$$

……A-5

The mechanical specific energy (MSE) applies the ROP value directly in its expression. Thus, to find a relationship between MSE value and rock drillability, a new model is proposed, which was originally in the power form as:[9, 21]

$$MSE = K_1 * \left(\frac{1}{f_1}\right)^{K_2}$$

……A-6

Where both K_1 and K_2 are constants obtained from the offset wells data. These are site-specific, and peculiar to the particular field conditions.

Imperfect-Cleaning Model:

$$ROP = \left(\frac{aS^2 d_b^3}{\mathrm{N} * WOB^2} + \frac{b}{N d_b} + \frac{c d_b \gamma_f \mu}{F_{jm}}\right)^{-1}$$

…….A-7

Appendix B

Other criteria used to determine the equivalent diameter in the annulus include the following:

1. The geometry term in Lamb's pressure loss equation for the lamina flow region, considering concentric annular flow.

$$D_e = \sqrt{{d_2}^2 + {d_1}^2 - \frac{{d_2}^2 - {d_1}^2}{In(d_2/d_1)}}$$

…….B-1

2. Comparison the Lamb's equation to the slot flow approximation for an annulus.

$$D_e = 0.816(d_2 - d_1)$$

……..B-2

3. Empirical expression developed by Crittendon from a study of about 100 hydraulic fracture treatments of producing wells.

$$D_e = \frac{\sqrt[4]{{d_2}^4 - {d_1}^4 - \frac{({d_2}^2 - {d_1}^2)^2}{In(d_2/d_1)}} + \sqrt{{d_2}^2 - {d_1}^2}}{2}$$

……B-3

In drilling operations, most annular geometrics we come across have $d_1/d_2 > 0.3$, and equation 2.52 in the body of this thesis, while equations B-1 and B-2 give almost similar results.

Appendix C

Eccentricity of Annulus

- Used to describe how off-set the pipe is in the hole.
- Usually expressed in percentages or fractions
- Fully eccentric (100%) annulus is if BHA/pipe is lying against the walls of the hole, while a perfectly centered pipe(i.e concentric) has 0% eccentricity

Frictional pressure drop in an eccentric annulus is lesser than in the concentric annulus by a correction factor. For lamina flow in Newtonian fluid, difference is about 50%, while turbulent is about 30%. For non-Newtonian fluid, the effect is less but still significant.[50]

Figure C-1: Types of pipe/annular eccentricity

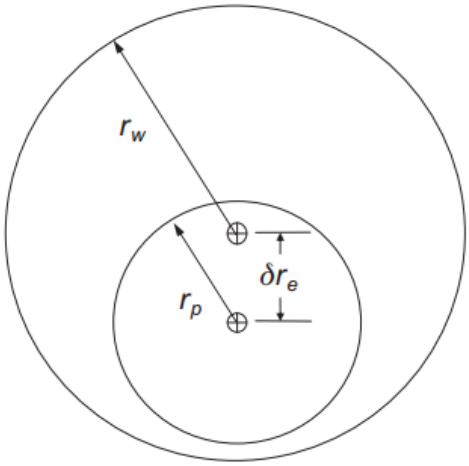

Fig. 5.38—Definition of an eccentric annulus.

Figure C-2: Definition of an eccentric annulus

Considering the figure C-2 above, Eccentricity 'N_e' is expressed as follows. [7]

$$N_e = \frac{\delta r_e}{r_w - r_p} = \frac{\delta r_e}{ID_{hole} - OD_{pipe}}$$

……..C-1

While the Correction factor, C_e for eccentricity is defined as the ratio of the frictional pressure drop for an eccentric annulus/pipe to that of a fully concentric annulus/pipe. i.e.

$$C_e = \left(\frac{dp}{ds}\right)_e \Big/ \left(\frac{dp}{ds}\right)_c$$

……..C-2

For a Newtonian fluid like water in a lamina flow region,

$$C_e = \frac{2}{2 + 3{N_e}^2}$$

…….C-3

While in a turbulent region, correction factor is:

$$C_e = \frac{1}{1 - 0.1975N_e + 1.8{N_e}^2 - 1.0625{N_e}^3}$$

……C-4

However, for a non-Newtonian fluid, considering Power law, in a lamina flow region $C_e$is obtained as follows.

$$C_e = 1 - 0.072\left(\frac{N_e}{n}\right)\left(\frac{r_p}{r_w}\right)^{0.8454} - 1.5{N_e}^3\sqrt{n}\left(\frac{r_p}{r_w}\right)^{0.1852} + 0.96{N_e}^3\left(\frac{r_p}{r_w}\right)^{0.2527} \quad \text{.....C-5}$$

And for turbulent flow,

$$C_e = \left(\frac{{u_c}^*}{{u_e}^*}\right)^2 \quad \text{.....C-6}$$

Where

$$u^* = \sqrt{\frac{\tau}{\rho}} \quad \text{.....C-7}$$

$u^*$is the flow velocity, n is power law flow exponent, τ is the shear stress and ρ the density of fluid.

Subscript "e" stands for eccentric pipe/annulus, while "c" stands for 100% concentric pipe/annulus.

Appendix D

Modelling of Accelerometers in DrillBotics 2016 (IRIS internal document)

An accelerometer is placed at a distance r" from the center of rotation of a pipe. The pipe rotates with an angular velocity $\dot{\theta}$" (the first derivative compared to time of the angle, θ"). The pipe axis rotates at a distance r' from a center of rotation Ω with an angular velocity $\dot{\theta}'$ (the first derivative compared to time of the angle, θ'). And the center of rotation Ω translates compared to the wellbore center Ω_0 (see Figure D-1) in an orthonormal basis defined by the unit vectors $\hat{\imath}$ and $\hat{\jmath}$.

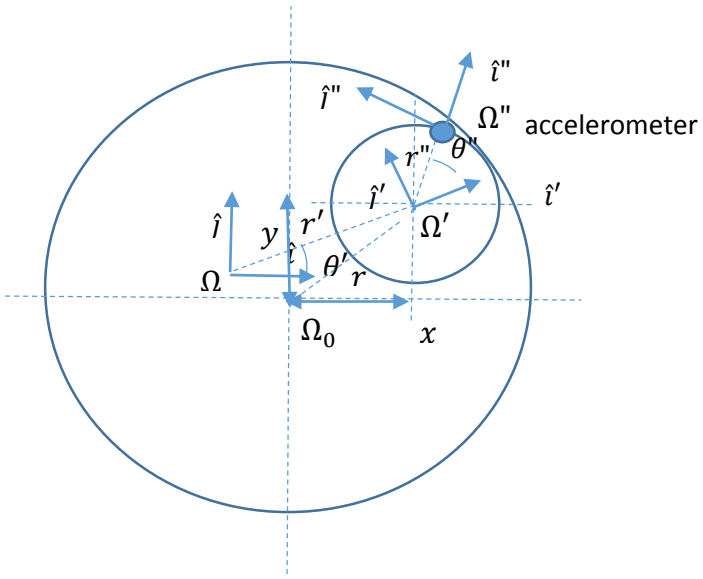

Figure D-1: Definition of the variables characterizing the movement of the accelerometer.

The polar coordinate $(r", \theta")$ are related to the geometrical position of the accelerometer and the drill-string, while (r', θ') are associated with the lateral movement of the drill-pipe inside the borehole. The latter can be contributed from either forward whirl, backward whirl or chaotic whirl.

For each of these two rotations, fictitious accelerations can be experienced by a local observer in the rotating frame. These accelerations are:

- Centrifugal acceleration: $-\vec{\omega} \times \left(\vec{\omega} \times \vec{r}\right)$
- Coriolis acceleration: $-2\vec{\omega} \times \dot{\vec{r}}$
- Euler acceleration: $-\dot{\vec{\omega}} \times \vec{r}$

However, Ω, r' and θ' are not directly known. Instead, it is most likely that we have the Cartesian coordinates (x and y) of the center line of the drill-pipe compared to the geometrical center of the borehole Ω_0, $\hat{\imath}$ and $\hat{\jmath}$. Ω, r' and θ' describes in fact a co-rotating frame which is sometime referred to as the osculating circle of the motion of the pipe center line with regards to the inertial frame defined by Ω_0, $\hat{\imath}$ and $\hat{\jmath}$. In the osculating circle, the fictitious accelerations are:

$$\gamma_r = \ddot{r}' - r'\dot{\theta}'^2 \; and \; \gamma_\theta = r'\ddot{\theta}' + 2\dot{r}'\dot{\theta}'$$

…….D-1

The curvature in the osculating circle is defined by:

$$\kappa' = \frac{1}{r'} = \frac{\dot{x}\ddot{y} - \dot{y}\ddot{x}}{(\dot{x}^2 + \dot{y}^2)^{3/2}}$$

..……D-2

And the center of the osculating circle is:

$$\begin{cases} x - \dfrac{\dot{y}}{\kappa\sqrt{\dot{x}^2 + \dot{y}^2}} \\ y + \dfrac{\dot{x}}{\kappa\sqrt{\dot{x}^2 + \dot{y}^2}} \end{cases}$$

……..D-3

which means that the angle $\theta' = \tan^{-1}\left(\frac{-\dot{y}}{\dot{x}}\right)$

Regarding the rotation of the accelerometer at the periphery of the pipe, its angle of rotation has to be corrected for the own rotation of the pipe inside the inertial frame. So if α is the angle of rotation of the pipe compared to a fixed referential, then the angle $\theta" = \alpha - \theta'$.

The pipe central line acceleration, seen from the reference frame of the accelerometer is:

$$\begin{pmatrix} \cos\theta" & \sin\theta" \\ -\sin\theta" & \cos\theta" \end{pmatrix} \begin{pmatrix} \gamma_r \\ \gamma_\theta \end{pmatrix}$$

…….D-4

This acceleration is superposed to the fictitious accelerations arising from the pipe rotation around its center line:

$$\gamma_r{}^{"} = -r^{"}\dot{\theta}^{"2} \; and \; \gamma_\theta{}^{"} = r^{"}\ddot{\theta}^{"}$$

…….D-5

Note that the first and second derivatives of the radius are zero, since the accelerometer does not move radially compared to the pipe.

Furthermore, the pipe may be subject to an axial acceleration. The axial acceleration γ_a will be seen on the axes of the accelerometer as:

$$\begin{cases} 0 \\ 0 \\ \gamma_a \end{cases} \qquad \text{……..D-6}$$

The accelerometer is also subjected to the gravitational acceleration g which is oriented downward in the global reference frame. The local inclination is denoted β and the rotation angle of the pipe in the inertial frame is α with regards to the upward vertical (see *Figure*).

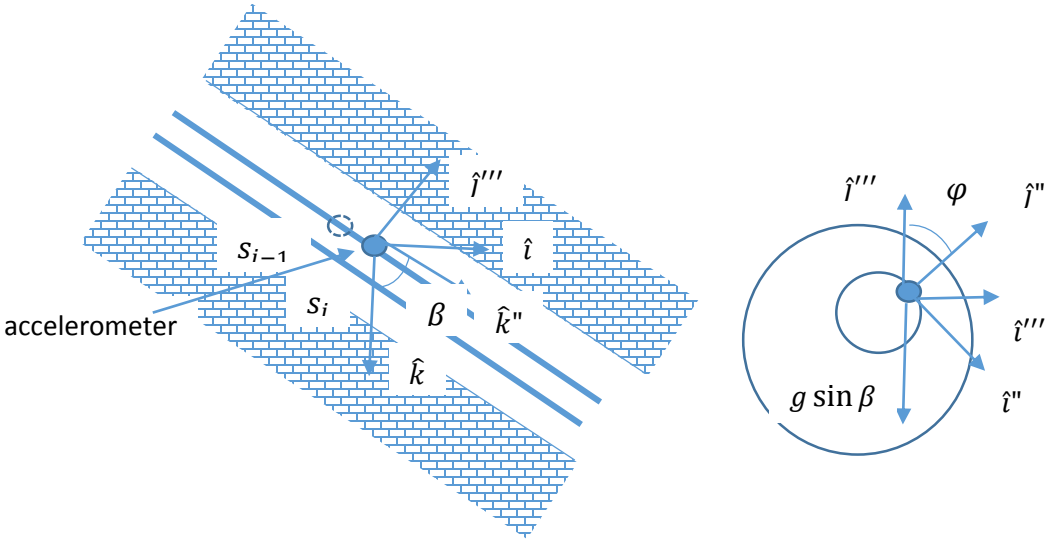

Figure D-2: axial acceleration

Then the gravitation will be seen on the axes of the accelerometer as:

$$\begin{cases} g \sin\beta \sin\varphi \\ g \sin\beta \cos\varphi \\ g \cos\beta \end{cases}$$

…….D-7

The acceleration readings are the sum of the gravitation, axial acceleration, acceleration induced by the pipe rotation around its center line and the one of the pipe center line due to lateral movement.

$$\begin{cases} g\sin\beta\sin\varphi - r"\dot{\theta}"^2 + \left(\ddot{r}' - r'\dot{\theta}'^2\right)\cos\theta" + \left(r'\ddot{\theta}' + 2\dot{r}'\dot{\theta}'\right)\sin\theta" \\ g\sin\beta\cos\varphi + r"\ddot{\theta}' - \left(\ddot{r}' - r'\dot{\theta}'^2\right)\sin\theta" + \left(r'\ddot{\theta}' + 2\dot{r}'\dot{\theta}'\right)\cos\theta" \\ g\cos\beta + \gamma_a \end{cases}$$

…….D-8

When there are no lateral and axial vibrations and for a steady rotation, the accelerometers will read:

$$\begin{cases} g\sin\beta\sin\varphi - r"\dot{\theta}"^2 \\ g\sin\beta\cos\varphi \\ g\cos\beta \end{cases}$$

……..D-9

Over a period of rotation, the average of the first component is the centrifugal force. Then we can subtract that value and extract the amplitude of the sinusoid to obtain the inclination.

For the second equation, the amplitude of the sinusoid should give the inclination.

The third equation does not need time processing to obtain the inclination.

By averaging the three estimations, it should be possible to obtain a more accurate assessment of the inclination.

However, if there are axial and/or lateral vibrations, then the accelerometer signals will contain much more noise. By applying a FFT and a pass band filter around the nominal rotational frequency, it is possible to eliminate the lateral acceleration effects.

On the other hand, by measuring the amplitude of the "noise", i.e. eliminating the main rotational frequency, it is possible to estimate the vibration level. If the vibration level goes above a defined threshold, then we can stop the rotation in order to avoid any potential destruction of the drill-string.

Appendix E

Derivation of Deflection in Walker's Model:

Function *y(x)* describes the state of the BHA (i.e. the deflected shape inclined at an angle), and this can be represented by a Fourier series[40, 42]

$$y(x) = \sum_{n=0}^{\infty} A_n \, sin \, \alpha_n x + \sum_{n=0}^{\infty} B_n \cos \alpha_n x$$

…….E-1

Satisfying the boundary conditions of no moments between the tubular and supports, both at the top and the bottom.

i.e. $-EI\frac{d^2y}{dx^2} = 0, when\ x = 0\ and\ when\ x = L$

$$\frac{dy}{dx} = \alpha_n \sum_{n=0}^{\infty} A_n \cos \alpha_n x - \alpha_n \sum_{n=0}^{\infty} B_n \sin \alpha_n x$$

…….E-2

and

$$\frac{d^2y}{dx^2} = -\propto_n^2 \sum_{n=0}^{\infty} A_n sin\alpha_n x - \propto_n^2 \sum_{n=0}^{\infty} B_n cos\alpha_n x$$

…….E-3

when *x=0,*

$$0 = -\sum_{n=0}^{\infty} \propto_n^2 B_n$$

…….E-4

This is satisfied if we set $B_n = o$ for all *n*

Also, at $x = L$ and if we also set $\alpha_n = \frac{(2n+1)\pi}{2L}$ we get a satisfying solution as below:

$$y(x) = \sum_{n=0}^{\infty} A_n sin\left[\frac{(2n+1)\pi x}{2L}\right]$$

……E-5

The optimum location of stabilizers on the collar to maximize their effectiveness is analyzed using Rayleigh-Ritz method, by which the deflection, δ at the top of the BHA (i.e. at distance, L from the bit) can approximately be obtained by considering the **minimum potential energy** of a cantilever system.[40, 42]

$$PE = Total\ Srain\ Energy - W_p$$

…….E-6

$$U = \int \frac{EI}{2}\left(\frac{d^2y}{dx^2}\right)^2 dx - W_p$$

…….E-7

Where *E* is the Young's modulus, *I* is the area moment of inertia and W_p the energy induced by the externally applied axial loads.[40]

An axial force *P(x)* will induce a negative longitudinal extension of the BHA from its unstressed length, i.e.;[46]

$$\Delta\ length = \left(\sqrt{1 + \left(\frac{dy}{dx}\right)^2} - 1\right)dx = \frac{1}{2}\left(\frac{dy}{dx}\right)^2 + 0\left(\left(\frac{dy}{dx}\right)^4\right)$$

……E-8

Thus the work done/energy induced by the axial load against the change in length is:

$$W_p = -\frac{1}{2}\int_0^L P(x)\left(\frac{dy}{dx}\right)^2 dx$$

…….E-9

Potential Energy of a Distributed Load: There is however need to consider the potential energy associated with the weight *(q)* per unit length distribution of the BHA. [45, 46] This load generates a compressive contribution, which is decomposed into axial component ($\cos\theta$) and a transverse component ($\sin\theta$). [46] If *s(x)* is the length of the BHA from the bit measured along the BHA axis, and it can be expressed as follows:

$$s(x) = \int_0^x \sqrt{1 + \left(\frac{dy(x')}{dx'}\right)^2}\, dx'$$

……..E-10

where x' is the BHA displacement.

The change in potential energy due to axial compression by the load $q(x)\Delta x$ can then be written as:

$$\Delta U_{qx} = -q(x)\Delta x \cos\theta [s(x) - x]$$

……..E-11

Integrating over the entire length of the BHA segment under consideration, we find

$$U_{qx} = -\frac{1}{2}\int_0^L q(x)\cos\theta \int_0^x \left(\frac{dy(x')}{dx'}\right)^2 dx' dx$$

..…….E-12

And the potential energy of the transverse component is:

$$U_{qy} = -\int_0^L q(x)\sin\theta\, y(x) dx$$

……..E-13

With a total of j stabilizer elements, and considering the displacement of the each stabilizer positioned at distance $L_{s,j}$ *(m)* from the bit as shown in figure 2.24 above, the transverse displacement component is equal to Δr_j, which is the radial distance from wellbore center to BHA center. A Lagrange multiplier, λ_j, is imposed and the corresponding potential energy is:

$$U_\lambda = \sum_{i=1}^{j} \lambda_j \left[y\left(L_{s,j}\right) - \Delta r_j\right]$$

……..E-14

Total Potential Energy: Combining the contributions of the externally applied axial load *P(x)* and the weight distribution of the BHA/string, the total potential energy of the string is formulated as below. [45, 46]

$$U = \int_0^L \left\{ \frac{EI}{2}\left(\frac{d^2y}{dx^2}\right)^2 - \frac{1}{2}P(x)\left(\frac{dy}{dx}\right)^2 - \frac{1}{2}q(x)\cos\theta \int_0^x \left(\frac{dy(x')}{dx'}\right)^2 dx' - q(x)\sin\theta\, y(x) \right\} dx + \sum_{i=1}^{j} \lambda_j \left[y(L_{s,j}) - \Delta r_j \right]$$

……..E-15

Minimum Potential Energy: The Ritz-coefficients A_n are determined from the principle of minimum potential energy. i.e.[46]

$$\frac{\partial U}{\partial A_n} = 0 \; and \; \frac{\partial U}{\partial \lambda_j} = 0$$

……..E-16

For all values of *n* and *j.* i.e.:

$$\frac{\partial U}{\partial A_n} = \left(\frac{EI(2n+1)^4\pi^4}{32L^3} - \frac{P(2n+1)^2\pi^2}{8L} - \frac{q\cos\theta(2n+1)^2\pi^2}{16} - \frac{q\cos\theta}{4} \right) A_n - \frac{2qL\sin\theta}{(2n+1)\pi} + \frac{1}{8}q\cos\theta \sum_{m=0}^{\infty} (2n+1)(2m+1)\left(\frac{(-1)^{n-m}-1}{(n-m)^2} + \frac{(-1)^{n+m+1}-1}{(n+m+1)^2} \right) A_m + \sum_{j=1}^{J} \lambda_j \sin\frac{(2n+1)\pi L_{s,j}}{L} = 0$$

…..…….E-17

and

$$\frac{\partial U}{\partial \lambda_j} = \sum_{m=0}^{\infty} A_m \sin\frac{(2m+1)\pi L_{s,j}}{L} - \Delta r_j = 0$$

…….E-18

Equations E-17 and E-18 can thus be simplified as equation E-19, which is then solved by matrices method.

$$a_n A_n + \sum_{\substack{m=0 \\ m\neq n}}^{\infty} e_{n,m} A_m + \sum_{j=1}^{J} \lambda_j b_{n,j} = c_n$$

……E-19

and

$$\sum_{m=0}^{\infty} b_{n,j} A_m = \Delta r_j$$

……E-20

Where we have the constants: [45, 46]

$$a_n = \frac{EI(2n+1)^4\pi^4}{32L^3} - \frac{P(2n+1)^2\pi^2}{8L} - \frac{q\cos\theta(2n+1)^2\pi^2}{16} - \frac{q\cos\theta}{4}$$

……E-21

$$b_{n,j} = \sin\frac{(2n+1)\pi L_{s,j}}{L}$$

……E-22

$$c_n = \frac{2qL\sin\theta}{(2n+1)\pi}$$

……...….E-23

$$e_{n,m} = \frac{1}{8} q\cos\theta\,(2n+1)(2m+1)\left(\frac{(-1)^{n-m}-1}{(n-m)^2} + \frac{(-1)^{n+m+1}-1}{(n+m+1)^2}\right)$$

……E-24

The solution to the Ritz-coefficients A_n are expressed in the following matrix, if the Fourier series is truncated at some value *n=N*. [45, 46]

$$\begin{bmatrix} A_0 \\ A_1 \\ A_2 \\ \vdots \\ A_N \\ \lambda \end{bmatrix} = \begin{bmatrix} a_0 & e_{0,1} & e_{0,2} & \cdots & e_{0,N} & b_0 \\ e_{1,0} & a_1 & e_{1,2} & \cdots & e_{1,N} & b_1 \\ e_{2,0} & e_{2,1} & a_2 & \cdots & e_{2,N} & b_2 \\ \vdots & \vdots & \vdots & \vdots & \vdots & \vdots \\ e_{N,0} & e_{N,1} & e_{N,2} & \cdots & a_N & b_N \\ b_0 & b_1 & b_2 & \cdots & b_N & 0 \end{bmatrix}^{-1} \cdot \begin{bmatrix} c_0 \\ c_1 \\ c_2 \\ \vdots \\ c_N \\ \Delta r \end{bmatrix}$$

……E-25

Appendix F-1: Matlab code to calculate friction factor:

```
clc;
clear;

rf = 998.2;      % density of fluid in kg/m3
pv = 0.001;      % viscosity of fluid Pa.s
u = 0.5;    % flow velocity in m/s
d = 0.008;       % internal diameter of pipe in m
E = 0.15*10^(-3);   % roughness of pipe in m
Re = rf*u*d/pv;     %calculates Reynolds no

if Re >= 4000   %turbulent flow regime
    f = (-1.8*log10(6.9/Re + ((E/d)/3.7)^(1.11)))^(-2);
else if (Re <= 2000)    % lamina flow regime
        f = 64/Re;
    else
        f1 = 64/Re;
        f2 = (-1.8*log10(6.9/Re + ((E/d)/3.7)^(1.11)))^(-2);
        Xint = (Re-2000)/(4000-2000);
        f = (1-Xint)*f1 + Xint*f2;
    end
end
    f_factor = f
```

Appendix F-2: Matlab code for settling velocity calculation:

```
clc;  clear;

rs = 2.7500; % density of cuttings, g/cc
rf = 0.9982; % Density of drilling fluid, g/cc;
dp = 0.005; % Size of cuttings, m;
PV = 0.001; % viscosity of drilling fluid, Pa-s;
g = 9.810; % Acceleration due to gravity, m/s^2

vs = 1.002; % Initial settling velocity guess, m/s

itermax = 100;      % max # of iterations
iter = 0;
errmax = 0.0000001;     % convergence tolerance
error = 0.00001;

while error > errmax & iter < itermax
v = vs;
Re = 1000*rf*v*dp/PV;

iter = iter+1;
if Re > 10^5;
        C = 0.1;    % dimensionless drag coefficient for Re>10^5
else if 1 < Re < 10^5;
    C = 24/Re*(1+0.2*Re+0.0003*Re^2)^0.5;  % drag coefficient for Re<10^5
else
        C = 24/Re;
    end
end
  vs = (4*g*dp*(rs-rf)/(3*rf*C))^0.5;   % return calculated settling velocity

        error = abs(v-vs);
            vs = 0.5*(v+vs);
end
vsettling = v
```

Appendix F-3: C++ Code to Implement Walker's Minimum Potential Energy Model

```
#include <vector>
#include <iostream>
#include <fstream>
#include <math.h>
#include "nr.h"

using std::vector;
using std::cout; using std::endl; using std::ofstream;

double const PI=acos(-1.);
// BHA inner diameter [m]
double const Di=0.07;
// BHA outer diameter [m]
double const Do=0.2;
// Area moment of inertia [m^4]
double const I=PI*(pow(Do,4)-pow(Di,4))/64;
// Hole diameter [m]
double const Dh=0.35;
// BHA weight [N] (i.e. mass times gravitational acceleration) per length,
including effect of buoyancy
double const q=9.81*8000*PI*0.25*(pow(Do,2)-pow(Di,2));
// Well inclination [degrees]
double const incl=53.;
double const inclRad = incl*PI/180;
// Axial force at tangency point [N]
double const P=5000.;
// Elastic modulus of BHA [Pa]
double const E=900*1.E9;
// First guess for the effective BHA length [m]
double Len = pow(36*E*I*(Do - Di)/(q*sin(inclRad)),0.25);
// Number of initial Lagrange multiplier constraints (1 at the tangential
point + number of stabilizers)
const unsigned numStab = 2;
// Locations of constraints (stabilizer positions and tangential point) along
x-axis of system
double stabPos[numStab] = {14.5, 20.55};
// Radial distance from wellbore center to center of BHA at each constraint
location [m]
double delR[numStab] = {0.07, 0.03};

// Function that returns the bending moment at position pos along the x-axis
double bend_Mom(const double pos) {
    //return (1+0.5*fabs(sin(PI*pos/Len)))*PI*(pow(Do,4)-pow(Di,4))/64;
    return I;
}

// Integrand for the diagonal matrix coefficients
double diag_Integr(const double pos, const int ind) {
    return E*bend_Mom(pos)*pow(sin((2*ind+1)*PI*pos/(2*Len)),2.);
}

// Integrand for the non-diagonal matrix coefficients
double non_diag_Integr(const double pos, const int m, const int n) {
```

```
    return
E*bend_Mom(pos)*(sin(0.5*(2*m+1)*PI*pos/Len)*sin(0.5*(2*n+1)*PI*pos/Len));
}

// Function to construct the main matrix
void constr_Mat(unsigned Nmax, vector<double> &posLagr, Mat_IO_DP &mat) {

    // Non-zero diagonal elements in matrix
    for (int i=0;i<=Nmax;++i) {
        // Note the sign in front of the term proportional to
q*cos(inclRad)/16: According to Walker and Sawaryn, this term should
        // have a positive sign. In our derivation (so far), we get a
negative sign. We will look into this again. For now,
        // the result of Walker and Sawaryn is implemented here (positive
sign).

        // For a non-constant bending momentum, we evaluate the associated
integrals numerically. For the diagonal coefficients:
        //double integ=NR::qtrap(diag_Integr,i,0.,Len);
        //mat[i][i]=pow(PI*(2*i+1),4)/(16*pow(Len,4))*integ-
P*PI*PI*(2*i+1)/(8*Len)+q*cos(inclRad)*pow(PI*(2*i+1),2)/16-
0.25*q*cos(inclRad);

        // Below is the diagonal coefficients for a BHA with constant bending
momentum:
        mat[i][i]=E*I*pow(PI*(2*i+1),4)/(32*pow(Len,3))-
P*PI*PI*(2*i+1)/(8*Len)+q*cos(inclRad)*pow(PI*(2*i+1),2)/16-
0.25*q*cos(inclRad);
    }
    // Off-diagonal e[i][j] elements
    double integ=0.;
    for (int i=0;i<Nmax;++i) {
        for (int j=i+1;j<=Nmax;++j) {
            //integ=NR::qtrap(non_diag_Integr,i,j,0.,Len);
            //mat[i][j]=pow(PI*PI*(2*i+1)*(2*j+1),2)/(16*pow(Len,4.))*integ;
            //mat[i][j]=mat[i][j]+q*cos(inclRad)*(2*i+1)*(2*j+1)*((-1+pow(-
1.,i-j))/pow(i-j+0.,2)+(-1+pow(-1.,i+j+1))/pow(i+j+1.,2))/8;

            // For a BHA with constant bending moment, the above integration
is identically zero. The off-diagonal elements are then:
            mat[i][j]=q*cos(inclRad)*(2*i+1)*(2*j+1)*((-1+pow(-1.,i-
j))/pow(i-j+0.,2)+(-1+pow(-1.,i+j+1))/pow(i+j+1.,2))/8;
            mat[j][i]=mat[i][j];
        }
    }

    // Total number of Lagrange multipliers
    int numLagr = posLagr.size();

    for (int i=0;i<=Nmax;++i) {
        // Off-diagonal b[i][j] elements due to stabilizers, protruding BHA
segments and tangential point
        for (int j=Nmax+1;j<=Nmax+numLagr;++j) {
            mat[i][j]=sin(PI*(2*i+1)*posLagr[j-Nmax-1]/(2*Len));
            mat[j][i]=mat[i][j];
```

```
        }
    }

    // Zero-elements in the bottom right corner of the matrix
    for (int i=Nmax+1;i<=Nmax+numLagr;++i) {
        for (int j=Nmax+1;j<=Nmax+numLagr;++j) {
            mat[i][j]=0.;
        }
    }
}

// Function to construct the original right-hand side vector
void constr_Vec(unsigned Nmax, vector<double> &radLagr, Mat_IO_DP &vec) {
    // Coefficients c in vector
    for (int i=0;i<=Nmax;++i) {
        vec[i][0]=2*q*Len*sin(inclRad)/(PI*(2*i+1));
    }

    int numLagr=radLagr.size();

    // Radial constraints due to stabilizers and tangential point
    for (int i=Nmax+1;i<Nmax+1+numLagr;++i) {
        vec[i][0]=radLagr[i-Nmax-1];
    }
}

// Function that evaluates the resulting sine-series
void sine_series_Eval(int Nmax, Mat_IO_DP &coeffs, Mat_IO_DP &func) {

    // Evaluate function at discrete positions xi and write output to the
func matrix
    int Nsamp=func.nrows()-1;
    double xi, tmp;
    double dX = Len/Nsamp;

    for(int i=0;i<=Nsamp;++i) {
        xi=i*dX;
        tmp=0.;
        for (int j=0;j<=Nmax;++j) {
            tmp=tmp+coeffs[j][0]*sin(PI*(2*j+1)*xi/(2*Len));
        }
        func[i][0]=xi;
        func[i][1]=tmp;
    }

}

// Function to test whether the BHA at some point(s) protrudes outside the
wellbore
void prot_Eval(Mat_IO_DP &func, vector<double> &pos, vector<double> &rad) {
    int Nsamp=func.nrows()-1;
    // Integer to indicate orientation of BHA: 0 = inside wellbore, +/-1 =
protruding in the positive/negative y-direction
    int side=0;
    // xmax: Position of maximum displacement within a protruding BHA segment
```

```
    double x1=0., maxval=0.;

    int i=0;

    while(i<=Nsamp) {
        if (fabs(func[i][1])-0.5*(Dh-Do) > 1.0E-5 && side==0) {
            // Store location where the BHA protrudes wellbore
            x1=func[i][0];
            maxval=fabs(func[i][1]);
            // Find at which side
            side=fabs(func[i][1])/func[i][1];
            // Find the location of maximum displacement within this
protruding BHA segment
            while (fabs(func[i][1])-0.5*(Dh-Do) > 1.0E-5 && i<Nsamp) {
                i=i+1;
                if (fabs(func[i][1])>maxval) {
                    x1=func[i][0];
                    maxval=fabs(func[i][1]);
                }
            }

            // Store point of maximum displacement in the pos vector
            pos.push_back(x1);
            // Store radial constraint at this point as well
            rad.push_back(side*0.5*(Dh-Do));
            // Update BHA orientation
            side=0;
        }
        i=i+1;
    }

}

// Function that solves the system of equations for a given set of Lagrange
multipliers
void sol_Eqs(unsigned Nmax, Mat_IO_DP &funceval, Vec_IO_DP &coeffs,
vector<double> &locLagr, vector<double> &radLagr) {

    // Total number of Lagrange multipliers
    int numLagr = locLagr.size();

    // The matrix holding coefficients a, b, e
    Mat_DP matr(Nmax+1+numLagr,Nmax+1+numLagr);

    // The vector with coefficients c and radial constraints
    // Defined as a matrix so that it can be used in conjunction with the
Gauss-Jordan algorithm in Numerical Recipes
    Mat_DP vec(Nmax+1+numLagr,1);

    // Calculating matrix and vector elements
    constr_Mat(Nmax, locLagr, matr);
    constr_Vec(Nmax, radLagr, vec);

    // Calculating the inverse of the matrix and the solution vector with
sine-series coefficients and Lagrange multipliers
```

```
    // After invoking gaussj(), the inverse matrix is stored in the first
parameter and the solution vector in the second parameter
    NR::gaussj(matr,vec);

    // Evaluate the resulting sine-series function along the effective BHA
length
    sine_series_Eval(Nmax, vec, funceval);

    // Store coefficients of sine-series
    for (int j=0;j<=Nmax;++j) {
        coeffs[j]=vec[j][0];
    }
}

// Function that evaluates the curvature (second derivative) of the
displacement function at the effective length
double eval_Curv(int Nmax, Vec_IO_DP &coeffs) {
    double curv=0.;
    for (int i=0;i<=Nmax;++i) {
        curv=curv-coeffs[i]*pow(-1.,i)*pow(PI*(2*i+1),2)/(4*Len*Len);
    }
    return curv;
}

// Function that writes Ritz coefficients and function values to file
void write_to_File(int Nmax, Vec_IO_DP &coeffs, Mat_IO_DP &func) {

    // Write all sine-series (Ritz) coefficients to file
    ofstream coeff_file;
    coeff_file.open("ritz_coeff.txt", ios::out | ios::trunc);
    for (int i=0;i<=Nmax;++i) {
        coeff_file << "A_" << i << " : \t" << coeffs[i] << "\n";
    }
    coeff_file.close();

    // Evaluate function at discrete positions xi and write output to file
and the func matrix
    int Nsamp=func.nrows()-1;
    ofstream series_file;
    series_file.open("sine_series.txt", ios::out | ios::trunc);
    series_file << "x \t Wellbore center \t Uppwer wall \t Lower wall \t w(x)
\n";

    for(int i=0;i<=Nsamp;++i) {
        series_file << func[i][0] << "\t" << 0 << "\t" << 0.5*(Dh-Do) << "\t"
<< -0.5*(Dh-Do) << "\t" << func[i][1] << "\n";
    }
    series_file.close();
}


// Function that calculates BHA displacement function for a given effective
length
double find_Func(int Nmax, int Nsamp, double tol, int remIt) {
```

```
    // Matrix to hold the position (first column) and function evaluation at
that position (second column)
    Mat_DP funceval(Nsamp+1,2);
    // Vector to store sine-series coefficients
    Vec_DP coeffs(Nmax+1);

    // Copy locations and constraints corresponding to stabilizers into
vectors
    vector<double> locLagr,radLagr;
    for(int i=0;i<numStab;++i) {
        locLagr.push_back(stabPos[i]);
        radLagr.push_back(delR[i]);
    }
    // Include Lagrange multiplier corresponding to tangential point
    locLagr.push_back(Len);
    radLagr.push_back(0.5*(Dh-Do));

    // Generate first solution based on stabilizers and tangential point as
function constraints
    sol_Eqs(Nmax, funceval, coeffs, locLagr, radLagr);

    // Update Lagrange multipliers if the BHA at some point(s) protrudes
outside the wellbore
    decltype(locLagr.size()) initsize = locLagr.size();
    prot_Eval(funceval,locLagr,radLagr);

    // If prot_Eval adds additional Lagrange multipliers, the BHA is
protruding at one or more points. In that case,
    // solve equations over and evaluate the new solution
    while(initsize != locLagr.size()) {
        initsize=locLagr.size();
        sol_Eqs(Nmax, funceval, coeffs, locLagr, radLagr);
        prot_Eval(funceval,locLagr,radLagr);
    }
    // Evaluate the curvature (second derivative) of displacement function at
tangent point
    double curvature=eval_Curv(Nmax, coeffs);

    // Write results to file if curvature is within tolerance limit or
maximum number of iterations is reached
    if(fabs(curvature) <= tol || remIt == 0)
        write_to_File(Nmax, coeffs, funceval);

    return curvature;
}

// Returning the order of the sine-series approximation, i.e. there are Nm+1
terms in the sine-series
int Nm(double L) {
    int Nmax = max(L,50.);
    return Nmax;
}

// Returning number of points at which the resulting function shall be
evaluated
```

```
int Ns(double L) {return 100*L;}

double func_trap(double const x) {return 0.34*sin(x*PI/2.34);}

int main() {
    double maxStabPos=0.;
    for(int i=0;i<numStab;++i) {
        if (stabPos[i] > maxStabPos) {
            maxStabPos = stabPos[i];
        }
        if (delR[i] > 0.5*(Dh - Do)) {
            cout << "Radial dimension of stabilizer " << i+1 << " is larger
than wellbore. Exiting..." << endl;
            exit(0);
        }
    }

    // Calculate first guess for effective BHA length
    Len=Len+maxStabPos;

    // Maximum number of iterations on the length
    int maxIter=50;
    int iter=1;
    // Upper numerical tolerance limit for second derivative at tangential
point
    double tol=1.E-5;

    double dLen = 0.025*Len;

    // Calculate the curvature at the estimated tangential point
    double curvature = find_Func(Nm(Len), Ns(Len), tol, maxIter-iter);
    double new_curv;
    cout << "Iteration - Effective length - Curvature" << endl;
    while (fabs(curvature) > tol && iter <= maxIter) {
        Len=Len+dLen;
        new_curv=find_Func(Nm(Len), Ns(Len), tol, maxIter-iter);
        curvature=new_curv;
        cout << iter << "  " << Len << "  " << curvature << endl;
        iter=iter+1;
    }
    return 0;
}
```